Università degli Studi di Napoli Federico II

Scuola di Dottorato in Ingegneria Industriale

Dottorato di Ricerca in Ingegneria dei Sistemi Meccanici

XXV Ciclo

MODELING OF THE MORPHOLOGY AND OF THE RADIATIVE HEAT TRANSFER IN OPEN-CELL FOAMS

Coordinatore della Scuola di Dottorato

Ch.mo Prof. Antonio Moccia

Coordinatore del Corso di Dottorato

Ch.mo. Prof. Fabio Bozza

Relatori

Ch.mo Prof. Nicola Bianco

Ch.mo Prof. Vincenzo Naso

Candidato

Dott. Gaetano Contento

To the Memory of

my Father and my Mother

TABLE OF CONTENTS

SUMMARY

On May 2007, ENEA (Italian National Agency for New Technology, Energy and Sustainable Economic Development) started, with the aid of the public partners Università degli studi di Napoli Federico II (DETEC) and Seconda Università degli studi di Napoli (DIAM) and the private partners CRIS-Ansaldo and Angelantoni Industria, the ELIOSLAB project. The main purpose of the project was to realize at ENEA Research Centre of Portici (Na) a national laboratory to develop technologies for solar thermal energy at high temperature (≥ 850 °C) for thermo-chemical water splitting, hydrogen production, high temperature test facilities of materials.

The above mentioned applications require good and inexpensive solar receiver-reactors of the concentrated solar radiation, which absorb well the light and transfer efficiently heat to an intermediate fluid. A volumetric receiver, with open-cell foam as the absorber material, seemed a suitable choice. In fact, high porosity open-cell foams (metallic, ceramic or carbon based) are nowadays widely used in a large number of systems. Their thermo-mechanical characteristics, in particular stiffness-strength ratio, lightness, tortuosity, good flow-mixing capability, high surface area density (i.e. interfacial surface area per unit volume), are very useful when the efficiency in the heat removing is necessary, from the power electronic systems to the thermal solar or thermo-chemical applications.

The mentioned applications generally imply high temperatures and then, the radiative heat transfer plays a significant role in the heat transfer process that, therefore, must be suitably accounted for. Unfortunately practical, flexible and sufficiently accurate tools, to model the radiative heat transfer, for the design and the optimization of systems, are scarce in the literature, whereas rather convoluted methods are suitable for scientific research purposes.

The aim of this work is to improve existing models and develop accurate and user friendly models. It has required the refined morphological modeling of inherently disordered reticulated material, too.

The morphology of the actual open-cell foams has been reviewed in Chapter 1. Suitable geometrical idealizations of the actual random reticular structure have been made using appropriate polyhedrons. Useful correlations among the principal morphological parameters of the foams, like the porosity, the strut thickness, the strut length, the cell size or the windows size with a functional relation have been proposed, according to the basic unit geometry assumed.

The conventional morphological correlations available in the literature have been considered and discussed. New correlations for the prediction of the interfacial surface area per unit volume as a function of the windows diameter and the porosity have been derived. They have then been compared with existing correlations and with experimental data found in the literature.

The morphological parameters predicted by correlations proposed in this work are in better agreement with experimental data than those predicted by the existing correlations, particularly when reference is made to the dependence of the struts cross-section on the porosity.

In Chapter 2 the radiation heat transfer in open cells foams has been modelled by a simplified analytical-numerical method based on a cubic cell, that modified an analytical model taken from the literature.

A more accurate evaluation of view factors between the significant geometric elements of the basic unit cell was carried out, by ray-tracing and numerical simulations based onto Monte Carlo method. The predictions by the original model and those by the proposed model have been compared to experimental data. The recalculated coefficients worked better than the original ones. The morphology of the foam turned out to markedly affect the radiative conductivity.

Successively, the assumption of a basic unit cubic cell has been removed and a more refined idealized structure based on a tetrakaidecahedric cell has been used. Again, the model involves a suitable discretization of the foam and asks for the evaluation of macroscopic parameters, such as radiosity and configuration factors, with a more refined geometry than in the previous model.

Configuration factors have been evaluated both by numerical Monte Carlo method and analytically with a suitable spherical approximation of the TD. The predictions of the model were compared both with experimental results from the literature and with predictions by a simplified model proposed by Zhao et al. [92] and based on a simple cubic representation of the foam unit cell. The agreement between predictions by the proposed model and experimental results is good and it is far better than predictions by the simplified model. One can, therefore, conclude that morphological characteristics need to be adequately evaluated when radiation heat transfer in foams is to be modelled, because of its dependence on the morphological characteristics of porous media**.**

RINGRAZIAMENTI

Ed ora, raggiunto un altro traguardo di questo appagante cammino, vorrei ringraziare quanti, in un modo o nell'altro, vi hanno contribuito.

Innanzitutto grazie a miei tutor Prof. Nicola Bianco e Prof. Vincenzo Naso. Il primo, per le idee stimolanti che hanno dato avvio a questo lavoro e per aver riposto la propria fiducia in uno "studente" ormai non più giovanissimo, il che era tutt'altro che scontato. Il secondo per la infinita pazienza, la cortesia, l'eleganza e l'efficacia con le quali ha fornito il suo, imprescindibile, contributo alla stesura della tesi. Senza l'aiuto e la fiducia di entrambi questo lavoro non sarebbe stato lo stesso. Grazie anche alla amica e collega Ing. Marika Oliviero per il contributo di idee offerto, per la disponibilità dimostrata nelle piccole e grandi occasioni e, soprattutto, per la sua impagabile capacità di valorizzare ed incoraggiare il mio lavoro. Mi auguro sinceramente di poter ancora lavorare a lungo con tutti quanti Voi.

Grazie all'ENEA, per avermi consentito di svolgere l'attività di dottorato congiuntamente alla mia normale attività lavorativa presso l'Agenzia. In particolare, al Dr. Leander Tapfer, alla Dr.ssa Antonella Rizzo ed all'Ingegner Carlo Privato. Soprattutto a quest'ultimo, poiché è con il progetto EliosLab che l'idea di questa tesi è nata. In particolare grazie all'amico e collega Ing. Carmine Cancro. Ho condiviso con lui una fondamentale parte della mia vita privata e professionale che così tanta importanza ha avuto nella mia formazione, come uomo, prima ancora che come ricercatore.

Grazie infinite anche alla collega Dr.ssa Luciana Mirenghi, amica affettuosa come poche, con la quale quotidianamente condivido gli spazi lavorativi e che mai ha smesso di incoraggiarmi e di ricordarmi che quella che facevo non era una "pazzia".

Grazie infine, ed al di sopra di ogni cosa, a due persone per me straordinarie nella loro normalità, che ora, purtroppo, non ci sono più. Grazie, cioè, a mio padre ed a mia madre. Per avermi amato, incondizionatamente, di un amore che non ho potuto in egual misura ripagare. Grazie di tutto, ovunque Voi siate, poiché senza di Voi la strada non sarebbe mai stata percorsa. Questo lavoro è dedicato a Voi...

"...perché forte come la morte è l'amore"

Cantico dei Cantici (8,5-7)

1 Morphology of the Open-Cell Foams and their Geometrical Representation

1.1 Introduction

The open cell foams can be considered as a part of the larger class of the so named cellular solids. These materials are largely produced and used for a lot of engineering applications (with microstructure of foams or honeycomb) and are also widely diffused in nature and, then, are largely studied. The first experimental studies of foams are owed to Hooke (1665), who discovered the typical tissues microstructure, whose fundamental unit he named "cellula". Darwin proposed some theories about the origin of cellular structure and about its function. The attention of Hooke, in particular, dwells on honeycomb planar structures in the sense that the walls which divide cells can be generated by the translation of a two dimensional structure moving in the direction perpendicular to the plane.

Another possible structure directly regards the type of materials object of this dissertation and is, instead, three dimensional. In the general 3-D case the cells could be both closed and not and the walls (real or unreal, according to whether cells are closed or not) are usually randomly oriented (see fig.1.1-1.2). Obviously, the topological modeling in the 3-D situation is much more difficult to realize than in the 2-D modeling.

In order to model foams reference is commonly made to a cellular structure as *vertexes*, joined by *edges*, which surround *faces*, that enclose *cells* [1]. The face-connectivity is defined as the number of walls that meet at an edge and similarly the edge-connectivity is the number of edges that meet at a vertex. Usually, the face-

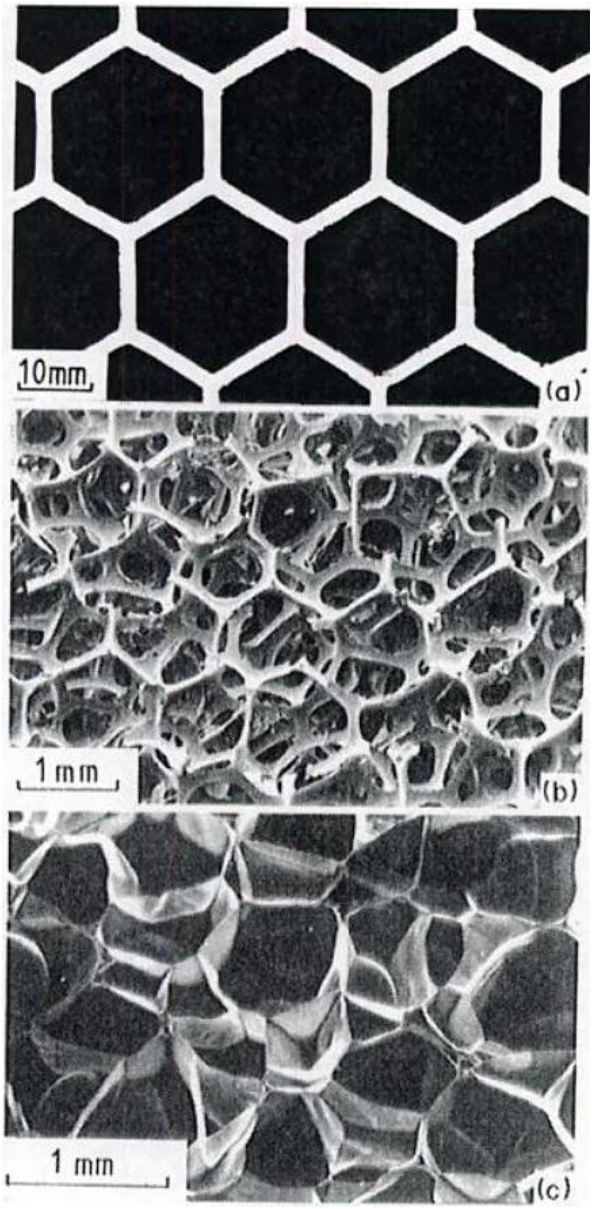

Fig.1.1. Examples of cellular solids: (a) a 2-D honeycomb; (b) a 3-D foam with open cell; (c) a 3-D foam with closed cell (from [1]).

connectivity is equal to three, but it can be as high as six in the 3-D cases. So the edge-connectivity is generally equal to three for the honeycomb structure or planar structure, but it is, instead, equal to four or higher in foams (3D).

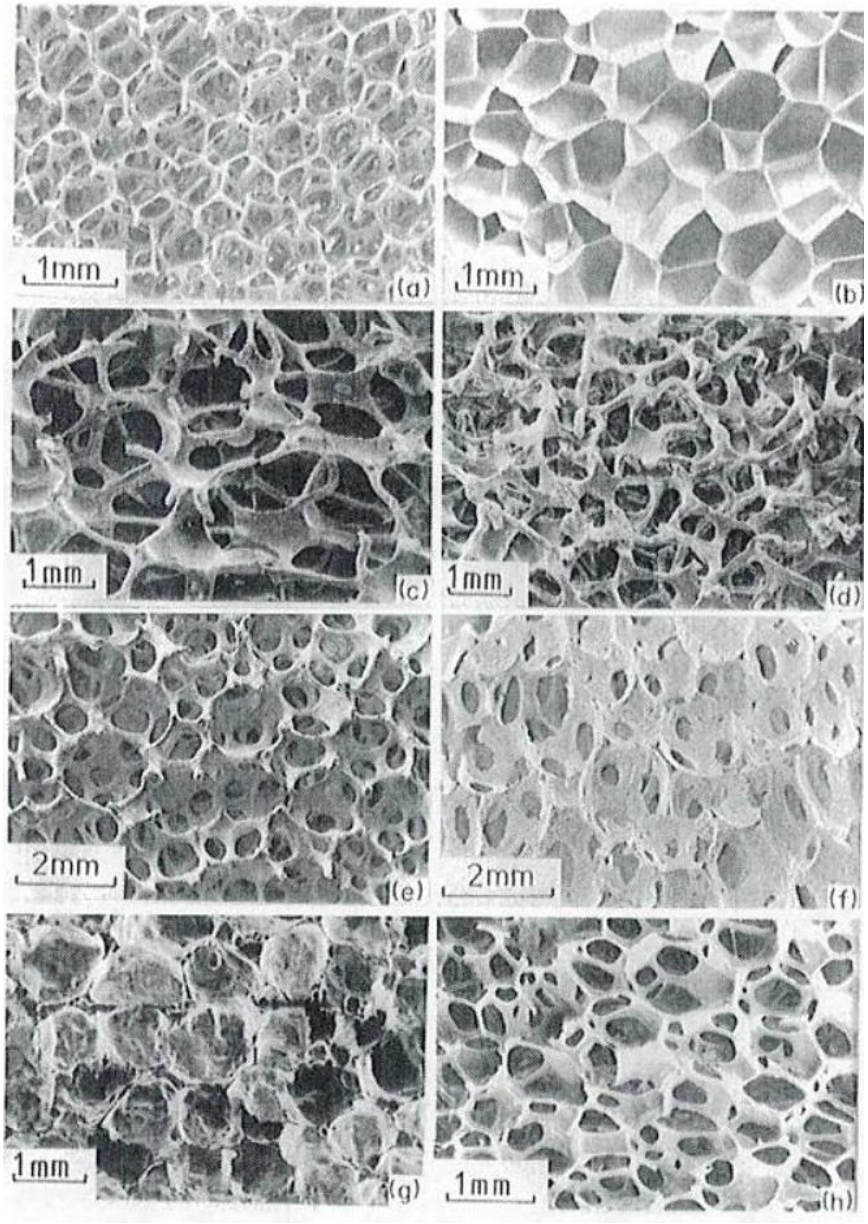

Fig.1.2. Some examples of 3-D foams: (a) open-cell polyurethane; (b) closed-cell polyethylene; (c) open-cell nickel; (d) open-cell copper; (e) open-cell zirconia; (f) open-cell mullite; (g) open-cell glass; (h) open-cells and closed-cells of a polyether foam (from [1]).

Substantially, the study of the foams morphology is based on geometrical idealizations of the cell that, filtering out the random fluctuations of the actual foams,

allow to derive suitable correlations among the relative density of the material, the dimensions of the cell, the dimensions of the faces, the length or the transversal dimensions of the edges. The last quantity has sense only when open cell foams are concerned. The topological laws that govern the edges and the faces connectivity, in fact, offer a precious aid since they impose geometric constraints to the dispersion laws and then they permit the comprehension of the structural details in the actual foams, too.

As far as the geometry and the form of the cell are concerned, the objective is, in general, to determine an "ideal" unitary cell that, with the best approximation, reproduces the actual cell form in detail, starting from geometrical characteristics measured experimentally or furnished by the manufacturers. This is the principal aim of this chapter where the analysis required by the exposed target will be described.

In fact, the actual length and the orientation of the edges, or struts (in the case of open cells), randomly fluctuate around a mean orientation or are dispersed around a mean length, that can be just determined by means of suitable measurements. In such a way, the mean length and orientation can be represented by the edge of the ideal basic cell, which obviously belongs to more contiguous cells.

In order to model an actual cellular solid with a regular structure, i.e. obtained with a regular repetition of an appropriate basic unit, such a unit must, by means of periodic spatial translation, fill space without leaving any voids and without overlaps. In many cases the basic unit can be directly identified with the same unitary cell but in other cases, a group of two o more cells is necessary.

Some ideal polyhedrons, shown in fig.1.3, have such a property.

Others polyhedrons are possible as characteristic cells for a foam. A more complete list of polyhedrons and the related geometrical characteristics are reported in fig.1.4 and in Table 1.1, respectively.

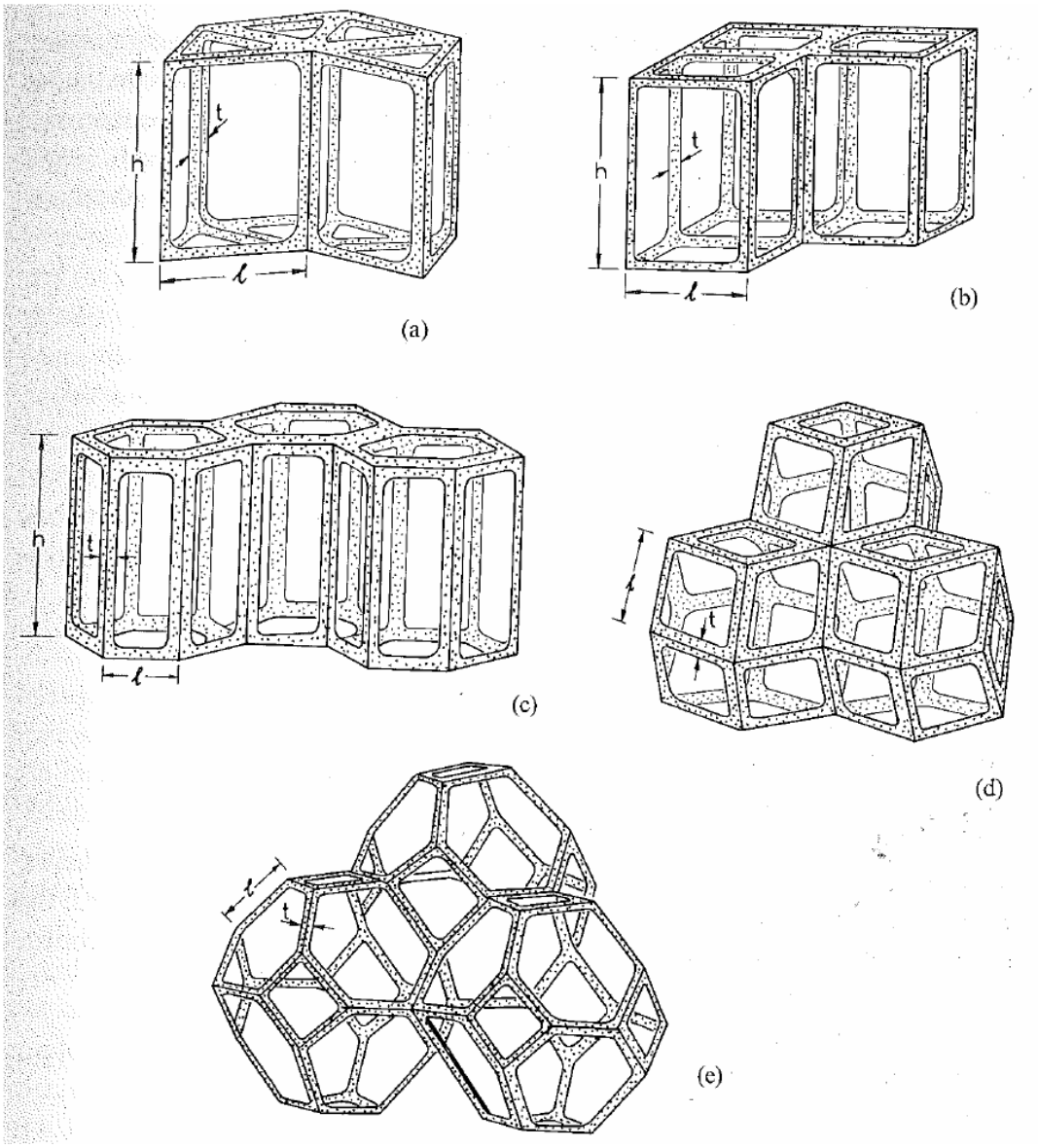

Fig.1.3. Some examples of polyhedra that fill the space: (a) triangular prisms; (b) rectangular prisms; (c) hexagonal prisms; (d) rhombic dodecahedra; (e) tetrakaidecahedra (from [1]).

A noteworthy example of polyhedron of large use in literature to analyze the convective or radiative heat transfer, the pressure drops and, in general, the transport phenomena in fluid is the pentagonal dodecahedron, which will be referred to in the next paragraphs.

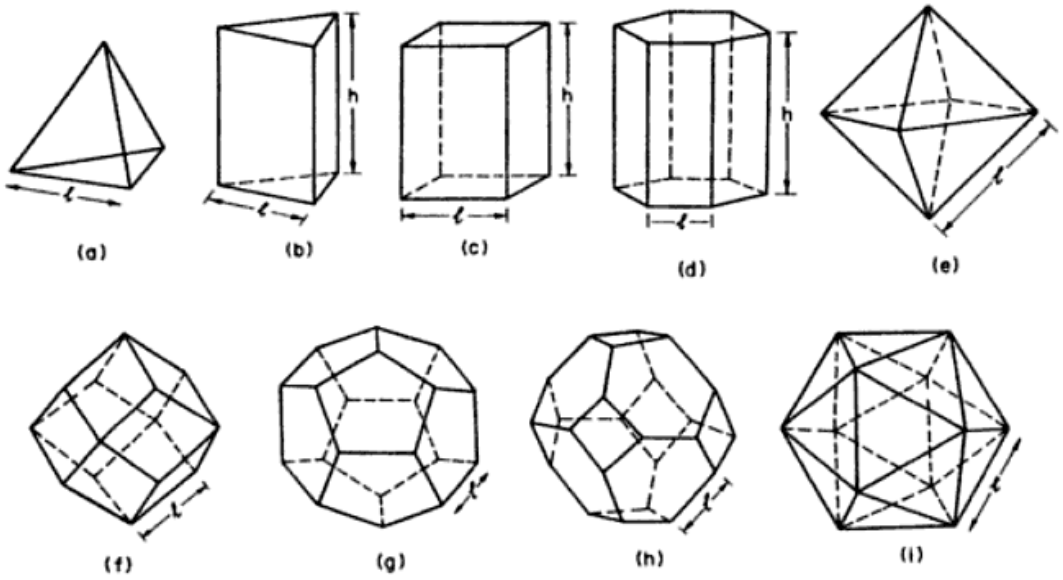

Fig.1.4. Three-dimensional polyhedric cells: (a) tetrahedron; (b) triangular prism; (c) rectangular prism; (d) hexagonal prism; (e) octahedron; (f) rhombic dodecahedron; (g) pentagonal dodecahedron; (h) tetrakaidecahedron; (i) icoesahedron (from [1]).

As far as natural foams and spontaneously aggregated foams are concerned, however, one can reasonably think of them as formed according to the criterion of minimization of the energy or, in some manner, of equilibrium like, as it is discussed in the following.

Sir William Thomson (Lord Kelvin) studied the ideal structure of a three dimensional foam as early as 1887 [2] with the aim to elaborate an appropriate model of ether. He reached onto the issue brilliant results which, however, did not enthrall his coevals [3]. The reason was that then the fundamental scientific debate onto nature of ether had started to turn in favour of its immateriality. The widespread opinion was that ether had to be considered as no more than a conventional verbal expression to indicate the vacuum, while Thomson persevered in the idea that it was "a material thing" filling the space.

Table 1.1. Geometric properties of the ideal polyhedric cells [1].

Cell shape	Faces, f (a)	Edges, n (b)	Vertices, v (c)	Volume (d) (e)	Notes (f)
Tetrahedron	4	6	4	$0.118l^3$	Regular
Triangular prism	5	9	6	$\frac{\sqrt{3}}{4}l^3A_r$	Packs to fill space
Square prism	6	12	8	l^3A_r	Packs to fill space
Hexagonal prism	8	12	6	$\frac{\sqrt{3}}{4}l^3A_r$	Packs to fill space
Octahedron	12	24	14	$0.471l^3$	Regular
Rhombic dodecahedron	12	30	20	$2.79l^3$	Packs to fill space
Pentagonal dodecahedron	14	36	24	$7.663l^3$	Regular
Tetrakaidecahedron	20	30	12	$11.31l^3$	Packs to fill space
Icosahedron				$2.182l^3$	Regular

Although the immateriality of the ether was soon demonstrated, since then results of Kelvin have been very useful in scientific and technical areas different from that for which they were presented: i.e. in crystallography, for the study of colloids, in many applications of chemical and mechanical engineering, in heat transfer problems and, in general, everywhere foams are employed.

As it has already been underlined, the problem is to realize a partition of the space vacuum using cells or group of cells having the same volume and the minimum surface. The mathematical problem is well described in [4] and "is solved in foam", how summed up by Kelvin. Previously Plateau [4] had proposed a qualitative solution of the problem, i.e. a rhombic dodecahedron (see fig.1.5a), in terms of the so named Plateau's rules. Lord Kelvin took into account the Plateau's rules, that states that the face-connectivity, Z_f, of a cell in equilibrium should be equal to 3 and that its edge-connectivity, Z_e, should be equal to 4. He concluded that the equilibrium cell

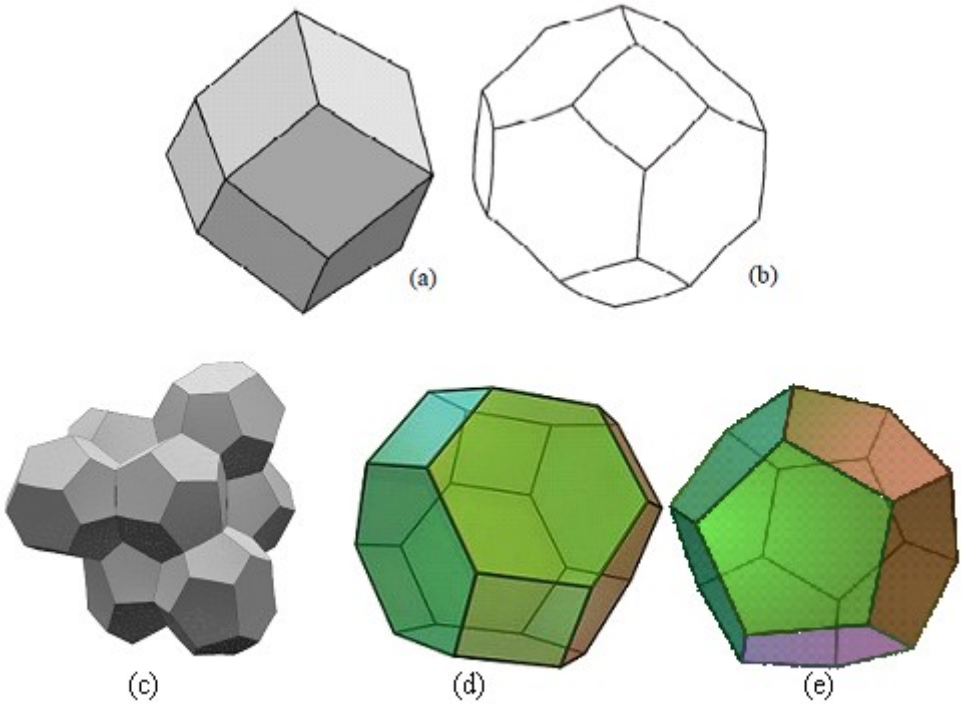

Fig.1.5. Proposed and idealized unitary cells to fill space with minimum energy: (a) rhombic dodecahedron by Plateau [4]; (b) unitary cell by Lord Kelvin, that is a TD whose edges are suitably slightly curved [2]; (c) Weaire-Phelan unit [5]; (d) idealized Kelvin's unitary cell; (e) pentagonal dodecahedric cell, that does not fill the space without overlapping or voids but idealizes the Weaire-Phelan unit.

coherent with the hypothesis was a polygonal bubble, having curved faces that meet at 120° angles (the so named Plateau lines) and edges that meet at equal 109.47° angles, thus resulting a partition of the vacuum space without overlaps and voids. The Kelvin's result is not only qualitative but also quantitative and highly accurate, even though some approximations were used in the calculations. The resulting basic unit consists of only one cell: a polyhedron with 36 equal plane edges, that form the contour of 6 nearly squared surfaces and of 8 nearly hexagonal surfaces (see fig.1.5b).

A long time afterwards it was pointed out that Kelvin's solution, based on the Plateau's rules, is only an equilibrium configuration in terms of minimization of the

surface per unit volume but not necessarily the configuration with the minimum energy (surface) in absolute [3]. In fact, Weaire-Phelan [5], thanks to some simulations with the calculator, concluded that a basic unit with energy per unit volume less than that of Kelvin is constituted by an aggregation of 8 cells: 6 made up by 12 pentagonal faces and 2 hexagonal faces and 2 made up by a pentagonal dodecahedron (PD). The authors proved that such a basic unit constitutes a partition of the space without overlaps and voids (see fig.1.5c).

Usually, two models of the cells are used in order to represent the foams under consideration with the required accuracy. For instance, this occurs in the cases, somewhat frequent, either of convective and/or conductive heat transfer or, also, when the fluid-dynamic is involved in this kind of materials. One of these models is based on a cell with tetrakaidecahedric geometry (truncated octahedron)and another is based, instead, on a pentagonal dodecahedron cell (see figs.1.5d-1.5e). Both the geometrical figures are further idealizations of the actual structure of a foam. The former, obviously, originates from the model proposed by Kelvin from which the cell can be obtained neglecting any curvature; the latter is an immediate derivation of the Weaire-Phelan model for which a prevalence of pentagonal faces is expected.

For open-cells foams, both the foregoing models in many cases match fairly well with the actual foams, as it is shown by the detailed experimental images of the foams (SEM, X-ray μ-Tomography). The important issue tackled in this thesis is that the pentagonal dodecahedron, contrary to the Weaire-Phelan unit, is not a partition of the vacuum space in the way previously described. Therefore, the radiative heat transfer cannot be modeled with the approach proposed in this work since it is not possible to build up a regular lattice starting directly from a cell having the PD form. The representation of such a type of cell with a suitable equivalent cubic cell, that is needed in order to obtain a coherent and useful lattice, will be presented in section 1.12. The tetrakaidecahedron (TD), in turn, is well known in cristallography and in solid state physics as the Wigner-Seitz cell of a body centered cubic (bcc) lattice [6].

As it has already been underlined, it is useful for modeling the radiative heat transfer inside a foam, by means of an innovative semi-analytical approach, as it will be shown in the following chapter 2.

Some models and correlations often used in literature, based on TD and PD cells or on suitable equivalent structures, are described and analyzed in the following sections. Correlations more largely used to determine the geometrical parameters of the cells starting from the experimental morphological data will be discussed and compared with experimental data taken from the literature. In many cases some new correlations predict values that better match the experimental data than those in the literature. They seem to have more solid bases than correlations usually found in the literature.

1.2 Structure of the open cells metallic and ceramic foams

Both metallic and ceramic open-cells foams can be considered as a net of interconnected solid rods whose transverse section generally is either circular or triangular or triangular with concave sides. The body of the rods (struts) can be either empty or full (see fig.1.6). The length of the rods, also named struts, is variable and lumps of material are often present where the intersections of the edges of the ideal geometry should be located.

The morphology and the microstructure of the struts and, thus, of the foams in terms of the dimensions, cross-sections, lengths, and so on, has been and still is the object of many studies and experimental investigations, as a consequence of the always more frequent and interesting applications of metallic and ceramic foams.

Finally, external solid surfaces have often a remarkable roughness that sometimes concurs to make difficult the geometrical interpretation.

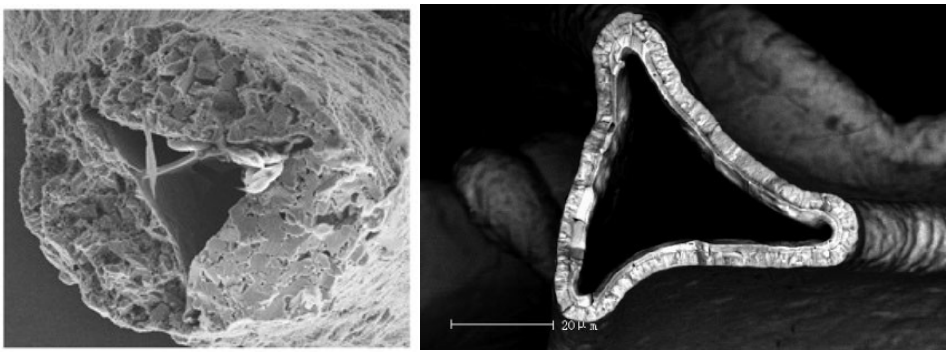

Fig.1.6: Examples of hollow cylindrical and triangular struts:
on the left, SSiC foam [7]; on the right, Nickel foam [8].

The aim of the morphological study is to find the characterizing structural parameters, such as the relative density ρ_r defined as follows

$$\rho_r = \frac{\rho_o}{\rho_s} \tag{1.1}$$

where ρ_s that is the density of the reticular solid structure, equal to

$$\rho_s = \frac{solid\ mass}{solid\ volume} = \frac{m_s}{V_s} \tag{1.2}$$

and ρ_o is the calculated density of the entire block, that is the solid material plus the fluid where the foam is immersed and that fills the vacuum spaces

$$\rho_o = \frac{solid\ mass + air\ mass}{block\ volume} = \frac{m_s}{V_o} \tag{1.3}$$

where the mass of the air is assumed to be negligible compared to the mass of the ceramic or metallic solid which substantiate the foam. If V_I is the entire inner volume, i.e. that occupied by all the pores of the foam, eqs.1.1 - 1.3allow to write

$$\rho_r = \frac{V_s}{V_o} = \frac{V_o - V_I}{V_o} \equiv 1 - \varphi_t \tag{1.4}$$

where

$$\varphi_t \equiv \frac{V_I}{V_o} \tag{1.5}$$

is the total porosity. It is the most important characteristic parameter of foams and represents the ratio of the volume of the pores (open in our usual hypothesis) to the total volume of the sample. It is worth to be remarked that very often the struts of actual foams are hollow, as it clearly shown by the SEM image in fig.1.6. Before having a deeper insight in the issue, it is worthwhile to underline that the outer surfaces of the struts are those that undergo both convective and radiative heat transfer. Therefore reference is usually made to the so named outer or open porosity, φ, that involves only the inner part of each open cell without considering the not accessible inner volume of the struts. For the sake of brevity, in the following the outer porosity will be indicated simply as porosity. Exception will be explicitly indicated when the strut has to be assumed a full body, that is without any cavity. In this case the symbol φ can be used without ambiguity. Viceversa, when the struts are hollow a fictitious density $\rho^* = V_{strut}/V_o = 1 - \varphi$ must be referred to, linked to the open porosity by means of a correlation similar to eq.1.4.

In fairly general terms the relative density of foams is less than about 0.3, also for polymeric foams, and can attain values of porosity as low as 0.003. The foams considered in this study have typical porosities as high or very high in literature: i.e. porosity higher than about 0.8 but less than about 0.99. In this work reference is made to three ranges of the porosity: $0.80 \leq \varphi < 0.90$ (high porosity), $0.90 \leq \varphi < 0.94$ (very high porosity), $0.94 \leq \varphi < 0.99$ (top porosity).

Gibson and Ashby [1] point out that, remarkably, the mechanical properties of the foams and, specially, the thermal ones are fairly dependent on the size of the cells but, rather, by the form of the cell itself and in turn by the porosity of the material or its relative density.

As it will be shown in the following chapters, however, it is concluded in this work that, at contrary, the dimensions of the open cells are fundamental together with the porosity in the determination of radiative thermal transport properties of the foams. In the following section 2.4 the dimension of the cell will turn out to be more important than the porosity in radiation heat transfer.

From a general point of view and in particular from a geometrical one, a cellular structure can be thought as constituted by *vertexes*, mutually connected by *edges*, which in turn form the contours of *faces* (or windows, in the case of open pores) that contain the cell [1]. As it was already said, the number of edges that converge on a vertex (in mean) is named edges-connectivity, Z_e, while the mean number of the faces converging on an edge is named connectivity of the faces Z_f.

For three dimensional cases and for a large number of cells the following equation holds

$$-C + F - E + V = 1 \tag{1.6}$$

where C is the number of cells, F is the number of faces, E is the number of edges and V is the number of vertexes. In such case for a single cell (C=1) one can obtain from eq.1.6 the following expression of the mean number of edges in each face $\bar{n}$

$$\bar{n} = \frac{Z_e Z_f}{Z_e - 2}\left(1 - \frac{2}{f}\right) \tag{1.7}$$

where f is the number of faces of a cell [1].

An important and useful consequence of the eq.1.7 is that in most foams, independently of the geometrical form of the cell, most faces have five edges. In fact, when the form of the cell is dodecahedric (f = 12), remembering that Z_e = 4 and Z_f = 3, $\bar{n} = 5$.

In all cases, $\bar{n} = 5.1$ and $\bar{n} = 5.4$ also when f = 14 (TD) and f = 20 (icoesahedron), respectively, as it will be proposed for the radiative model in the following. Therefore, though pentagonal faces are frequently observed in actual foams, one is not allowed to conclude that the cell has a pentagonal dodecahedric form.

It has already been stated that so far reference was made to geometrical structures that idealize the geometry of the actual cell which really exhibits dispersions in its form and dimensions. The manufacturers of metallic and ceramic foams usually provide the user with the two essential characteristics of a foam: the porosity (or relative density) and the nominal density of the pores, usually expressed in PPI i.e. pores per inch. PPI represents the number of cells (pores) per unit length of material, and it is practically equal to the reciprocal of the mean diameter of the pore (nominal diameter), d_N, that is the diameter of the sphere tangent to the faces of the ideal polyhedron associable to the real one. Such a sphere, tangent to all the faces of the ideal polyhedron associated to the real cell exists only if the polyhedron is a pentagonal dodecahedron. When, on the contrary, the polyhedron is a TD, such the above said sphere does not exist and the sphere could only be tangent to some of the polyhedron faces

$$PPI \equiv \frac{1}{d_N} \tag{1.8}$$

A sphere capable to represent the cell has, then, to be determined. It is however possible to outline that eq.1.8 can be used to determine the mean diameter of the pore experimentally, by counting the number of pores in a given length of the material using images captured by means of many instruments (X-ray axial tomography, SEM

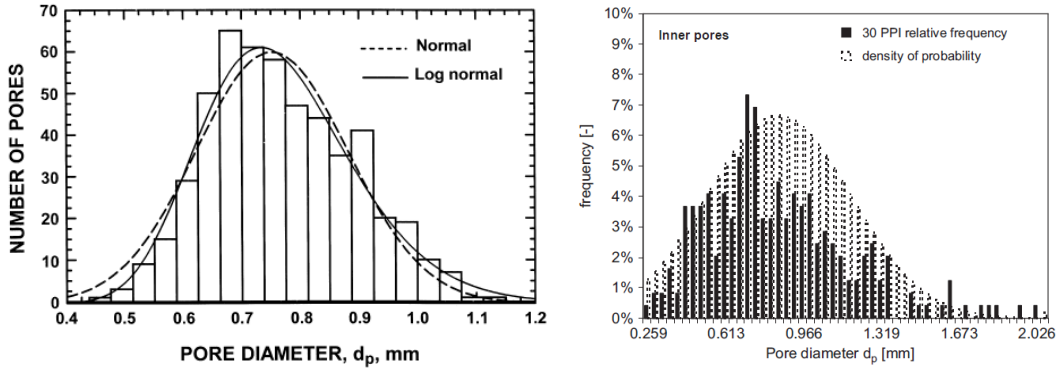

Fig.1.7. Pore size distribution for α-Al_2O_3: [9] on the left; [10] on the right.

images, etc.). Measured values are, generally, far different from the value that can be derived on the basis of data given by the manufacturer, namely the PPI value. For this reason it is better to use different symbols when reference is made to the two values. Typical results reported by Twigg et al. [9] and Incerra-Garrido et al. [10] are presented in fig.1.7.

Both diagrams show, superimposed, the normal distribution with the mean values and the standard deviations of the measured frequency distributions. The good fit of

Gaussian distributions, in general cases, as in those shown here, confirms the stochastic fluctuation of lengths and directions of the struts in open-cell foams.

Further geometrical characteristics of foams and various correlations proposed in the literature to determine all the characteristic parameters useful to predict fluid-dynamics and heat transfer will be investigated in the following sections.

1.3 Relative density, edges thickness and edges length of an ideal polyhedral cell

The relative density, ρ_r, or, equivalently, the porosity, φ, are of paramount importance in the characterization of a foam. The porosity, however, does not affect

directly momentum and heat transfer inside the material, that are, rather, dependent on the morphology and the microstructure of the material, that, in turn, affects its porosity.

From the engineering point of view, the main interest is obviously in building up suitable and useful models, depending only on a limited number of microscopic parameters of the foam, in particular on those more easily measurable. Models should also allow fairly accurate predictions and should be user friendly. To this aim, correlations that link the relative density, ρ_r, to the edge length, l, or to the edge thickness, t_o, in the case of open-cell foams, for which a defined unitary ideal cell is fixed, are needed.

The first approach to the problem was proposed by Gibson and Ashby [1]. Their correlations are largely used in the literature, with a particular reference to a tetrakaidecahedric cell. The authors presented the following correlation

$$\rho_r = C_1 \left(\frac{t_o}{l}\right)^2 \tag{1.9}$$

that holds for an open cell foam with sufficiently low density. The C_1 factor must be calculated by suitably considering the geometrical details of the cell idealization [1].

Equation 1.9 holds when an open-cell foam with sufficiently low density is involved and the C_1 factor must be calculated appropriately accounting for the geometrical details of cell idealization [1].

A more accurate formulation of the correlations among l, t_o and ρ_r take into account that eq. 1.9 overestimates the density because count more times (Z_e times) the single struts (or better the portion of them which can be considered as part of the cell) which meet to vertexes. The correction to higher order proposed by Gibson and Ashby [1] is the following general expression

$$\rho_r = C_1 \left(\frac{t_o}{l}\right)^2 (1 - C_2 \frac{t_o}{l}) \tag{1.10}$$

that introduces a new constant, C_2. However, the correction introduced is, as underlined by the authors, significant only for relative density larger than 0.2, i.e. for porosity less than 0.8. It is worth noticing that differently from what just said from the results of this thesis, as it will be seen in the following, one can conclude that a similar correction regarding the calculation of the specific surface S_v (see paragraph 1.15) is instead relevant, also for porosity values larger than about 0.80 (see par.1.17).

In the present work the interest is focused on high porosity (0.80 – 0.90) foams and very high/top porosity (0.91 – 0.99) foams. Therefore, eq. 1.9 will be assumed as the starting point for our quantitative consideration on the argument.

It is important to note, however, that correlations such as eq.1.9-1.10 are meaningful only for regular, space-filling structures because only for this type of structures it is possible to calculate the relative density in a simple and direct way. For structures based on a 3-D cell, such as a PD or an icosahedrons, or a 2-D pentagon, at contrary it is not possible to fill the space and a mixing of more figures and distortions of them are necessary to calculate, also with noticeable difficulty, a suitable relative density of the resultant structure. Therefore, equations such as eqs.1.9 and 1.10 are not useful. A list of correlations similar to eq.1.9, valid for 3-D high porosity open cell foams is reported in [1], with reference to the paper by De Hoff and Rhines [11]. The above cited correlations are presented in Table 1.2, together with the principal characteristics in terms of edges connectivity Z_e, faces connectivity Z_f, mean number of sides for face $\bar{n}$, mean number of faces for cell $\bar{f}$ and the aspect ratio $A_r = h/l$, where h is the height and l is the base of the prisms when prisms are involved, because in these cases two sides characterize the geometry.

Table 1.2. Edge and face connectivities (Z_e, Z_f), mean number of edges for face ($\overline{n}$), mean number of faces for cell ($\overline{f}$), relative density for the principal filling space polyhedral [1].

Three dimensions: open cell (Aspect ratio $A_r = h/l$)	
Triangular prisms (Z_e = 8.0, Z_f = 4.5, $\overline{n} = 3.6,\ \overline{f} = 5$)	$\rho_r = \frac{2}{\sqrt{3}}\left(\frac{t_o}{l}\right)^2\left\{1+\frac{3}{A_r}\right\}$
Square prisms (Z_e = 6.0, Z_f = 4, $\overline{n} = 4.0,\ \overline{f} = 6$)	$\rho_r = \left(\frac{t_o}{l}\right)^2\left\{1+\frac{2}{A_r}\right\}$
Hexagonal prisms (Z_e =5.0, Z_f = 3.6, $\overline{n} = 4.5,\ \overline{f} = 8$)	$\rho_r = \frac{4}{3\sqrt{3}}\left(\frac{t_o}{l}\right)^2\left\{1+\frac{3}{2A_r}\right\}$
Rhombic dodecahedra (Z_e = 5.3, Z_f = 4.5, $\overline{n} = 4.0,\ \overline{f} = 12$)	$\rho_r = 2.87\left(\frac{t_o}{l}\right)^2$
Tetrakaidecahedra (Z_e = 3.0, Z_f = 3, $\overline{n} = 5.1,\ \overline{f} = 14$)	$\rho_r = 1.06\left(\frac{t_o}{l}\right)^2$

It is reported in the named references that results are deduced for $t_o << l$, that is for very slim struts which can be considered a good position for ρ_r lesser than 0.2.

When the aspect ratio is 1 the values of the C_1 constant are comprised between 1.06 and 4.61.In particular, a coefficient equal to 1.06 results for the very important case of the TD.

One can notice that neither basic or starting assumptions, with a particular reference to the geometry, hypothesis, nor comments, for TD, on the most used correlation in the study of 3D foams, are reported in [1, 11]

In the following some correlations taken from the literature and those proposed in the present work will be compared. Some idealized and geometrical models will be compared with experimental data. Particularly, correlations for the prediction of the values of the surface per unit volume S_v will be validated, since it is of paramount

importance in the determination of the thermo-fluidodynamic and the radiative behaviour of porous materials.

1.4 The Gibson-Ashby correlation [1]: strut thickness as function of the porosity and of the edges length

The tetrakaidecahedric idealization of the basic cell in the actual open-cell foams is one of the more plausible and then frequently used representation of the foam at a sufficiently accurate level. Thanks to this representation, some new correlations will be proposed to better predict some significant morphological parameters, such as, tipically, the surface per unit volume and the strut thickness for assigned values of the pore size, the windows diameter, the porosity. The proposed correlations will be compared with experimental data taken from the literature and to the predictions of morphological models, i.e., models based on a pentagonal dodecahedric cell (see section 1.12) , the Richardsone t al.'s model (see section 1.7), the Inayat et al.'s model (see section 1.8).

Apart from the dodecahedric representation each correlation can be derived by from the Gibson-Ashby correlation [1], that links the strut thickness to the porosity and to the strut length. It is critically analyzed in the following. Its analysis will result very useful to introduce, successively, two different basic correlations among the process parameters, such as the specific surface, S_v, as a function of the porosity, φ, the windows diameter, d_w, the pore size, d_p.

We now start deriving the basic relation reported in the Table 1.2 for the TD, on the basis of simple geometrical considerations, that allow to deduce that the volume of a TD with an l long edge is equal to

$$V_{TD} = 11.31 * l^3 \tag{1.11}$$

and that the relative volume occupied by solid struts with mean section area A (that are in the first approach considered filled) is, instead, equal to

$$\rho_r \equiv \frac{V_s}{V_{TD}} = \frac{1}{3} * \frac{36 * A * l}{11.31 * l^3} = 1.06 * \frac{A}{l^2} \tag{1.12}$$

where the ratio 1/3.0 represents the fraction of the strut that has to be considered to belong to the unitary cell, since in TD $Z_e = 3.0$.

Equation.2.11 should be compared with the expression given by Gibson and Ashby [1], account being taken that, as well as in [1], until now we made no assumption on the cross-section profile

$$\rho_r = 1.06 * \frac{{t_o}^2}{l^2} \tag{1.13}$$

Remembering the correlation between the relative volume and the porosity $V_r = 1 - \varphi$ and eq.1.12, one can obtain

$$\sqrt{A} = 0.971 * (1 - \varphi)^{0.5} * l \tag{1.14}$$

Usually, however, the Gibson-Ashby equation [9, 10, 12-17]), very similar to eq.1.14 is actually used

$$t_{ga} = 0.971 * (1 - \varphi)^{0.5} * l_t \tag{1.15}$$

which is also equivalent to eq.1.13. Differently from eq.1.13, the symbol l_t is used in eq.1.15 to underline that all researchers, implicitly or explicitly, assume that the cross-section of the strut is an hollow triangle.

Rigorously, however $A \approx t_m^2$ for a suitable equivalent linear dimension t_m of the ligament section and one can write, from a general point of view,

$$t_m = k * (1 - \varphi)^{0.5} * l \tag{1.16}$$

where k is a constant to be determined using measured morphological data either on empirical or on theoretical bases. Equation 1.15 holds only if $k = 1$, i.e. if the fraction of the ligament belonging to the cell (1/3) had a square section, with a t_m long side. However, as it is widely recognized in the literature, the shape of the ligament section (triangular concave, triangular, circular) is strongly affected by the porosity [13] and, therefore, eq.1.16 cannot be used on an empirical basis.

1.5 Two new correlations for cylindrical and triangular cross section

Equation 1.15 is largely used and it is one of the basic correlations to calculate the important parameter S_v, i.e. the fluid-solid interface area per unit volume of foam. This is a fundamental parameter in the study and the prediction, through suitable models, pressure drop and convective heat transfer inside foams. Naturally, such a parameter, often measured experimentally with various methods or indirectly deduced by means of morphological measurements, plays an important role also in the radiative heat transfer.

No derivation of eq.1.15 was proposed by Gibson-Ashby book [10], however. The authors took it by the De Hoff and Rhines' book [11] where, in turn, the correlation was introduced without any geometrical justification but only on an empirical basis, in the opinion of the author. Furthermore, no assumption about the cross-section profile was made. Anyway in the literature, as to the Gibson-Ashby correlation and some of the correlations that were derived by it, reference is made to Richardson et al. [14] who recommend to consider t_{ga} as the side of a triangle section strut (see fig.1.8) is usually assumed, but the reason for this choice is not given.

Since the Gibson-Ashby correlation was the source for some useful morphological correlations, it is worthwhile to discuss and validate it as well as correlations proposed in the present work by comparison with experimental data presented in [15,16], for assigned values of the thickness and the porosity.

Experimental data of the strut thickness, strut length and porosity for seven open cell foams samples are summarized in Table.1.3 [15].

Mancin et al. [15,16] assumed a cylindrical struts and use eq.1.15 to derive their diameter and to evaluate the porosity, that is then compared with that given by the manufacturer. As a consequence, an indirect test of predictive capacity of eq.1.15 is carried out. The match among the values was good when a circular section of the ligament circular was assumed.

However, eq.1.15 is usually employed with reference to the work of Richardson et al. [14] that assumed an equilateral triangle shaped section, with a side *t* (t_s in fig.1.8c) just derived from eq.1.15.

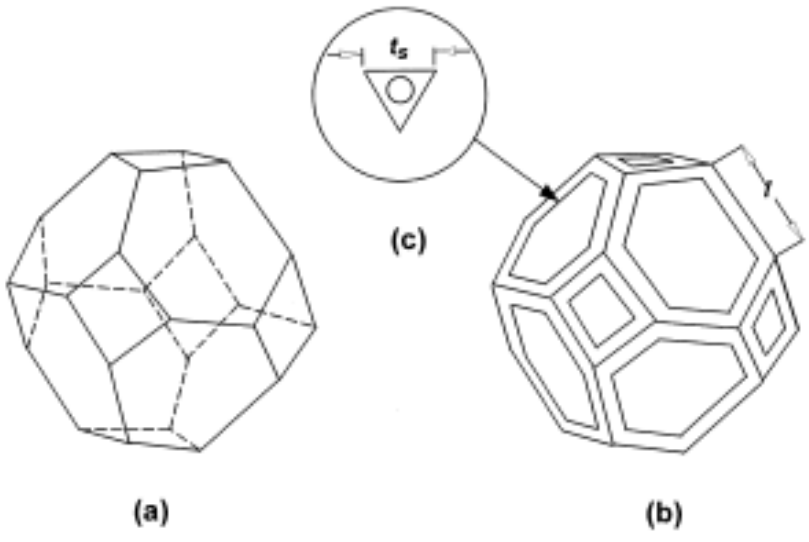

Fig:1.8:Morphological model proposed by [14]: (a) ideal tetrakaidecahedron; (b) ideal cell; (c) assumed strut cross-section.

Table 1.3. Morphological characteristics of seven aluminum foam samples [15].

Sample	SM-1	SM-2	SM-3	SM-4	SM-5	SM-6	SM-7
PPI (in^{-1})	10	10	5	40	5	10	10
Porosity, φ	0.896	0.903	0.921	0.930	0.932	0.934	0.956
Relative density, ρ_r (%)	10.4	9.7	7.9	7.0	6.8	6.6	4.4
Mean pore diameter, d_p (mm)	2.54	2.54	5.08	0.635	1.27	2.54	2.54
Area per unit volume, S_v (m^{-1})	866	839	339	1679	1156	692	537
Fiber thickness, t (mm)	0.484	0.529	0.540	0.324	0.365	0.450	0.445
Fiber length, l (mm)	1.900	1.870	1.959	1.072	1.218	1.785	1.351

Two very simple modifications to eq.1.15 will be presented in the following, that take into account the shape of the strut cross-section and the suitable different ways to denote the strut thickness.

When reference is made to a circular cross section, the following correlation can be written, with A = $\pi\, d^2/4$

$$d = \frac{2}{\sqrt{\pi}} * 0.971 * (1-\varphi)^{0.5} * l \qquad (1.17)$$

$$= 1.096 * (1-\varphi)^{0.5} * l$$

while for a triangular cross section we can write

$$t_s = \frac{2}{3^{0.25}} * 0.971 * (1-\varphi)^{0.5} * l = 1.476 * (1-\varphi)^{0.5} * \ l \tag{1.18}$$

s of the classical Gibson-Ashby correlation, match fairly well the experimental data for longer struts, while the other two correlations herein proposed work very well for the shorter struts.

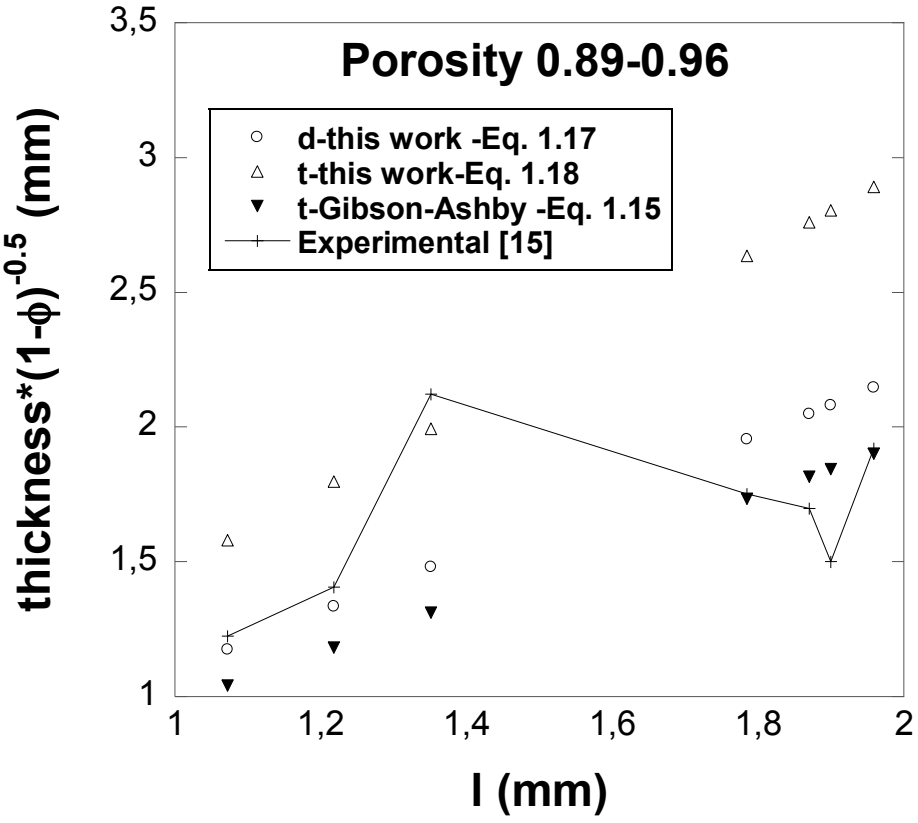

Fig. 1.9. Strut thickness times $(1-\varphi)^{-0.5}$ vs. measured ligament length

One can also remark that there are only slight deviations from the predictions given by eq.1.17 for the cylindrical model and those given by the Gibson-Ashby's model. It was to be expected because of the small difference between eq.1.15 and eq.1.17.

More precisely the correlation for the triangular strut works better for the higher porosity (φ = 0.956) and the cylindrical section whereas the Gibson-Ashby correlation tends to work better for the lower porosities (φ = 0.932, φ = 0.930).

This results agree with data for the cross-section geometry of the an open cell foam struts from the literature, that, generally, varies from a circular to a triangular shape in the 0.85 – 0.94 porosity range and from a triangular to an inner concave triangular shape in the 0.94 - 0.98 porosity range [13,17]. For shorter lengths experimental data agree better with the cylindrical correlation of this work. On the contrary, for larger lengths, the Gibson-Ashby model works better than the cylindrical model proposed in this work. Anyway, both correlations exhibit a good agreement for all lengths.

One can, however, remark that, as outlined in [18] and clearly shown in fig.1.10, the actual thickness of the struts varies passing from the centre to the extremities, is thinner in the center, where it is commonly measured, and is thicker in the proximity of the nodes (vertexes). Because of this, the diameter of the equivalent cylinder is systematically underestimated, as it was to be expected specially for longer struts, where differences between measured and predicted values are expected to be larger. As a consequence, eq.2.15, that underestimates more than eq.2.17 the average value of the thickness, gives a more accurate estimate for longer struts.

SEM images of strut cross-sections of metallic foams as a function of the porosity are presented in fig. 1.10. It shows that the larger the porosity the larger the variation. They show that the larger the porosity the larger the variation of the cross-section

profile whose side changes from cylindrical into triangular and then into triangular concave. The approximate ranges of the above mentioned profiles are schematically sketched on the top [13].

Table 1.4. Measured fiber length, l and fiber thickness, t_{meas} [18]; thickness predicted with eq.1.15, t_{ga}; diameter predicted with eq.1.17, d; thickness predicted with eq.1.18, t.

Sample	SM-1	SM-2	SM-3	SM-4	SM-5	SM-6	SM-7
Fiber thickness, t_{meas} (mm)	0.484	0.529	0.540	0.324	0.365	0.450	0.445
Fiber length, l (mm)	1.900	1.870	1.959	1.072	1.218	1.785	1.351
t_{ga} (mm) from eq.1.15	0.595	0.565	0.535	0.275	0.308	0.445	0.275
$(t_{meas} - t_{ga})/t_{meas}$ (%)	- 22.9	- 6.9	1.0	15.0	16.0	1.0	38.2
d (mm) from eq.1.17	0.671	0.638	0.603	0.311	0.348	0.502	0.310
$(t_{meas} - d)/t_{meas}$ (%)	- 38.7	- 20.6	- 11.7	4.1	5.2	- 11.6	30.2
t (mm) from eq.1.18	0.904	0.859	0.812	0.418	0.469	0.677	0.418
$(t_{meas} - t)/t_{meas}$ (%)	- 86.8	- 62.6	- 50.5	- 29.2	- 27.7	- 0.4	6.0

SEM images of a typical tetrakaidecahedron unitary cell [13] are presented in fig.1.11. The differences between the thickness at the centre and at the extremities of the strut can be detected in the left side image. The differences between the thickness of windows and pores is highlighted in the right image.

Predicted and measured fiber length and fiber thickness for seven open cell foams samples are summarized in Table.1.4 The percent deviations between predicted and measured values are sometimes fairly large. This is comprehensible because the experimental determination of the geometrical parameters of a foams is not simple also for the intrinsic disorder of the actual microstructure compared to the simple geometrical picture also in the cases of modeling based on fairly refined tetrakaidecahedric or dodecahedric cell. In all cases such an approach is very useful from an engineering point of view. In particular, a set of suitable geometrical

correlations is often used in the literature, as suggested by various authors. Therefore, a limited number of fundamental parameters, such as pore size, cell size, strut thickness, strut length and porosity is necessary to determine all the others, thus allowing the prediction of the foam behavior. More, it is the case to underline here that reasonably a suitable correlation, could be more precise to predict the thickness of the strut than, with the connected difficulties,

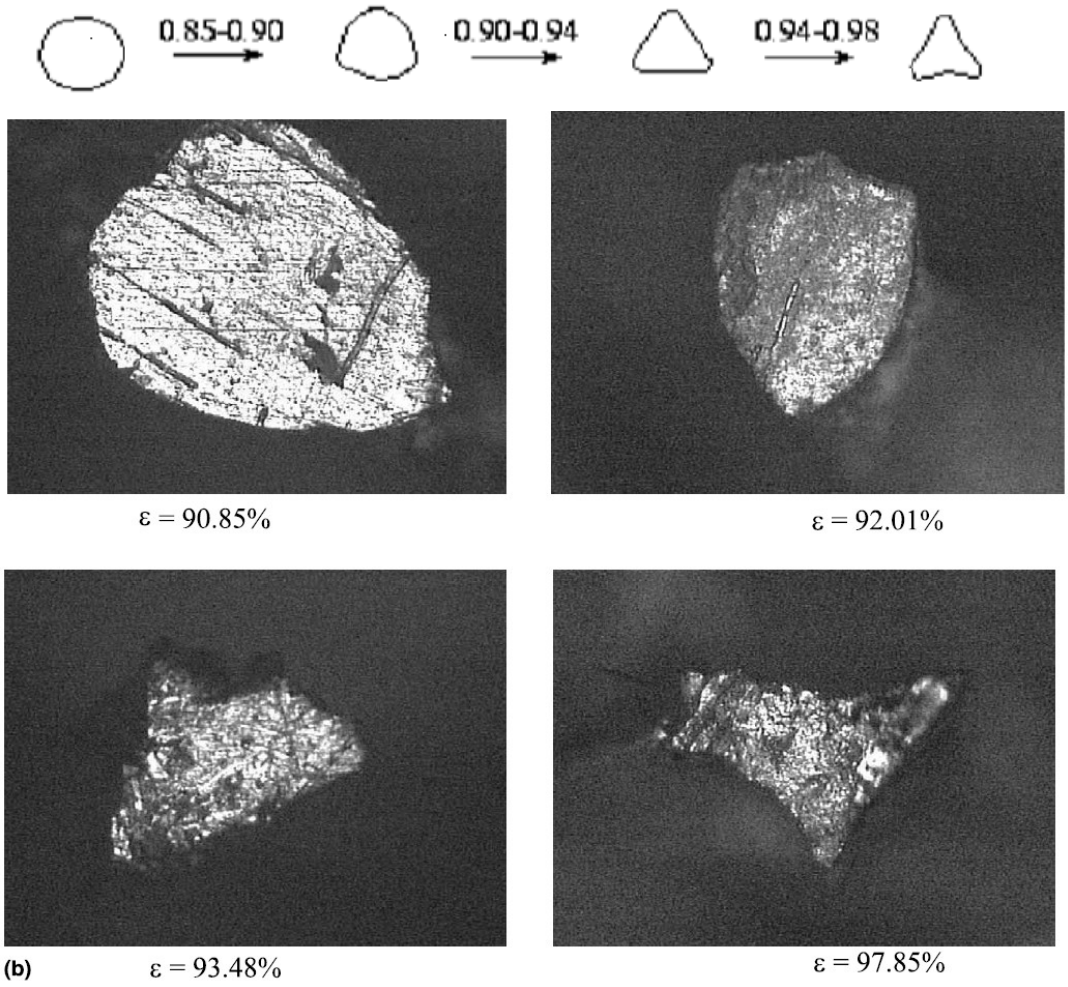

Fig.1.10. SEM images of strut cross-sections of metallic foams vs. the porosity.

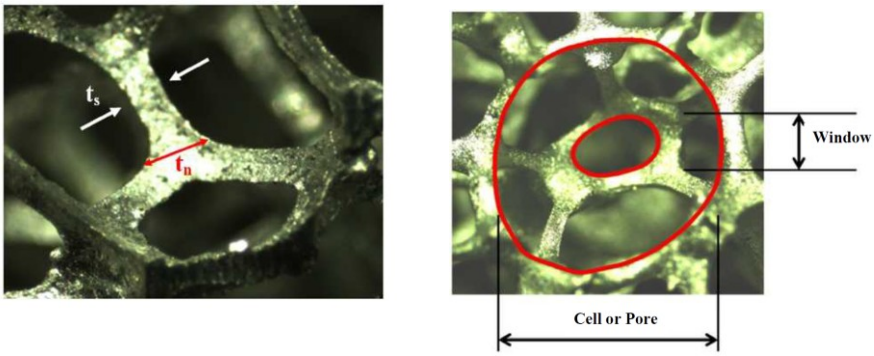

Fig. 1.11. SEM images of a typical tetrakaidecahedron unitary cell [13]

directly measure it. In fact, if sufficiently accurate a correlation links among them a suitable mean thickness, the pore size and the porosity and permits then to calculate thickness of the strut as an appropriate and significant mean value. In order to calculate the specific surface, S_v, for example is not necessary to know the measured

An example of an important quantity from this point of view is the externally accessible fluid-solid interface area per unit volume of material, S_v, that is a widely used parameter in thermo-fluidodynamics modeling and in radiative heat transfer.

thickness, that as already noted is often underestimated, but rather a suitable mean value with which get the effective porosity or the surface area per unit volume.

Since the errors on the calculation of the thickness or on the length of the ligament directly affect the evaluation of the specific surface, one can to conclude that a more refined glance on this argument is necessary, in order to reach more accurate results onto the models and onto morphology of open cells foams. With this aim a comparison with experimental data taken from the literature is important to test the more used correlations as well as those herein proposed. In particular, it is important to coherently suppose a well defined cross-section geometry of the strut, because in the two cases of cylindrical cross-section and of triangular cross-section the two different relations must be used to calculate at a first order of approximation the specific surface respectively

$$Sv_c = \frac{\pi}{3} * \frac{36 * d * l}{11.31 * l^3} \tag{1.19}$$

$$\mathrm{Sv}_t = \frac{36 * t * l}{11.31 * l^3} \tag{1.20}$$

More detailed considerations on open cells foams morphology and some new useful geometrical correlations will be presented and tested in the next sections.

1.6 The pores size and the windows size: fundamental definitions

Two more geometrical parameters are frequently used to characterize open-cell foams, namely the pore size (cell size) and the window size. In this work a net distinction between the two quantities will be made, though often authors give a different meaning to the "pore size" expression. As remarked also by Giani et al.[19] the unit cell in a foam resembles a polyhedron that limits a spherical-like inner space, so that a pore can be defined as the hollow volume of the polyhedron both PD or TD. According with [13, 16, 20] the diameter of the pore, d_p, is the reciprocal of the number of pores per unit length that, in turn, is measured counting the number of pores contained in a certain length along a fixed direction (see fig.1.11b)- Alternatively, but less accurately it can be referred to as the reciprocal of the PPI (Pores Per Inches) quantity, that characterizes the foam and that is usually given by the manufactures. It makes reference to the original polymer sponges, starting by which the final foam is obtained, so that the PPI is meaningful only for that sponge.

Representative metallic foams are depicted in Figures 1.11 and 1.12, that clearly exhibits the hexagonal faces and the square faces as well as a sphere-like structure of the cell with prevalently concave struts.

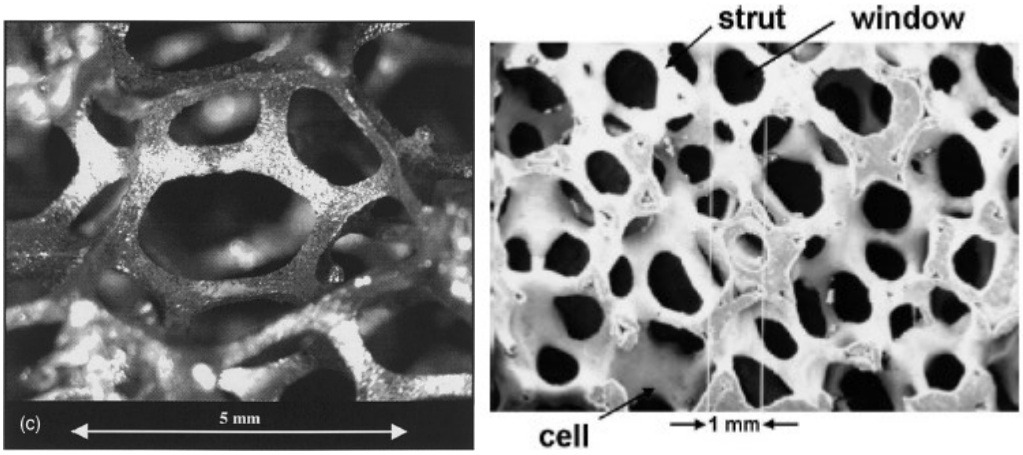

Fig.1.12. Representative metallic foams.

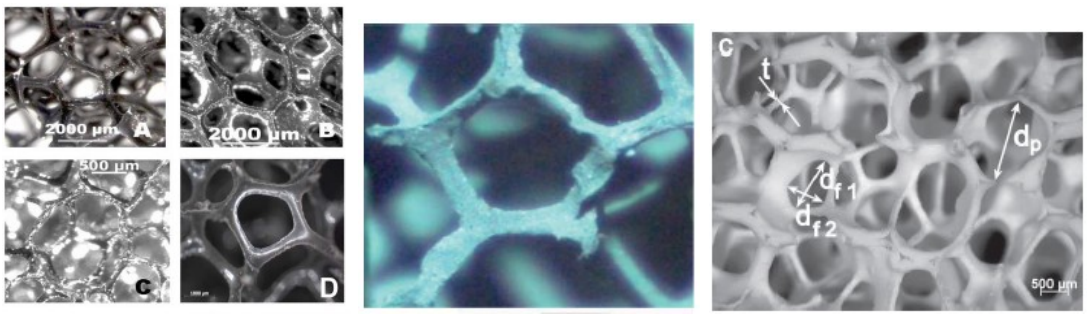

Fig.1.13. Details of a representative pentagonal dodecahedric cell. [15]

Examples of ceramic foam windows and struts are also pointed out. In the case of a foam whose cells have prevalent tetrakaidecahedric geometry and that, as consequence, can be represented with the simplified Kelvin model, there are three ways to interpret and calculate the pore size according to the ideal geometrical model of the foam used.

One consists in the identification of d_p with the diameter of a sphere tangent to the hexagonal faces; another one consists, instead, in the identification of d_p with the diameter of a sphere tangent to the square faces; finally, the third method, simply consists in calculating d_p as a mean of the above couple of values. On the contrary, for an ideal model of the foam, based on a cell with the PD geometry, d_p can be

interpreted either as the diameter of the inscribed sphere (that is a unique one) inside the cell or as that of the circumscribed sphere, or, again, as their mean value.

With the symbol d_w we denote the diameter of the window (void) whose contour is formed by the struts (see figs.1.11-1.12). Generally, distinct hexagonal faces (hexagonal voids) and squared ones [23,24] (see fig.1.12) and sometimes pentagonal faces [17] (see fig.1.13) can be observed inside foams. In the first case, usually, the measured window dimensions are those of the hexagonal faces, which can be easily detected inside the foams. In these cases the measured diameter can be looked at as the diameter of the inscribed circle or, as it occurs more frequently, as the diameter of a circle having the same area as that of the hexagonal or pentagonal face.

Sometimes, however, because of the ellipsoidal form of the window, the two axes of the ellipse are measured and their average value is assumed as d_w [20] (see fig.1.13). Finally, some authors define the measured diameters as the mean values of the equivalent diameters of the square and hexagonal faces, by taking into account the relative theoretical weights or frequencies with which each type of face should occur in a random check [25]. The same authors, moreover, underline very clearly the difference between the window diameter and the reciprocal value of the "pore count", even if, they name "pore diameter, d_p" the quantity that herein is indicated as d_w. In particular, they emphasize difficulties that arise from counting the number of the pores from a plane cut through the foam which includes not only pores parallel to the observation plane but also pores lying in different space directions causing foreshortening and all kinds of sections of cells [25].

In some cases, however, the preceding distinction is not so clear and the pore dimension or/and the cell size are treated in a somewhat incoherent manner.

Richardson et al. [14] define the quantity d_p as 1/PPI or as the reciprocal of the number of cells per unit length, but afterwards they refer it as the diameter of circle having an area equivalent to the hexagonal window, thus obtaining a set of geometrical correlations, based on the Gibson-Ashby correlation (eq.1.15),

frequently used in literature. Also in [16] the difference between d_w and d_p is not so clear.

In the following the Richardson's correlations will be discussed, new correlations will be proposed, with the aim to better predict some geometrical parameters, particularly with reference to the interface fluid-solid area per unit volume, S_v.

1.7 The Richardson et al.'s correlation [14]

In order to calculate the diameter of the circle having the same area of the hexagonal windows, that is the area of an hexagonal face without considering the contribution of the struts, reference is made to one sixth of the hexagon (see fig.1.14).

Thanks to very simple geometrical considerations, one can obtain the area of the window

$$A_e = 6 * \frac{\sqrt{3}}{4} * (1 - x)^2 \tag{1.21}$$

Noting that the area of a circle of diameter d_w is equal to $\pi\ d_w^2/4$, the following equation is then obtained imposing the equality of the two areas

$$l = 0.5498 * \frac{d_w}{\left(1 - \frac{x}{l}\right)} \tag{1.22}$$

Richardson et al. [14] combined eq.1.22 with the Gibson-Ashby correlation eq.1.15 and obtained the following important correlation between the window diameter, the porosity and the strut length

$$l_{ga} = 0.5498 * \frac{d_w}{(1 - 0.971 * (1 - \varphi)^{0.5})} \tag{1.23}$$

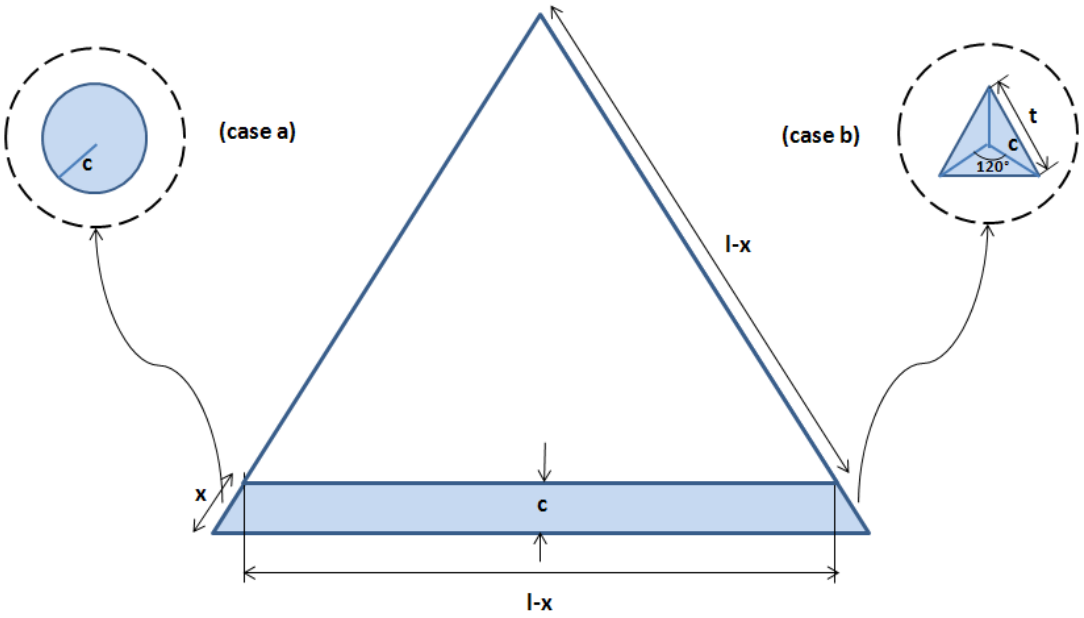

Fig.1.14. Sketch of one sixth of a hexagonal face with the portion of the strut thickness belonging t the unitary TD represented: a): cylindrical strut; b) prismatic triangular strut.

Notice that, even though d_w was determined using eq.1.21, it was defined as the same quantity elsewhere defined as the pore diameter. Moreover, a triangular cross-section was assumed in [14] and the Gibson-Ashby relation combined with eq.1.23 was used.

However, a more useful correlation is often used, which directly links the strut thickness to the pore size, to the windows diameter and to the porosity by means of a suitable functional dependence for various cases. They substituted eq.1.23 into eq.1.15 and obtained the following Richardson's correlation

$$t_{rich} = \frac{0.5339 * (1-\varphi)^{0.5}}{(1-0.971 * (1-\varphi)^{0.5})} \mathrm{d_w} \tag{1.24}$$

The above correlation was proposed by the authors in the implicit assumption that the Gibson-Ashby correlation works and the cross-section of the strut is triangular. However, the interpretation of d_w is doubtful since in eq.1.24 in [14] it is defined and calculated as the window diameter, but the symbol d_p is used instead of d_w and 1/PPI is the way through which the authors seem to measure it using experimental data for

PPI. In any case there is no doubt that eq.1.22 is used accounting for the quantity that there is called the window diameter. Equation 1.24 will be compared with other correlations in the following.

1.8 The Inayat et al.'s correlation [7]

Inayat et al. [7] presented three correlations for the cases of the tetrakaidecahedra model: cylindrical, triangular and concave cross-section. They did not derive the equations starting from basic geometrical argumentations but modifying the Richardson's relation eq.1.24. According to me, this implied an uncorrect modification of the Gibson-Ashby's correlation eq.1.15, on which eq.1.24 was based, under the assumption of validity for triangular strut. The authors use the correlation suggested for cylindrical strut, by considering the circle circumscribed to the triangular cross section (see fig.1.15). They considered two cases: a triangular cross-section, for which Gibson-Ashby eq.1.15 was made reference to and a cylindrical cross-section. In the latter case a new equation (eq.1.25) was obtained multiplying eq.1.15 times the factor $2/\sqrt{3}$, thus obtaining an equation valid for a cylindrical strut circumscribed to a triangular prismatic strut in the hypothesis (however doubtful) that, in any case, eq. 1.15 correctly describes the last type of strut

$$d_{In-c} = 0.971 * (1-\varphi)^{0.5}\, l_{In-c} \tag{1.25}$$

where the symbol $l_{In\text{-}c}$ denotes that the strut is assumed to be a cylinder.

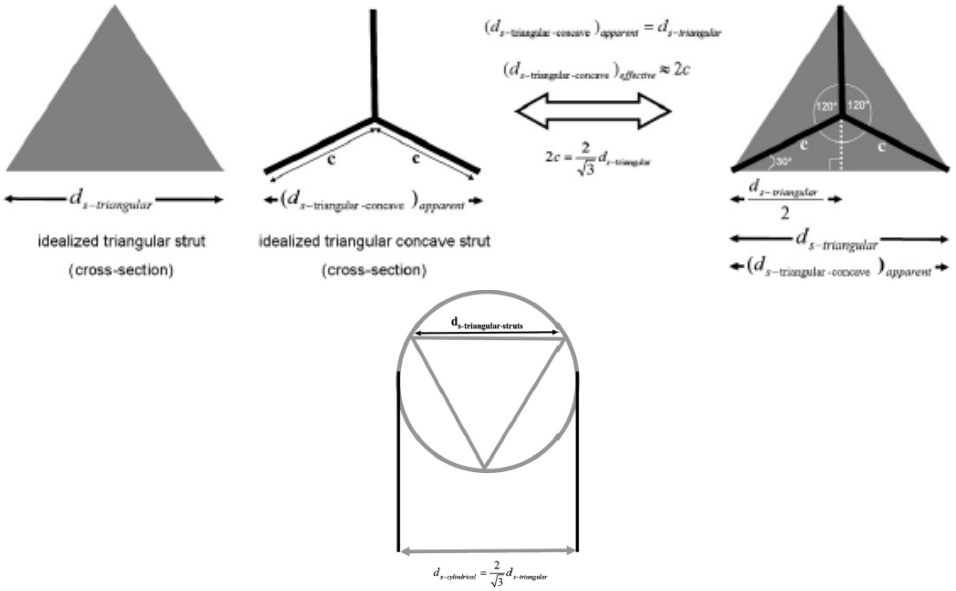

Fig.1.15. Sketch and the reciprocal geometrical correlations of an idealized: triangular strut, triangular concave strut inscribed in it, cylindrical strut circumscribed to it.[7].

The direct consequence is the somehow implicit assumption of the authors that, for a given porosity, the length of the cylindrical strut, when it is circumscribed to the triangular prismatic strut, is $2/\sqrt{3}$ times longer than it.

In a similar manner, starting again from eq.1.15, the authors introduced an inner-concave triangular strut having the same vertexes of the triangular and associated to it an "apparent thickness" equal to the actual thickness of the triangular strut and an "effective thickness" related to the effective external surface of the strut, which should be considered in the evaluation of the specific surface S_v.

The effective thickness was obtained by multiplying eq.1.15 times the factor $2/\sqrt{3}$, under the assumption that the thicknessis equal to the sum $c + c$ (see fig.1.15). Once again and surprisingly, however, the implicit assumption in the paper is that the Gibson-Ashby correlation is still valid, in between the effective thicknesses $d_{Inayat-}$

$_{concave\text{-}effective}$ - $l_{Inayat\text{-}concave}$. This implies, in turn, the explicit assumption that this last length is equal to the length, $l_{In\text{-}c}$, of the circumscribed cylindrical strut.

However, as clearly shown by eq.1.14, no theoretical justification exists for a such type of assumption, because the relating foam in this case could not have the same porosity as that of the foam with cylindrical struts. In my opinion the three cases seem not coherently described.

The three correlations proposed by the authors to link the thickness and the windows diameter in the various cases are reported in the following equations [26].

$$d_{In-c} = \frac{0.6164 * (1-\varphi)^{0.5}}{(1-0.971 * (1-\varphi)^{0.5})} d_w \tag{1.26}$$

$$d_{In-con-a} \equiv t_{rich} = \frac{0.5338 * (1-\varphi)^{0.5}}{(1-0.971 * (1-\varphi)^{0.5})} d_w \tag{1.27}$$

$$d_{In-con-e} = \frac{0.6164 * (1-\varphi)^{0.5}}{(1-0.971 * (1-\varphi)^{0.5})} d_w \tag{1.28}$$

Equations 1.26 ÷ 1.28 show that if eq. 1.15 correctly describes a triangular prismatic strut two foams having a common value of the windows diameter, d_w, and a cylindrical strut and a concave triangular strut, the former being circumscribed to the latter, should have the same density, that, obviously, would be absurd. In fact, if d_w is the same, the same should also be the length of the TD edge, l, since c assumes the same value in both cases). Furthermore, eqs.1.26 ÷ 1.28 do not permit to distinguish concave struts from triangular struts, for a given porosity and a given windows diameter. Finally, eqs. 1.26 and 1.27 imply that two foams with the same porosity and the same window would have a circular shape, whose diameter is given by eq.1.26, and a triangular shape, whose side is given by eq.1.27, respectively, i.e. they would be circumscribed; this would again be absurd.

The above mentioned equations will be discussed in the following section, with reference to equations to be derived by them, account being taken of the interface surface for unit volume S_v in the three cases above considered.

Now, we only remark that by the authors' position on concave profile follows that the measured thickness will be the "apparent" one, for which, again, we get

$$d_{In-con-a} = 0.971 * (1-\varphi)^{0.5}\, l_{In-t} \tag{1.29}$$

the Gibson-Ashby correlation being valid in this case.

1.9 New geometrical correlation among the strut thickness, the windows diameter and the porosity

As previously deduced, however, more coherently with the assumption of a triangular cross-section of the ligament, eq. 1.18 should be used instead of the Gibson-Ashby's one. With reference to fig.1.14, noting from the geometry that

$$x = \frac{2}{\sqrt{3}}\, c$$

$$c = \frac{t}{\sqrt{3}} \ (\text{case b} - \text{fig. 1.14}) \tag{1.30}$$

$$c = \frac{d}{2} \ (\text{case a} - \text{fig. 1.14})$$

it is easy to deduce that for the case of a triangular cross-section of a strut in a tetrakaidecahedric geometry (Z_e = 3), only a third of the struts belongs to each cell (TD): it is a prism having a triangular cross-section, two sides of length *c* and one side of length *t*. Using the first and the second eqs.1.30, we obtain

$$\frac{\mathrm{x}}{l_t} = 0.9837 * (1-\varphi)^{0.5} \tag{1.31}$$

and, using eq.1.22,

$$l_t = 0.5498 * \frac{d_w}{(1 - 0.9837 * (1-\varphi)^{0.5})} \tag{1.32}$$

When reference is made to a cylindrical strut, using the first and the third eqs.1.30 and substituting them into eq.2.17, we obtain

$$\frac{x}{l_c} = 0.6326 * (1-\varphi)^{0.5} \tag{1.33}$$

and, using eq.1.22, the following correlation is derived

$$l_c = 0.5498 * \frac{d_w}{(1 - 0.6326 * (1-\varphi)^{0.5})} \tag{1.34}$$

If eq.1.34 is substituted into eq.1.17 and eq.1.32 is substituted into eq.1.18, the following equations are derived for the struts with triangular cross-section

$$t = \frac{0.8115 * (1-\varepsilon)^{0.5}}{(1 - 0.9837 * (1-\varphi)^{0.5})} d_w \tag{1.35}$$

and for struts with a cylindrical cross-section

$$d = \frac{0.6026 * (1-\varphi)^{0.5}}{(1 - 0.6326 * (1-\varphi)^{0.5})} d_w \tag{1.36}$$

Three differences can be noticed between the results of the above analysis and those of Richardson:

1) not a unique correlation has been derived for the TD case, like it was in [14], independently of the shape of the strut cross-section (triangular or cylindrical);

2) a clear connection to the window diameter d_w and not to the pore (cell) diameter d_p was found;

3) two new correlations have been proposed.

1.10 Correlations for the inner concave triangular cross-section profiles as function of the windows diameter

It is now possible to propose a somewhat more refined correlation for the case of concave triangular cross-section ,which has usually proposed for a 0.94 – 0.99 porosity range (see fig.1.10), namely for top porosities, in agreement with the terminology used in this work.

Such a correlation is eq.1.42 and is obtained with reference to the inner concave triangular cross-section with a profile constructed adding up three circular arcs whose subtended cords are equal to the sides, t, of an equilater triangle that circumscribes the strut cross-section (see fig.1.16). The curvature centre of each circular arc is assumed too be the vertex of another equilateral triangle which has a common side with the external triangular profile. In other words, the arcs subtend 60° angles. Under such assumptions the internal area delimeted by each arc of length *s* and its cord of length *t* is equal to

$$A_{ac} = \frac{1}{2}\, s\, t - \frac{\sqrt{3}}{4}\, t^2 \tag{1.37}$$

where the first term is the area of a circular sector delimited by the arc *s* and the two sides of the external equilateral triangle (dotted line in fig.1.16) and the second term is the area of the triangle. The area of concave cross-section turns out to be

$$A_{ic} = \frac{\sqrt{3}}{4}\ t^2 - 3\ A_{ac} \tag{1.38}$$

So, noting that $s = (\pi/3)\ t$, we can write

$$A_{ic} = 0.1612\ t^2 \tag{1.39}$$

and, using eqs.1.39 and 1.14 the following coorrelation is finally obtained

$$d_{ic} \equiv t = 2.418\ * (1 - \varphi)^{0.5}\ l \tag{1.40}$$

Naturally, similar considerations allow to deduce a useful correlation for an inner-concave triangular profile among apparent inner-concave thickness, porosity and equivalent diameter of window. In this case eq.1.22 must be combined with a suitable expression of the *x*/*l* ratio (see eq.1.31 or eq.1.33 and fig. 1.14) valid for this specific case. In particular, also for a concave profile the first and the second term in eq.1.30 are valid. They link the apparent thickness, d_{ic}, which is equal to the side *t* of the circumscribed triangle, the geometrical parameters *x* and *c* and, using eq.1.40 gives the following equation

$$x = 1.612 * (1 - \varphi)^{0.5}\ l \tag{1.41}$$

Now, with the ratio *x*/*l* given by eq.1.41 and using eqs.1.22 and 1.40, one can obtain the following interesting correlation

$$d_{ic} \equiv t = \frac{1.3294 * (1-\varphi)^{0.5}}{(1-1.612 * (1-\varphi)^{0.5})} d_w \tag{1.42}$$

where the thickness d_{ic} assumes the clear meaning of the "apparent thickness" for the case of a triangular concave strut with fixed porosity, which is equal to the side of triangle circumscribed. However, in this case, such triangular strut has not the same porosity as that for the concave case, if the same is the windows diameter as it was implicitly assumed to derive eq.1.27, that is far different from eq.1.42, which was used for both the cases.

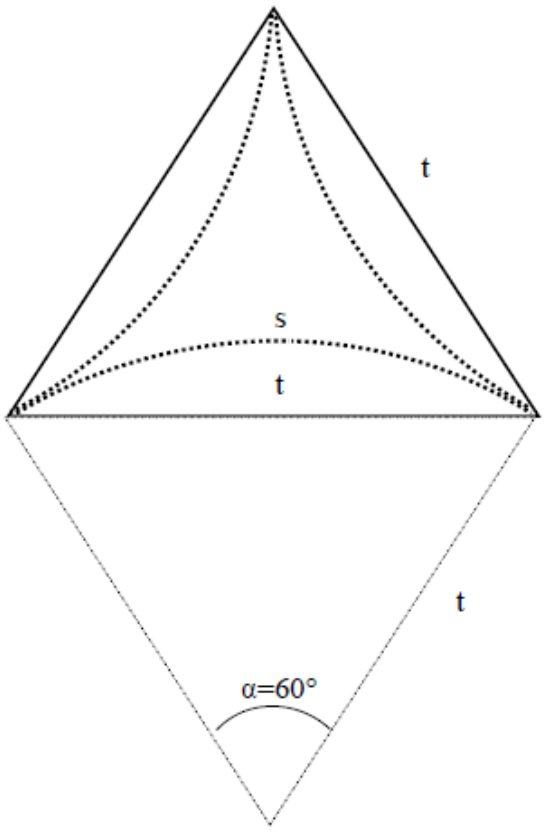

Fig.1.16. Proposed simplified geometry used to describe inner-concave triangular prismatic strut.

1.11 New geometrical correlations among the strut thickness, the pore size and the porosity

As it was already said, often the distinction between the pore size and windows diameter is not clear in the literature.

In this work, however, with the aim to test the validity of the Gibson-Ashby's correlation in cases where the pore size d_p is clearly measured, correlations will be presented among the pore size, the thickness and the porosity. The pore size can be assumed to represent the diameter of the sphere tangent to the square faces, d_1; the diameter of the sphere tangent to the hexagonal faces, d_2; the average of d_1 and d_2

$$d_p \equiv d_1 = 2\sqrt{2}\, l$$
$$d_p \equiv d_2 = \sqrt{6}\, l \tag{1.43}$$

The first definition in eqs 1.6 and the average of d_1 and d_2, only when explicitly indicated, will give the two following correlations respectively, for whichever cross-section profile.

$$l = 0.3535 * d_p \tag{1.44}$$

$$\mathrm{l} = 0.3789 * \mathrm{d_p} \tag{1.45}$$

both independent of the porosity of the foam.

The correlations between the thickness and the pore size, considered as the distance between two faced square faces in both cases, eqs.1.17 and 1.44 give

$$d = 0.3874 * (1 - \varphi)^{0.5} d_p \tag{1.46}$$

and, from eqs.1.18 and 1.44, one gets

$$t = 0.5218 * (1 - \varphi)^{0.5} d_p \tag{1.47}$$

It should be noted that in the above cases the dependence on the porosity is different from than in the previous ones. However, in all cases it is no surprise since in eqs.1.35 and 1.36 the windows diameter clearly depends on the pore size d_p, increasing with it, and on the porosity, decreasing with it.

Finally, considering that, as reported in the literature [13,17] there are many experimental evidences that in the 0.85÷0.94 porosity range the shape of the cross-section of the strut varies from the circular to the triangular, it is useful to introduce a correlation among the measured thickness, the porosity and the size of the cell, in order to interpret the measured value as a middle form in-between them. The thickness, obtained as an average value of those given by eqs. 1.46 and 1.47, is

$$d_{tc} = 0.4546 * (1 - \varphi)^{0.5} d_p \tag{1.48}$$

From eqs.2.40 and 2.44, denoting the apparent thickness with the symbol d_{ic} instead of t, we obtain

$$d_{ic} = 0.8548 * (1 - \varphi)^{0.5}\, d_p \tag{1.49}$$

that is just equal to the measured value.

Finally, with same procedure and starting form eq.1.15, the Gibson-Ashby correlation between the thickness of the strut and the pore size can be obtained

$$t_{ga} = 0.3432 * (1 - \varphi)^{0.5}\, d_p \tag{1.50}$$

different from Richardson's correlation eq.1.24. We can also remark that the Inayat's correlations discussed in section 1.8 imply the validity of eq.1.15 in all cases, i.e. that is not possible to distinguish the strut profile by means of the measure of the pore

size and of the porosity, whatever its range. On the contrary, this is made possible by the correlations herein proposed.

In conclusion, it is worth noticing that as it was reported in section 1.8, the correlations of the eq.1.25 and the eq.1.29, here again represented, hold i.e.in all cases the Gibson-Ashby (correlation eq.1.15)

$$d_{In-c} = 0.971 * (1-\varphi)^{0.5}\, l_{In-c} \tag{1.25}$$

$$d_{In-con-a} \equiv t_{In-t} = 0.971 * (1-\varphi)^{0.5}\, l_{In-t} \tag{1.29}$$

The basic geometric eq.1.43, which directly links the length of the edges of a TD (indifferently l_t or l_c) and the dimension of the cell, d_p, implies is that the correlation proposed by Gibson-Ashby (eq.1.50) must be used both for a cylindrical strut and for a prismatic triangular strut, in agreement with Inayat et al.. This permits to validate empirically and directly the Gibson and Ashby triangular strut assumption and the Inayat et al. all cross-sections assumption, apart the doubts already underlined, about equations 1.15, 1.24 and 1.50 that can be derived only from the following eq.1.14

$$\sqrt{A} = 0.971 * (1-\varphi)^{0.5} l \tag{1.14}$$

1.12 The Calmidi et al.'s pentagonal dodecahedric correlations [13,27]

Calmidi et al. [27] were the first to propose a substantial simplification of the open-cell foams morphological model. They introduced a modeling of the convective heat transfer based on a simple cubic structure (sc), i.e. a cubic reticular structure of cylindrical fibers, having an appropriate diameter, d_f, as depicted in fig.1.17. In such

a model both the fiber diameter d_f and their mutual distance d_p' must be suitably chosen, that is, in such a manner that the resulting sc structure has the same porosity (relative density ρ_r). In order to take into account the dependence of the fiber diameter on the porosity, they introduced the following shape parameter, G

$$G = 1 - exp\left(-\frac{1-\varphi}{0.04}\right) \tag{1.51}$$

and derived the following correlation among the porosity, φ, the fiber diameter, d_f, and the square side of cubic pores, d_p', which had to be the distance between two close fibers in the simple cubic (sc) reticulate and not the dimension of the cell, a,

$$\frac{d_f}{d_p'} = 2\sqrt{\frac{1-\varphi}{3\pi}}\frac{1}{G} \tag{1.52}$$

Battacharya et al.[13] then modified eq.1.52 observing that it fixes only the ratio of the representative cylindrical fibers, d_f, to their reciprocal distance, d_p'. In fact, imposing that the area of squared faces of the sc structure, equal to $(d_p')^2$, coincides with the area of the pentagonal faces of the PD having an l edge, they derived the following correlation between the dodecahedric cell size a and the step of sc grid, d_p'

$$d_p' = 0.59\, a \tag{1.53}$$

where the parameter a is determined by counting the number of cells in a given direction and repeating the procedure over different lengths to get an average value [16]. In other words a has the same significance of the pore or cell size, d_p, as it is denoted in the present work.

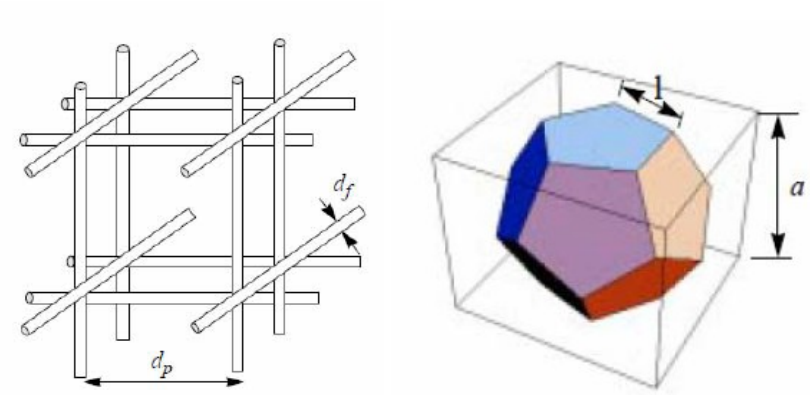

Fig.1.17. Basic geometry of the Calmidi et al.model: on the left the simple cubic reticular structure at which actual foam is equivalently reduced; on the right the unitary ideal cell adopted in the model: i.e. a pentagonal dodecahedron [28].

Then, using this symbol the following correlation among the porosity, the diameter of the cylindrical fiber and the pore size can be derived for the case of PD geometry in sc representation

$$\frac{d_f}{d_p} = 1.18\sqrt{\frac{1-\varphi}{3\pi}}\frac{1}{G} \tag{1.54}$$

And it will be referred to as the Calmidi correlation.

Equations 1.53 and 1.54, in particular, were used by Zhao et al. [28, 29, 30] with the aim to model the actual foam from a geometrical point of view, in order to get an analytical model both of the convective and radiative heat transfer inside foams.

The radiative model, in particular, inspired the work developed in this thesis in order to predict the radiative thermal conductivity by accurately using as the starter the model proposed by Zhao et al. and, successively, by modifying it by means of a geometrical modeling of open-cell ceramic and metallic foams, based on an idealized Kelvin's geometry and on a correlated lattice structure of the type "body centered

cubic" (bcc). All the details on this such approach will be discussed in the next chapter.

As to the d_p parameter, whose meaning in the Calmidi model is undoubtful, it is not fully clear if Zhao et al. [29,30] determined it either by counting the number of pores per unit length, i.e. in some way in the same manner by which the reciprocal of the PPI value (pores per Inches) given by the manufacturer is calculated, or counting the number of windows in the unit length in a cut plane through the sample.

In fact, in the first case the pore size or the cell size, d_p, interpreted as the distance between two faced pentagonal faces, should be measured whereas, in the second case, the quantity herein named the windows diameter, d_w, which in the Calmidi's model is coincident with the step of the sc reticulate, d_p', it should be equal to t. Finally, the first interpretation was preferred.

1.13 Validation of the proposed correlations among the strut thickness, the porosity and the pore size

With the aim to test the validity of the correlations in eqs.1.46 - 1.49 and eq.1.50 experimental data presented by Calmidi and Mahajan [21] and by Bhattacharya et al. [13], summarized in Table 1.5, have been used. The pore size in the above referred papers should represent the diameter of the cell (d_p herein) and not the void face diameter (d_w herein).

Measured values taken from [13] and values predicted in this work (eq.1.46), in this work (eq.1.47) and by Gibson-Ashby (eq.1.50 deduced using eqs. 1.43 and 1.15) of the strut thickness times $(1-\varphi)^{-0.5}$ as a function of the cell size, in the $0.89 \div 0.98$ porosity range, are presented in fig.1.18.

One can remark a small difference between values predicted by the Gibson-Ashby correlation (eq.1.50) and by the cylindrical correlation (eq.1.46), even though, for

instance, in order to evaluate the specific surface S_v, one must know the perimeter and, therefore, the shape of the cross section that in eq.1.50 was assumed to be triangular, should have a more important effect. Then, in order to account also for the dependence of strut shape on the porosity which is experimentally proved, it is useful to organize data in relation to this parameter. Data given by Bhattacharya et al. [13], and reported in fig.1.18, are divided and collected in three different groups: the first for the 0.89 ÷ 0.94 porosity range (figs.1.19 and 1.20); the second for the 0.94 ÷ 0.97 porosity range (fig.1.21); the third for the 0.97 ÷ 0.98 porosity range (fig.1.22).

Table 1.5. Morphological parameters of metal foams samples used to test correlations. The data are extracted from Calmidi and Mahajan [21] and Bhattacharya et al. [13].

Samples	Porosity, ϕ	PPI	d_f(m)	d_p (m)
1	0.9726	5	0.0005	0.00402
2	0.9118	5	0.00055	0.0038
3	0.9486	10	0.0004	0.00313
4	0.9138	10	0.00045	0.00328
5	0.8991	10	0.00043	0.0032
6	0.9546	20	0.0003	0.0027
7	0.9245	20	0.00035	0-0029
8	0.9005	20	0.00035	0.00258
9	0.9659	40	0.0002	0.0019
10	0.9272	40	0.00025	0.00202
11	0.9132	40	0.00020	0.0018
12	0.971	5	0.00051	0.004
13	0.946	5	0.00047	0.0039
14	0.905	5	0.00049	0.0038
15	0-949	10	0.00037	0.0031
16	0.909	10	0.00038	0.00296
17	0.978	20	0.00038	0.0028
18	0.949	20	0.00032	0.0027
19	0.906	20	0.00034	0.0026
20	0.972	40	0.00023	0.0018
21	0.952	40	0.00024	0.00198
22	0.937	40	0.00024	0.002

Measured values taken from [13] and values predicted in this work (eq.1.46), in this work (eq.1.47) and by Gibson-Ashby (eq.1.50 derived by eqs. 1.43 and 1.15) of the strut thickness times $(1-\varphi)^{-0.5}$ as a function of the cell size, in the 0.89 ÷ 0.94 porosity range are presented in fig.1.19. The linear regression of experimental data, that has a minimum variance with respect to data, is also reported in the figure.

The same experimental data and predictions of this work by correlations 1.46, 1.47 and 1.48, in the 0.89 ÷ 0.94 porosity range, are presented in fig.1.20. It can be noted that the correlation 1.48 relative to a strut having an intermediate profile, between the

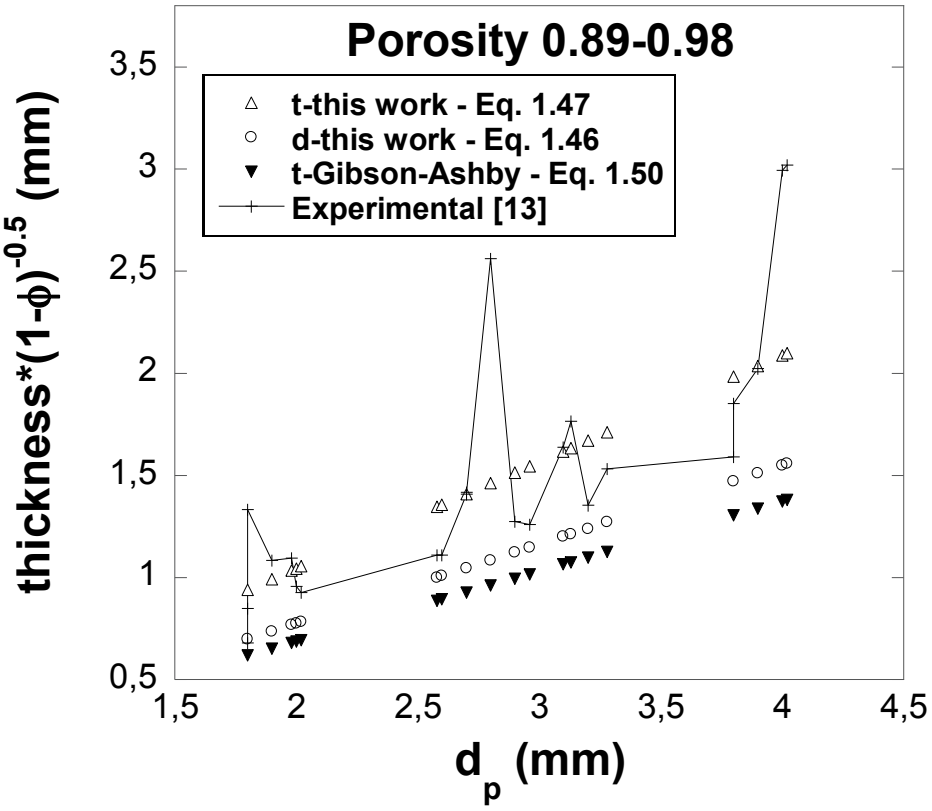

Fig. 1.18. Measured cell size vs. ligament thickness multiplied for the factor $(1-\varphi)^{-0.5}$.

cylindrical and the triangular, matches very well with the experimental data. In particular, it adapts very well, and better than any other set of predicted values, to the best-fit line of experimental data, the correlation 1.48 having the minimum variance with respect to data.

Measured data and predictions obtained by eqs. 1.46, 1.47 and 1.49, for triangular, cylindrical and inner-concave triangular cross-section, together with the linear regression of data, in the porosity range 0.94 - 0.97, are reported in fig.1.21.

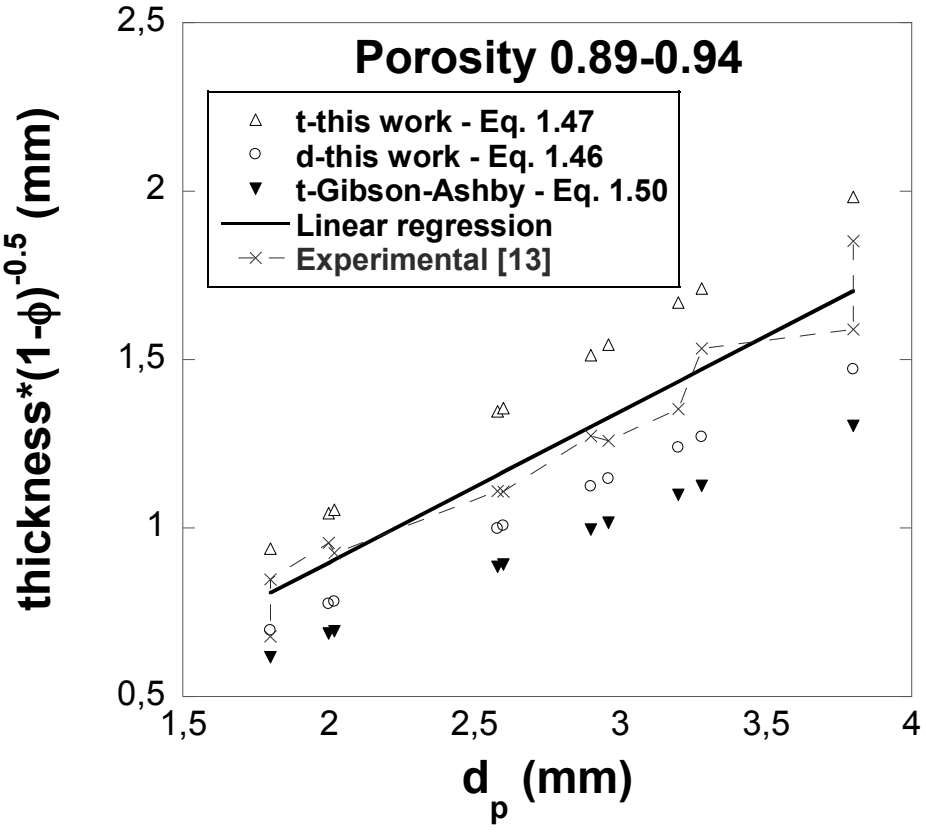

Fig. 1.19. Measured cell size vs. ligament thickness multiplied for the factor $(1-\varphi)^{-0.5}$

Table 1.6a. Data extracted from Fuller et al. [31]. Sintered FeCrAlY foam samples.

Sample	S1	S2	S3	S4	S5	S6	S7
Measured pore size, d_p (mm)	3.131	3.109	1.999	2.089	0.975	0.959	1.998
Measured ligament diameter d_f (μm)	287	351	215	267	124	154	241
Effective porosity, φ	0.917	0.822	0.917	0.879	0.898	0.852	0.897

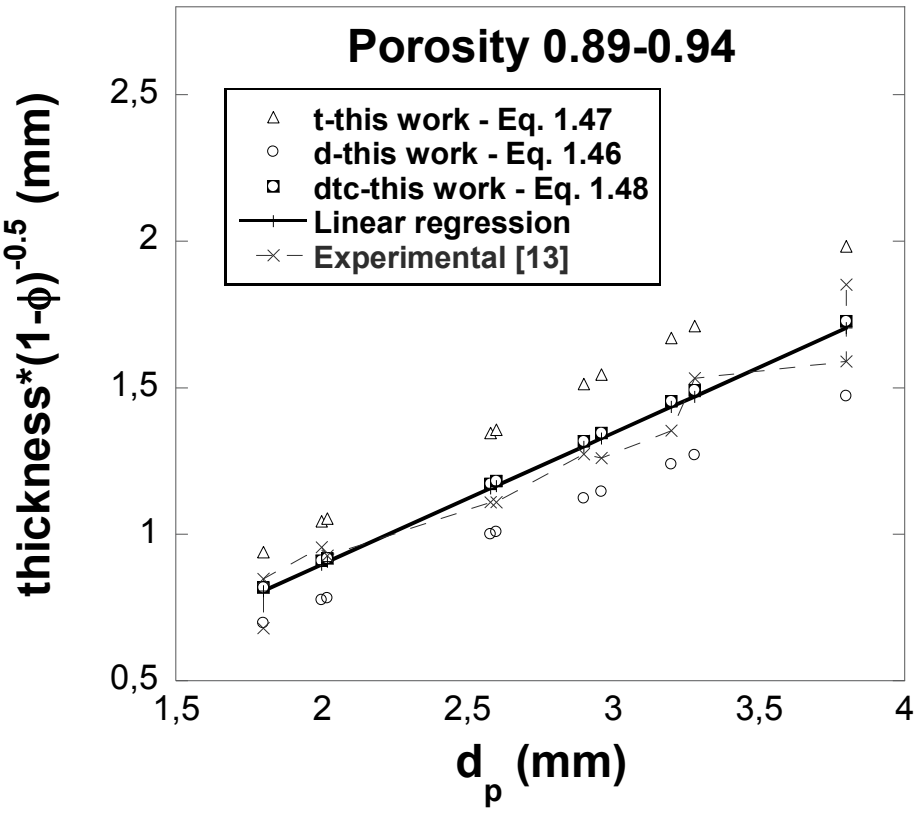

Figure 1.20. Measured cell size vs. measured ligament thickness multiplied for the factor $(1-\varphi)^{-0.5}$.

Table 1.6b. Data extracted from Zhao et al.[24, 25]. Copper samples whose effective porosity coincide with outer porosity (full struts).

Sample	Cu1	Cu2	Cu3	Cu4	Cu5	Cu6
Measured pore size d_p (mm)	2.645	2.697	1.284	1.431	0.554	0.657
Measured ligament diameter, d_f (μm)	263	270	122	127	88.8	93.2
Effective porosity, φ	0.926	0.885	0.940	0.881	0.927	0.915

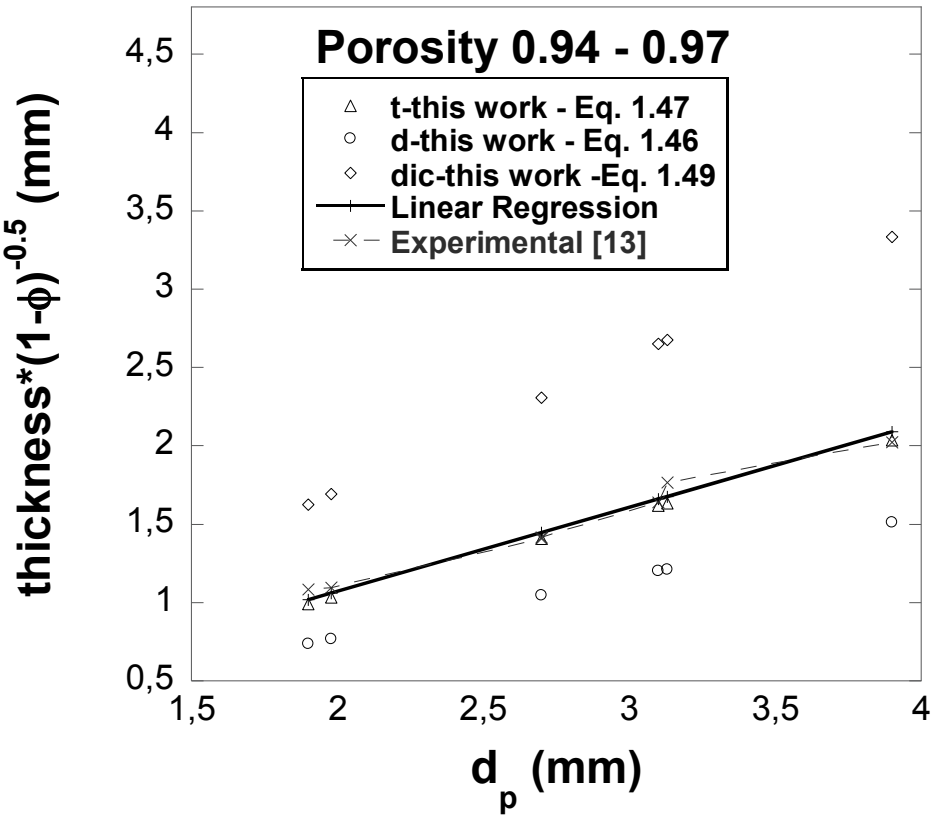

Figure 1.21. Measured cell size vs. measured ligament thickness multiplied for the factor $(1-\varphi)^{-0.5}$.

Coherently with experimental observations [13] (see fig.1.10) the triangular cross-section give the best predictions.

Measured data and predictions given by eqs. 1.46, 1.47 and 1.49, for triangular, cylindrical and inner-concave triangular cross-section, together with the inear regression of data, for a porosity $\varphi \geq 0.97$, are presented in fig.1.22 which clearly shows the validity of inner-concave triangular cross-section.

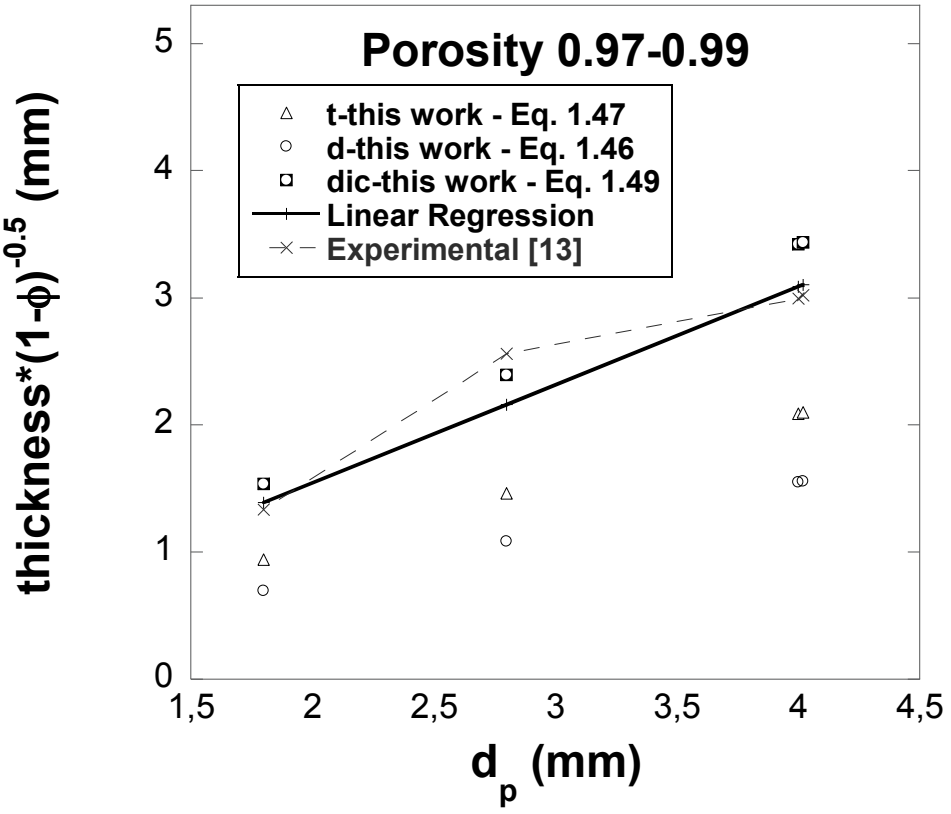

Figure 1.22. Measured cell size vs. measured ligament thickness multiplied for the factor $(1-\varphi)^{-0.5}$.

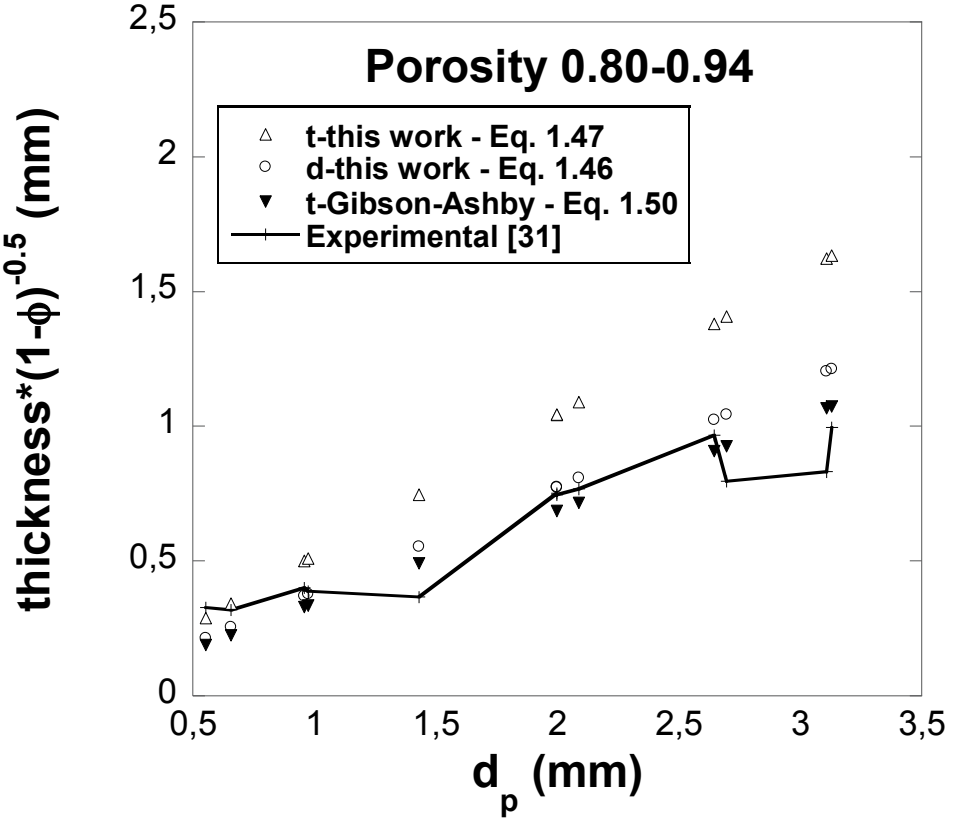

Figure 1.23. Measured cell size vs. measured ligament thickness multiplied for the factor $(1-\varphi)^{-0.5}$.

Experimental data by Fuller et al. [31] and from Zhao et al.[24, 25], reported in Table 1.6, have been used to test the correlations among the thickness of the ligament, cell size and the porosity, even though in these last works the interpretation of term "pore size" is somewhat doubtful. Furthermore, measured values of the relative density have been suitably corrected by the authors in order to take into account the effect of the hollow struts. An effective porosity of the investigated samples has been evaluated that could have introduced some inaccuracies in the evaluated quantities.

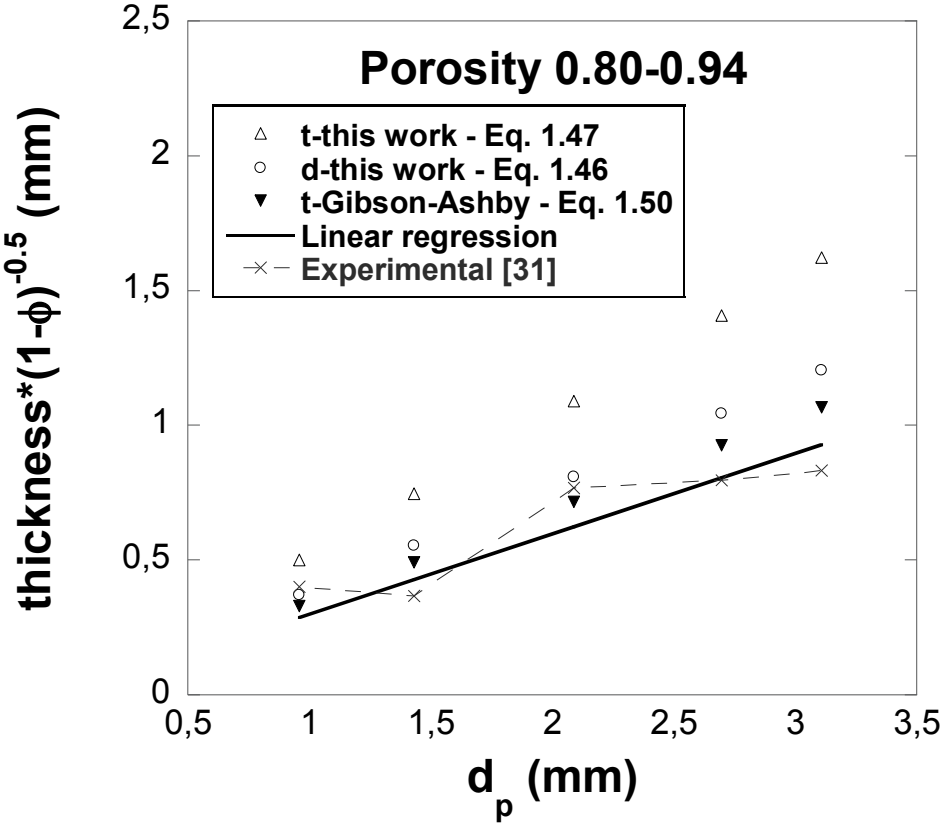

Figure 1.24. Measured cell size vs. measured ligament thickness multiplied for the factor $(1-\varphi)^{-0.5}$.

Data from Fuller et al. [31], with their linear regression, and predictions by eqs. 1.46, 1.47 and 1.50 of the struts thickness times the factor $(1-\varphi)^{-0.5}$, with the porosity ranging between 0.80 and 0.94, are reported in fig.1.23. In this case too one can remark that cylindrical correlation 1.50 fairly well matches the linear regression of the data in the 0.80 - 0.89 porosity range, in good agreement with results obtained with the Bhattacharya et al. data [13] for a porosity less than about 0.90, even though

the tendency to overestimate the thicknesses is exhibited (see fig. 1.24 for data in the range 0.80 - 0.89).

Slightly different, nevertheless, is the case for a porosity in the range between 0.89 and 0.94, presented in fig.1.25. Equation 1.46 still works well, except that for the two samples with smaller cells that are in good agreement also with the triangular model (eq.1.47).

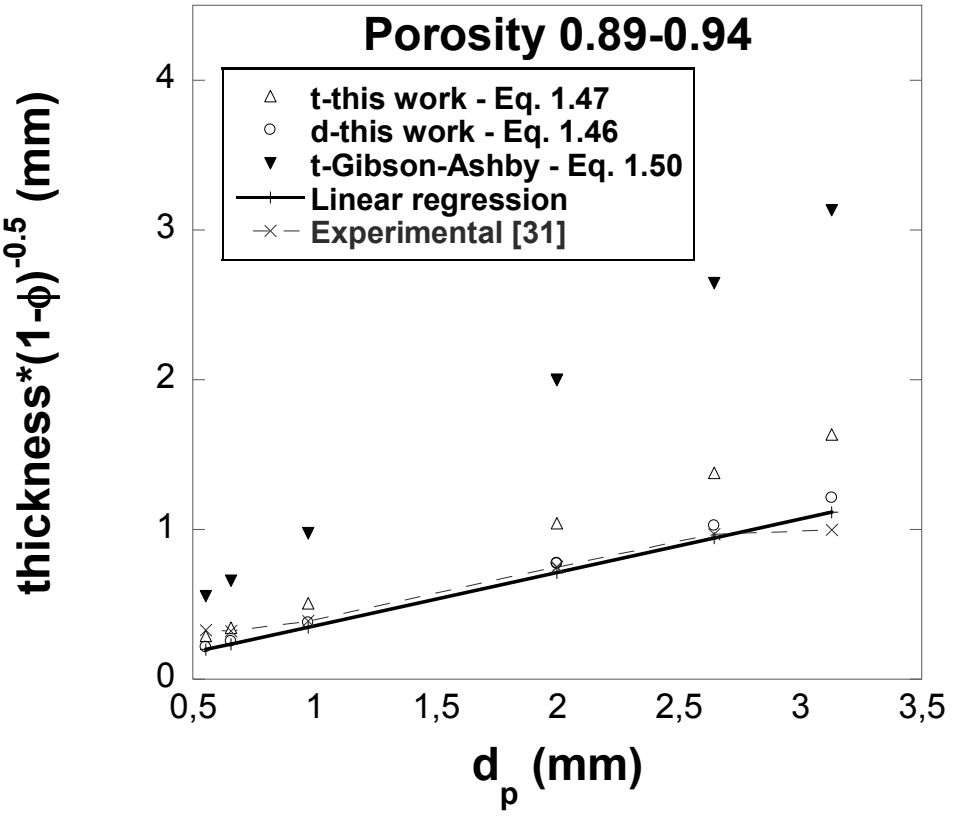

Figure 1.25. Measured cell size vs. measured ligament thickness multiplied for the factor $(1-\varphi)^{-0.5}$.

We can conclude that, provided the cells size, d_p, is known, eq.1.46 for a cylindrical correlation (or, with very little difference, the Gibson-Ashby eq.1.50) should be used for porosities less than about 0.89 - 0.90, while the triangular correlation (eq.1.47) should be employed for porosities in the 0.94 - 0.97 range.

For porosities larger than 0.97, the inner-concave triangular eq.1.49 is recommended. Furthermore, for porosities in the range 0.89 – 94 the mixed circular-triangular correlation (eq.1.48) seems to be the best, even though, for data by [24, 25] the cylindrical correlation well matches measured values also in the 0.89 - 0.94 range.

It is worth underlining that the proposed porosity ranges and the relatives suggested correlations agree very well with those presented by Bhattacharya et al. [21] and by Huu et al. [17]. It is, however, important to remark that in both papers the effect of the strut cross-sections and the differentiation of the morphological models are limited to triangular and cylindrical cross-sections and, above all, are based on a pentagonal dodecahedric cell instead of the tetrakaidecahedric one.

In conclusion, results herein obtained confirm that such experimental observations on the strut profile are very well compatible and, till a refined level, with TD cell, too.

1.14 Validation of the proposed correlations among the strut thickness, the porosity and the windows diameter

Now the above proposed correlations among the significant parameters and windows diameter, eqs. 1.35, 1.36, 1.42, the classical Richardson et al.'s correlations (eqs.1.24) and Inayat's correlations (eqs.1.26 – 1.28) for various values of the porosity, will be validated, comparing them with experimental results taken from the literature. It is worth reminding that, when the cross section of the strut is a mix of a cylinder and a triangular prism, reference can be made to the average value of predictions from eqs. 1.35 and 1.36.

A review of the experimental results reported in the literature was presented by Huu et al. [17], who compared them with predictions by a model based on a pentagonal dodecahedric cell. They are presented in Table 1.7.

However, not all of the above mentioned data have been used in the present work. As a matter of fact, data taken from Giani et al. paper [19] have not been accounted for since they are the result of measured values of the strut thickness and of the specific surface predicted numerically by means of the cubic geometrical model proposed by Lu et al. [32].

Table 1.7. Morphological parameters of various foams samples [17].

Source	Porosity, ϕ	d_w, (μm)	d_s, (μm)	S_v, (m^2/m^3)
Lu et al.[32]	0.96	500	92	
	0.96	1000	190	
	0.96	2000	360	
	0.92	500	110	
	0.92	1000	215	
	0.92	2000	440	
	0.88	500	130	
	0.88	1000	250	
	0.88	2000	490	
Du Plessis et al.[33,34]	0.973	254	47	
	0.975	423	54	
	0.978	564	54	
Stemmet et al.[35]	0.931	2450	553	
	0.932	612	138	
	0.936	314	66	
Groβe et al.[20, 36] (Outer porosity)	0.757	1096	258	1229
	0.745	1232	422	1247
	0.760	745	154	1974
Huu et al.[17] SiC foam	0.91	1326	405	
	0.90	1200	456	
	0.915	392	140	

	0.91	1053	225	
	0.88	750	226	
Huu et al. [17] PU foam	0.96	1259	303	
	0.955	893	284	
	0.98	591	120	
	0.97	797	166	
Buciuman and Kraushaar-Czarnetzki [25]	0.834	1500	680	
	0.864	1550	550	
	0.947	1580	430	
	0.799	950	300	
	0.851	959	280	
	0.884	940	270	
	0.897	980	260	
	0.767	580	220	
	0.837	620	20	
	0.844	630	180	
	0.797	340	150	
	0.849	360	90	
	0.872	370	70	
	0.827	210	90	
	0.878	250	40	
Moreira and Coury [37]	0.94	2300		1830
	0.88	800		1920
	0.76	360		2340
Incera Garrido et al. [10] (Outer porosity)	0.772	1933	835	675
	0.751	1192	418	1187
	0.766	871	319	1437
	0.761	666	201	1884
	0.812	2254	880	629
	0.814	1131	451	1109
	0.807	851	330	1422
	0.801	687	206	1816
	0.719	1069	460	1290

On the other side, experimental data for alumina Al_2O_3 and SiSiC ceramic foams obtained by Inayat et al. [26] and Grosse et.al [20], have been added to experimental values from Table 1.7 and are presented in Table 1.8 and 1.9, respectively.

In the Figure 1.27-1.32, as for the preceding case, the measured thicknesses and the calculated ones by means of the various correlations considered are plotted, after the multiplication for factor $(1-\varphi)^{-0.5}$, versus the windows diameter d_w.

Measured and predicted values of the ligament thickness times the factor $(1-\varphi)^{-0.5}$ as a function of the windows diameter, d_w, for different porosities, are reported in figs.1.27-1.32.

Table 1.8. Morphological parameters of some SiSiC foam samples used to test correlations [7].

PPI	d_w, (μm)	d_s, (μm)	φ (Outer)	S_v, (m^2/m^3)
10	1800	0.701	0.853	732
20	1297	0.480	0.873	858
30	1030	0.399	0.862	1136

Table 1.9. Morphological parameters of some Al_2O_3 and SiSiC foam samples used to test correlations [20].

PPI (material)	d_w (μm)	d_s (μm)	φ (Outer)	S_v (m^2/m^3)
10 (Al_2O_3)	1974	1007	0.688	639
20 (Al_2O_3)	1070	651	0.719	1260
10 (Al_2O_3)	1796	944	0.773	664
20 (Al_2O_3)	955	509	0.745	1204
30 (Al_2O_3)	847	391	0.754	1474
45 (Al_2O_3)	781	138	0.763	1884
10 (Al_2O_3)	1952	809	0.812	629
20 (Al_2O_3)	1137	544	0.813	1109
30 (Al_2O_3)	860	273	0.793	1520
45 (Al_2O_3)	651	217	0.783	1816
10 (SiSiC)	2181	695	0.865	477
20 (SiSiC)	1603	470	0.867	683

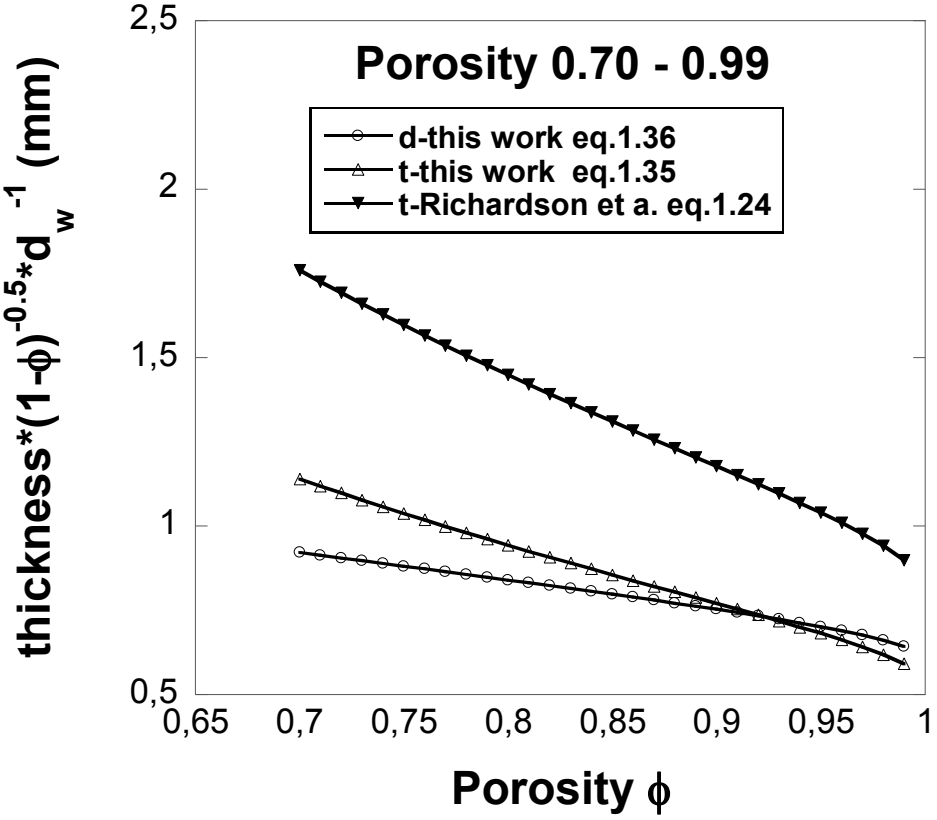

Figure 1.26. Theoretical ratio $d * (1-\varphi)^{-0.5}/d_w$ vs. the porosity.

All the equations clearly show that the quantity $d * (1-\varphi)^{-0.5}$, where d is the strut thickness, does not depend on d_w linearly as is the case for the correlations involving the pore size parameter, d_p. In fact, as in fig.1.26 it is plain that the ratio $d * (1-\varphi)^{-0.5}/d_w$ depends on the porosity, φ. Anyway as shown the dependence of this ratio with the porosity is fairly weak, above all for the cylindrical case and for that of Richardson, and above all if the values of porosities are comprised in limited intervals with values at below of about 0.97. So, especially in order to compare the cylindrical model, the Richardson's model and the Inayat's model among them, in

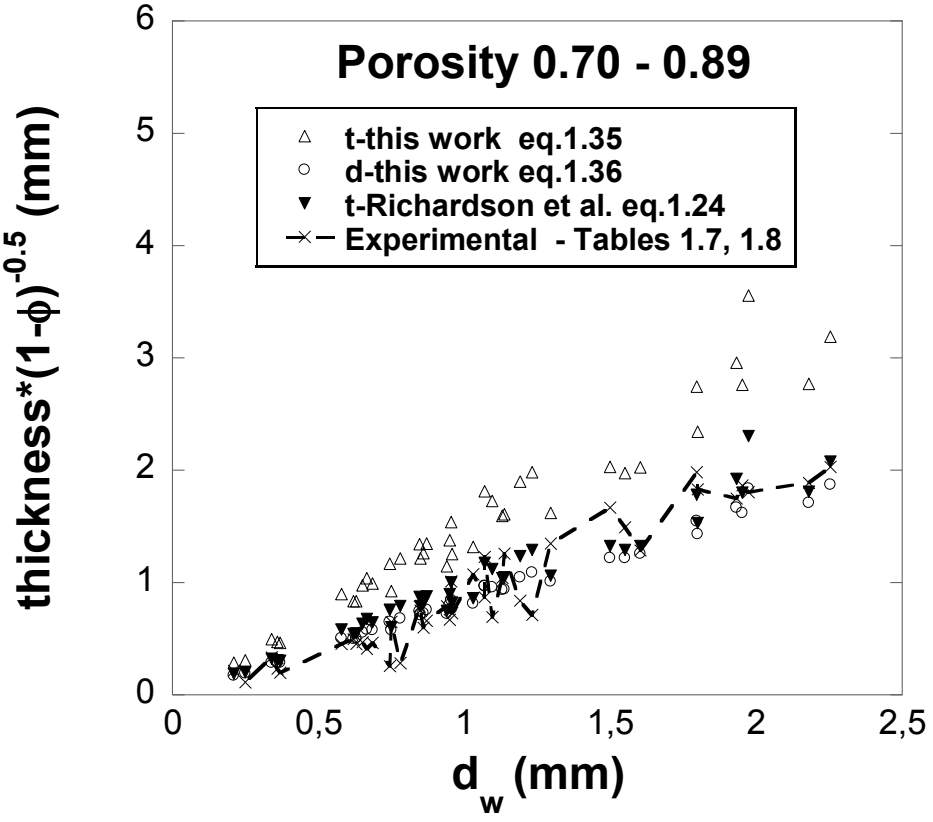

Figure 1.27. Measured windows size vs. measured ligament thickness multiplied for the factor $(1-\varphi)^{-0.5}$.

restricted intervals of the porosities (less than 0.81, in the range 0.81 ÷ 0.89 or 0.89 ÷ 0.94, for example) a linear regression can represent an acceptable good reference to validate predictions with experimental data (specially for cylindrical and triangular model herein proposed as it is shown in fig.1.26).

The totality of data (Table 1.7-1.8) and predictions of the triangular model (eq.1.35), cylindrical model (eq.1.36), Richardson et al.'s model or Inayat's triangular apparent

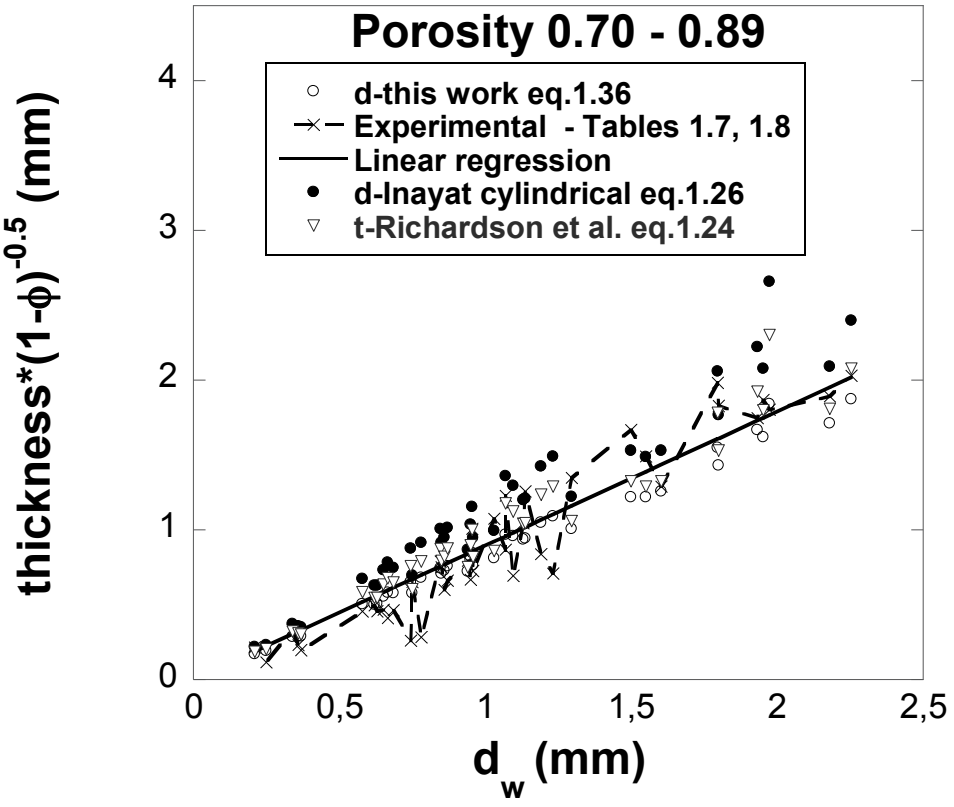

Fig. 1.28. Measured windows size vs. measured ligament thickness multiplied for the factor $(1-\varphi)^{-0.5}$.

model (eq.1.24) and Inayat et al.'s cylindrical model (eq.1.26), for porosities less than 89%, are presented in fig.1.27.

The predictions for the triangular model have not been reported and a best linear regression is added in fig.1.28, where the three models seem to work fairly well, even though predictions for the cylindrical model (eq.1.36) seems to work better (together with Richardson's model), while Inayat's cylindrical model seems to work worse than the others.

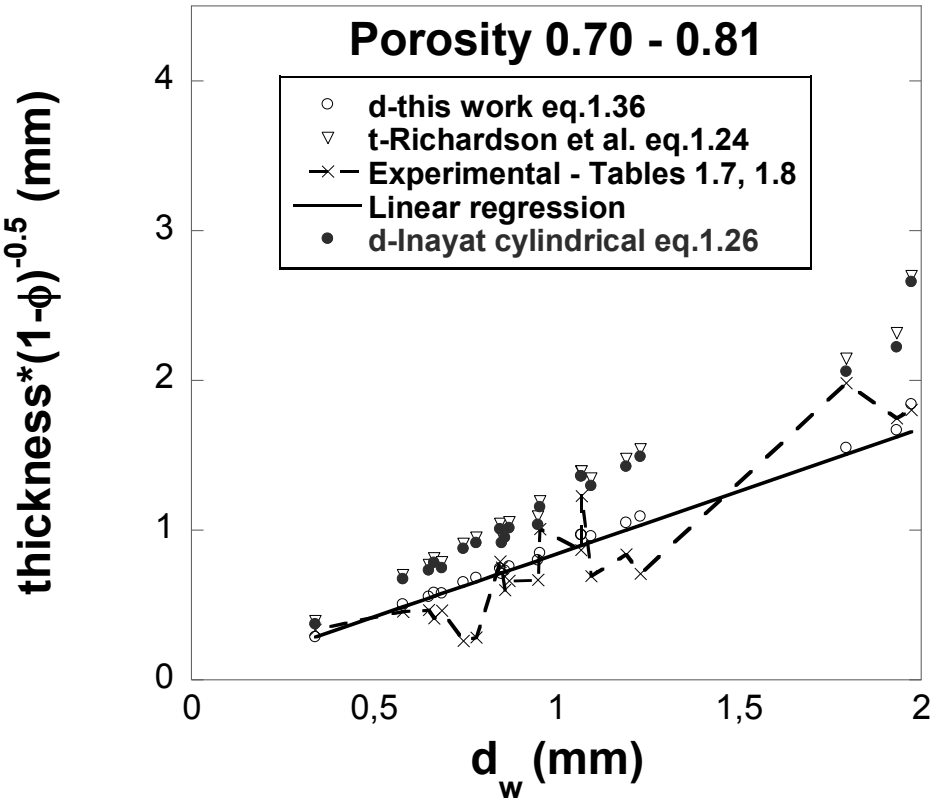

Fig. 1.29. Measured windows size vs. measured ligament thickness multiplied for the factor $(1-\varphi)^{-0.5}$.

Naturally the results obtained with Richardson et al.'s model could be considered consistent with a concave triangular profile at the light of Inayat et al.'s model: but, as we know this is not consistent with experimental observations [13].

The substantial agreement between the prediction of the cylindrical model herein proposed and experimental data is furthermore confirmed if, accounting for th

already mentioned dependence of the ratio $d*(1-\varphi)^{-0.5}/d_w$ on the porosity, the experimental values are split in two sub-ranges of the porosity: 0.81 ÷ 0.89 and 0.70

÷ 0.81. In the latter porosity range the agreement between the best linear regression and the predictions of the cylindrical model is confirmed, whereas for the former porosity range the Inaya et al.t's model predictions seem to fit only slightly better than the correlation 1.36 (cylindrical model of this work). However it should to be underlined that splitting the porosity into intervals is only speculative because no substantial difference in the cross-section profile has been experimentally observed in actual foams for porosities less than 0.89.

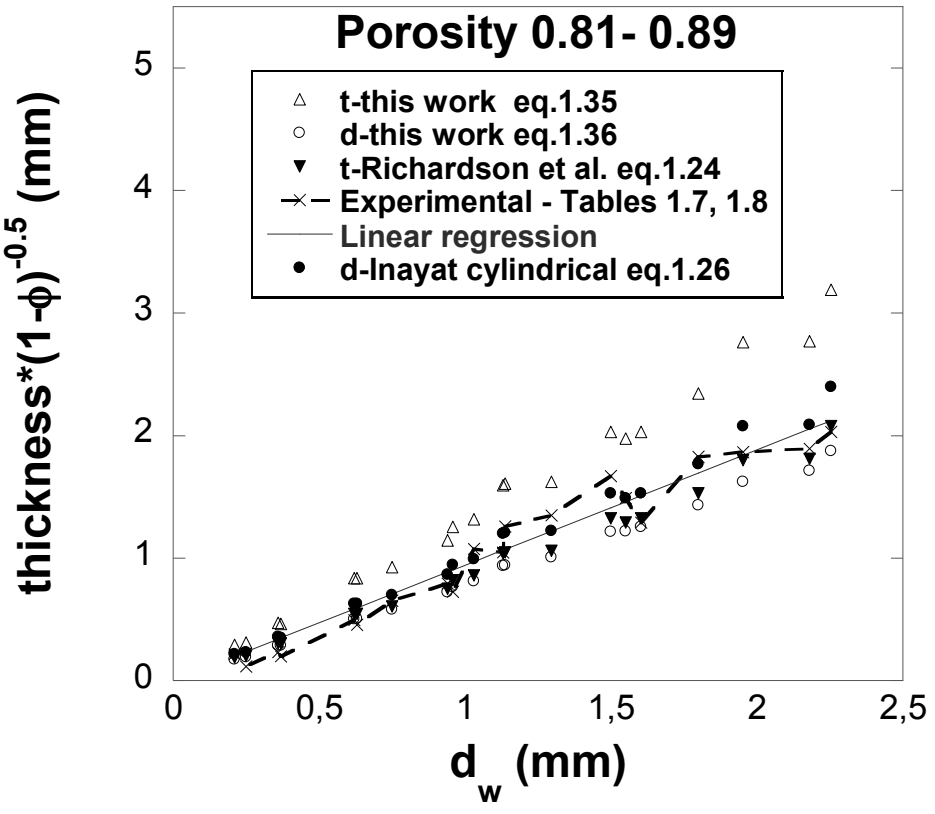

Fig. 1.30. Measured windows size vs. measured ligament thickness multiplied for the factor $(1-\varphi)^{-0.5}$.

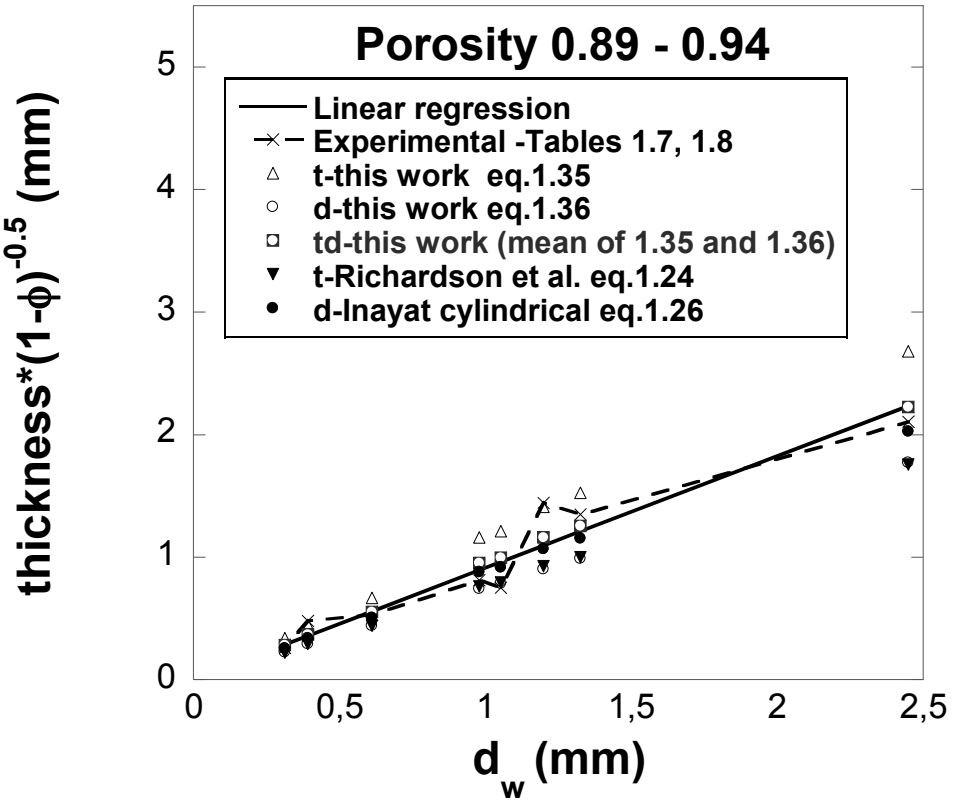

Fig. 1.31. Measured windows size vs. measured ligament thickness multiplied for the factor $(1-\varphi)^{-0.5}$.

Therefore, predictions obtained using eq.1.36 and reported in fig.1.28 can be considered more coherent with experimental data for a cylindrical cross-section and for porosities less than about 0.89.

The three correlations exhibit a fairly good prediction capability, the difference among the predicted quantities being rather small.

In Figure 1.31 instead are shown experimental data and theoretical predictions for the porosity in the range 0.89÷0.94 and the linear regression of the data. As it possible to

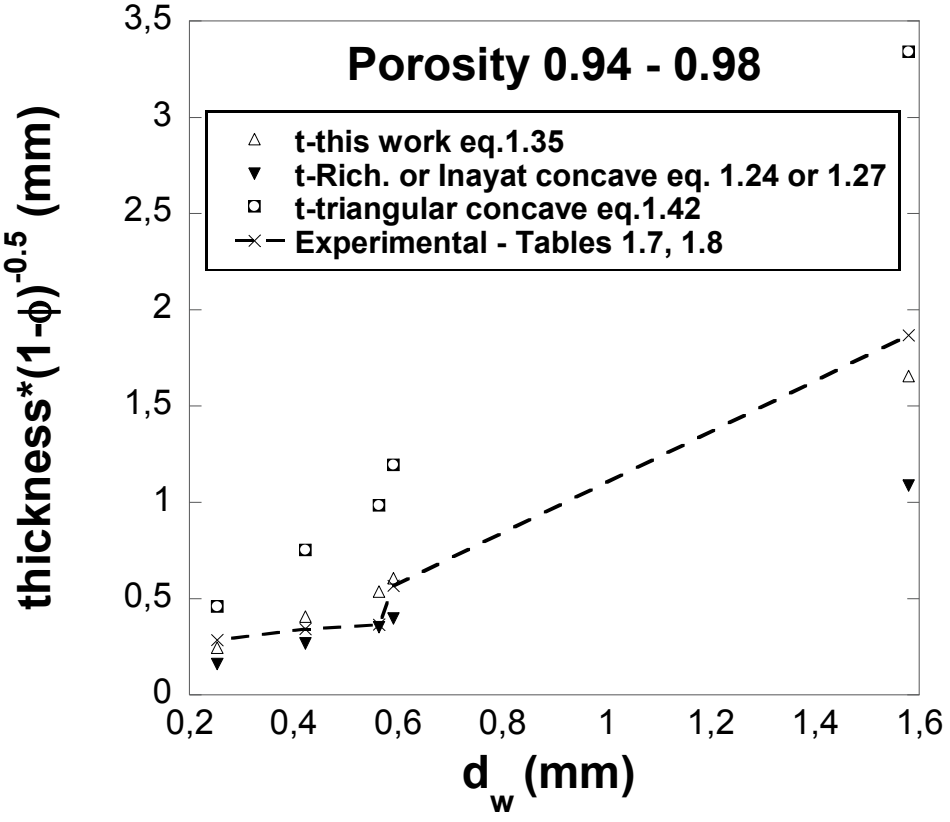

Fig. 1.32. Measured windows size vs. measured ligament thickness multiplied for the factor $(1-\varphi)^{-0.5}$.

see the theoretical values which better match to the measured values are in this case those obtained with Inayat's cylindrical model and those obtained using a mixed model (cylindrical-triangular) by means of the average of the eq.1.35 and eq.1.36. In particular this last mixed model is in better concordance with the experimental observation. The Inayat's correlation truly works only slightly worse in this range,

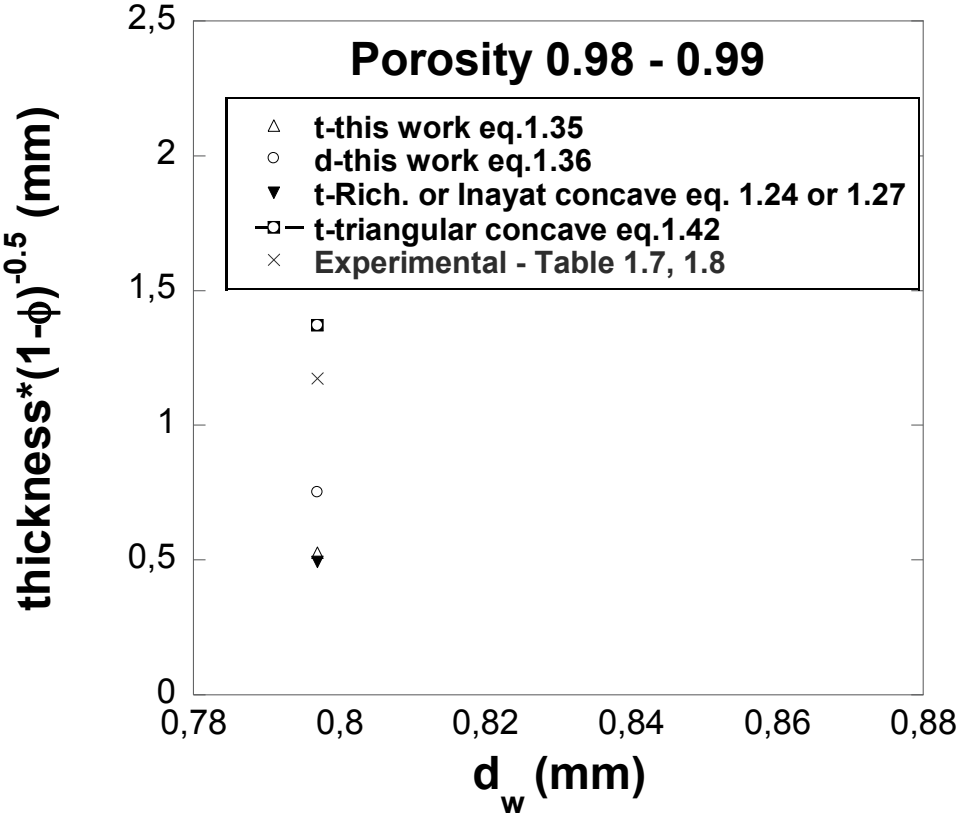

Fig. 1.33. Measured windows size vs. measured ligament thickness multiplied for the factor $(1-\varphi)^{-0.5}$.

but should imply, again, that a cylindrical strut should be assumed till to values of the porosity as great as 0.94, in contrast instead with the experimental relevance reported in literature.

Data in fig.1.31 refer to the 0.89÷0.94 porosity range. The best agreement with the measured values is exhibited by the predictions obtained with the Inayat's cylindrical model and those obtained using a mixed model (cylindrical-triangular) by averaging

eqs.1.35 and eqs.1.36. The mixed model shows the best agreement with the experimental data. The Inayat's correlation truly works only slightly worse in this range, but this should imply, again, that a cylindrical strut should be referred to up to a 0.94 porosity, in contrast with the experimental data reported in the literature.

Finally, the adequacy of the approach herein proposed is further confirmed in the 0.94 ÷ 0.98 and 0.98 ÷ 0.99 porosity ranges. Foremost in the 0.94 ÷ 0.98 range the triangular correlation (eq.1.35) clearly matches very well the data. The Richardson et al.'s and the triangular Inayat's correlations coincide and their agreement withmeasured values is not good, as fig.1.32 points out. It also notes that in this range of very high porosity (0.94 ÷ 0.98) a linear regression is not a very good fit for the data as evident also in the fig.1.32.

One can remark that also for the data taken from the literature, with known window diameter and porosity, eqs.1.35, 1.36 and 1.42 work generally better than predictions by Inayat et al. and Richardson et al. for high porosities ($\varphi > 0.80$), specially in order as to the capability to predict the dependence of the cross-section shape variation n the porosity. They are also fully justified from a geometrical point of view differently from the other correlations herein discussed that seems to be justified at most under a strictly empirical point of view.

To conclude, the unique value of the measured thickness for porosities larger than 0.98, is reported in fig.1.33, that exhibits the prediction of our concave triangular correlation (eq.1.42) to be largely the best, also if it is not yet optimal.

In conclusion of this section it is worthwhile remembering that a morphological model has been introduced and discussed that is the basis for the evaluation of the interface (solid-fluid) area per unit volume, S_v, an important morphological characteristic of a foam, that widely affects the radiative and convective heat transfer.

1.15 Prediction of the area of the interfacial surface per unit volume: indirect method

The simpler method to obtain an useful expression of the specific surface area, S_v, namely of the interface area per unit volume of foam, is to derive it by means of the correlations which link the length and the thickness of the strut to the windows diameter.

The unit cell or the REV (Representative Elementary Volume) of the idealized foam is assumed to be tetrakaidecahedric in this work. In order to evaluate the useful surface per unit volume, i.e. the surface directly involved in the convective and radiative heat transfer, reference is made to outer (open) porosity, φ. As it was pointed out in section 1.2, it coincides with the total porosity, φ_t, when the struts are not hollow, just like it is assumed in the present work; in the opposite case reference has to be made to the following equation

$$\varphi = 1 - \frac{V_{strut}}{V_0} = 1 - \frac{V_s + V_{hollow}}{V_0} \equiv 1 - \rho^* \tag{1.55}$$

where a suitable fictitious apparent density ρ^* is introduced.

It is worth reminding high pressure experimental techniques allow to measure the hollow volume of the strut body and, therefore, to distinguish between the outer or open porosity and the total porosity [10].

Practically, in order to calculate a suitable value of specific surface S_v in the various cases one must take into account the REV volume i.e. the volume of the TD that represents the cell and consider only the third of the strut perimeter (remember that for Kelvin's cell $Z_f = 30$) facing the inner part of the cell. Then the external surface of a strut belonging into a unit cell is evaluated. At the first order of approximation, that is neglecting the effect of intersection of the strut at each TD vertex (24 vertexes), it is possible to distinguish three cases, that refer to strut with cylindrical, triangular or

inner concave triangular cross-section, respectively, whose the following expressions can be used

$$Sv_c = \frac{\pi}{3} * \frac{36 * d * l_c}{11.31 * {l_c}^3} \tag{1.56}$$

$$\mathrm{Sv}_t = \frac{36 * \mathrm{t} * l_t}{11.31 * {l_t}^3} \tag{1.57}$$

$$\mathrm{Sv}_{ic} = \frac{36 * \mathrm{d_{ic}} * l_{ic}}{11.31 * {\mathrm{l_{ic}}}^3} \tag{1.58}$$

Nevertheless, with the aim to get a higher level of accuracy, a more refined model of the interface area per unit volume S_{vc} can be proposed, by evaluating more accurately the contribution of the vertexes at the interface area of the unit cell. At a second level of approximation the contribution to the outer surface of the terminal part of the cylinders at the vertex surface is currently counted three times in eq.1.56, once for each cylinder. With reference to fig.1.14 and to an l_c long strut, it must be remarked that, for each strut in the unit cell, the extremities of the three struts converging at each vertex can be considered as an x long cylinder for which the first and the third in eqs.1.30 hold for a cylindrical strut. One can take into account this overcounting effect by considering only the contribution of one strut instead of that of the all three strut at the vertex. As a consequence, since one third of the outer surface of each strut must be considered, it is possible to conclude that for any vertex an area equal to

$$A_{ext} = \frac{2}{3}\left[3\left(\frac{\pi d * x}{3}\right)\right] \tag{1.59}$$

must be subtracted from eq.1.56 so that only the contribution of one cylinder is considered as indicated by the factor 2/3 in eq.1.56. Since there are 24 vertexes, we have

$$Sv_c = \frac{\pi}{3} * \frac{36 l_c}{11.31 * {l_c}^3} - \frac{16\pi d^2}{11.31 * {l_c}^3 \sqrt{3}} \tag{1.60}$$

where reference was made to eq.1.30 for the case of cylindrical ligament.

If eq.1.60 is expressed explicitly as a function of the windows diameter and the porosity, the following correlation for the specific surface in the case of cylindrical strut is obtained

$$Sv_c = \frac{6.643 * (1-\varphi)^{0.5} - 9.805 * (1-\varphi) + 3.544 * (1-\varphi)^{1.5}}{d_w} \tag{1.61}$$

This second order expression is substantially equivalent to a correlation proposed Grosse et al. [20] for the case of a Weaire-Phelan structure with cylindrical struts and spherical knots of suitable diameter,but in their work the correlation is a function of the reciprocal of the sum of window diameter and strut thickness, d_w+d. Most important in [20] good results have been obtained for ceramic foams with coefficients obtained empirically.

Naturally, the cylindrical correlation (eq.1.61) should be used only for porosities less than 0.94, for which the cylindrical model matches well the experimental data whereas eqs.1.57 and 1.58 should be used for very high or top porosities. Unfortunately, to the knowledge of the author of this work, no measured values of specific surface are available for foams with porosities higher than 0.9.

As a matter of fact, Table 1.7 summarizes values taken from the Huu et al. [17] paper. In the Table 1.8, instead, are shown data by Inayat et al. [7] for ceramic foams: windows size, strut size and specific surface are measured with the aid of X-

ray computed tomography (CT), while open porosity is determined with He-picnometry and mercury intrusion. Finally, in the Table 1.9 there are other experimental values of specific surface measured for ceramic foams, with outer porosities, and windows diameters by means of Pycnometry and MRI or Volume Image Analysis by Grosse et al. [20].

The first order of approximation of the correlations among the interface area per unit volume, the porosity and the window diameter, for the cases of a triangular strut or a inner-concave triangular strut proposed in this work, are reported in eqs.1.57 and 1.58 in terms of strut thickness and strut length and, explicitly, in terms of porosity and windows size in the following

$$Sv_t = \frac{8.543 * (1-\varphi)^{0.5} - 8.404 * (1-\varphi)}{d_w} \tag{1.62}$$

$$Sv_{ic} = \frac{13.999 * (1-\varphi)^{0.5} - 22.5658 * (1-\varphi)}{d_w} \tag{1.63}$$

The aim is to validate the correlations proposed in this work for porosities less than 0.90, for which it is possible to make a comparison among experimental data from the literature and the predictions by the Richardson et al.'s [14] and Inayat eta al.'s [7] models, with reference to a given surface. These last papers, in particular, reported the following correlations [7, 14] which are also compared with predictions of this work

$$Sv_{rich} = \frac{5.621 * (1-\varphi)^{0.5} - 5.458 * (1-\varphi)}{d_w} \tag{1.64}$$

$$Sv_{In-c} = \frac{4.868 * (1-\varphi)^{0.5} - 4.727 * (1-\varphi)}{d_w} \tag{1.65}$$

$$Sv_{In-con-e} = \frac{6.491 * (1-\varphi)^{0.5} - 6.302 * (1-\varphi)}{d_w} \quad (1.66)$$

The Richardson's correlation always assumes a triangular cross-section whereas Inayat et. al.'s correlation adds to a triangular model other two correlations valid for the case of a cylindrical strut and a concave strut respectively. Equations 1.64, 1.65 and 1.66 have been derived from eqs.1.26 and 1.28.

In conclusion of this section it should be pointed out that the correlation proposed by Inayat et al. for the case of triangular strut is the same as that deduced by Richardson et al., and that the Richardson et al.'s correlation differs from that reported in [14], probably because of a misprint. For clearness this different expression is reported here in the following eq.1.67

$$Sv_{rich-2} = \frac{12.979 * (1 - 0.971 * (1-\varphi)^{0.5})}{d_w} \quad (1.67)$$

The expression of the specific surface is clearly indicated in [14] and it is calculated similarly to eq.1.57 with the proper values of thickness and length deduced by eqs.1.15 and 1.24: from which eq. 1.65 was obtained.

1.16 Spherical direct correlation for the area of the interfacial surface per unit volume

A morphological representation of an ideal foam based on the Kelvin's geometry is presented in this section. The inner pore of each tetrakaidecahedric cell is obtained subtracting the material contained in a sphere having a suitable diameter an ideal full TD. The above said diameter should be compatible with the measured characteristic of the foam, such as the diameter of the windows, d_w, and the porosity, φ. This approach has already been proposed by Duan et al. .[8] for the case of a pentagonal

dodecahedric cell and by Krishnan et al.[38] for a reticular configuration of Kelvin type. It is not dissimilar from that proposed in the present work but for the different calculation procedure. Moreover, goals are slightly different since Krishnan et al. [38] aim to find a simpler alternative to the procedure based on the software Surface Evolver for building up the unit cell of an ideal Weaire-Phelan representation of a foam and obtaining a good mesh for a CFD calculations. In the procedure proposed in the present work the Kelvin geometry is strictly connected with a bcc (body centered cubic) lattice if one simply substitutes a lattice site at the centre of each TD, that is the TD is a Wigner-Seitz cell associated to a bcc lattice. If such a unit-cell is placed according a bcc lattice scheme, the foam can be easily reconstructed with concave triangular strut and lumps at the intersections, as it is often observed for very high or top porosities.

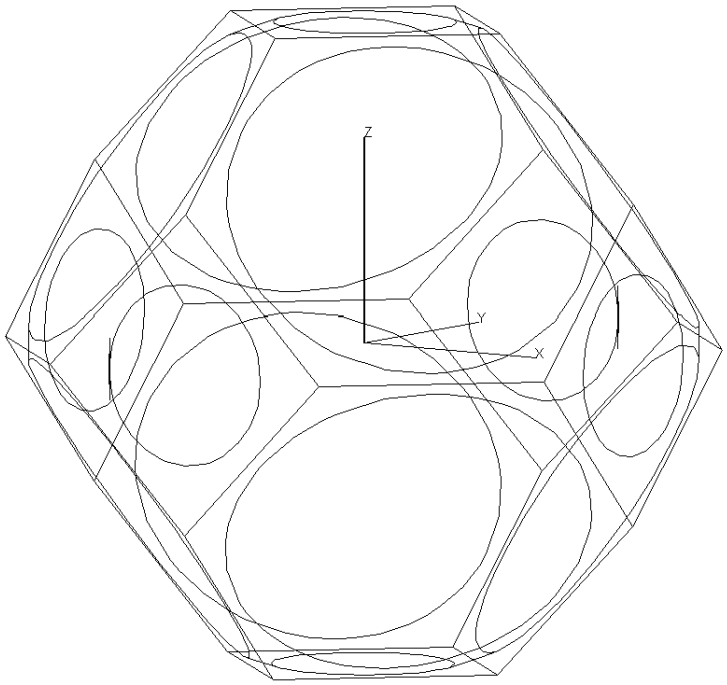

Figure 1.35. Schematic representation of the unit cell in the herein so named spherical approach .

As an example of the above mentioned procedure a TD emptied in such a manner that a sphere opens a circular window in all the faces of the TD, both squared and hexagonal, is sketched in fig.1.35. The empting does not introduce any structural failure of the reticule with the break of the struts of the unit cell.

This is not surprising as far as open cell metal foams are concerned, such as aluminum foams, since metal foams are made up by blowing gas through a molten metal, with ceramic particles as stabilizers [39] and with the formation of gas bubbles which tend to agglomerate with the liquid metal in the interstices.

The model has also been used for graphitic carbon foams [40] and herein it will be tested for ceramic foams, too. The concave struts have been observed in the foams for porosities well above 0.9., however data used for the test refer to values of the porosity below 0.9. Also for this type of foam, however, a spherical type approach has been used to model the geometry, with the aim to carry on a numerical computer simulation, and it is justified also in this case by the manufacture technique [41].

From an analytic point of view the appropriate diameter of the sphere which must hollow out the TD can be determined imposing simple suitable conditions.

With reference to fig.1.36, where the structure of a bcc lattice is sketched, it is possible to note that in the Kelvin's representation the unit ideal cell is a TD which can be obtained as the Wigner-Seitz cell of the bcc lattice. The fourteen first and second neighbourings of a lattice node are shown. The bisection of all the segments represented allows to construct the Wigner-Seitz cells. The eight hexagonal faces and the six squared faces of a TD, respectively, are thus obtained.

As consequence, a is the distance among aligned sites of a bcc lattice and it is also the distance between two facing squared face of the TD, i.e. the pore size d_p in the present work.

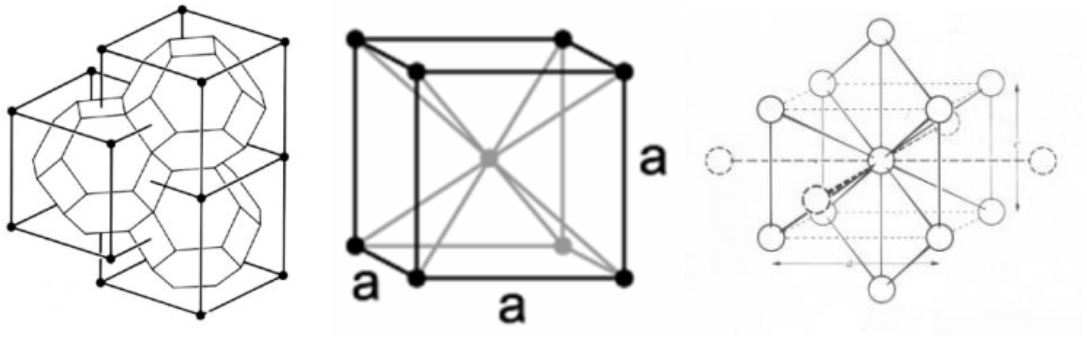

Figure 1.36. Schematic representation of a bcc lattice for which a the basic cube has edge of length *a*. The Wigner-Seitz cells are TD. At bottom the fourteen first and second neighbourings of a lattice node are shown: the bisection with planes of all the segments represented consents to construct the Wigner-Seitz cells

From an analytic point of view the appropriate diameter of the sphere which must hollow out the TD can be determined imposing the following simple suitable conditions. At first, the diameter of the circle open on the hexagonal faces of TD must be equal to the measured windows diameter, d_w, as defined in this work. In other words, the assumption is made that the measured diameter is only an average value of the hexagonal windows, the effect of the squared ones being neglected.

Significant geometrical parameters in the spherical cap of a sphere of radius r_s. A plane cuts off in the sphere a circle having a diameter d_w if a distance equal to $(\sqrt{3}/4)d_p$ is imposed between the plane and the center of the sphere. The distance between two facing windows is then equal to $(\sqrt{3}/2)d_p$). Figure.1.37 allows to conclude that

$$r_s = \frac{\sqrt{3\,{d_p}^2 + 4\,{d_w}^2}}{4} \tag{1.68}$$

The portion of the spherical surface facing the pore can be calculated remembering that the area of a spherical segment of height h and radius r_s is equal to $2\,\pi\,r_s\,h$. As a

consequence, if S_o is the area of the internal surface of an open cell and if h_{hex} and h_{sq} are the heights of spherical caps onto hexagons and squares, respectively, S_o is equal to

$$S_o = 4\pi {r_s}^2 - \left(8 * 2\pi r_s h_{hex} + 6 * 2\pi r_s h_{sq}\right) \tag{1.69}$$

$$\frac{d_p}{2} \leq r_s < \frac{3d_p}{2\sqrt{2}} \tag{1.70}$$

where the diameter of the sphere must be enough large to open the square face of the TD, as required by the first condition expressed by the eq.1.70, but also small enough to guarantee the structural consistence of the cell. In other words, it should not hollow out the struts, as required by the second condition in eq.1.71. Equivalently, the portion of the inner area of the sphere to be considered is equal to

$$S_c = 4\pi {r_s}^2 - (8 * 2\pi r_s h_{hex}) \tag{1.71}$$

$$\frac{\sqrt{3}}{4} d_p \leq r_s < \frac{d_p}{2} \tag{1.72}$$

where the first inequality in expression 1.72 guarantees that the hexagonal voids are opened and the second guarantees that only them are opened.

Remembering that the volume of unit cell (TD) is equal to

$$V_{TD} = 8\sqrt{2} * l^3 \tag{1.73}$$

we can conclude that in the two cases of completely open cells and of partially open cells the specific area are, respectively, equal to

$$S_{vo} = \frac{4\pi {r_s}^2 - \left(8 * 2\pi r_s h_{hex} + 6 * 2\pi r_s h_{sq}\right)}{8\sqrt{2} * l^3} \tag{1.74}$$

$$S_{vc} = \frac{4\pi {r_s}^2 - 8 * 2\pi r_s h_{hex}}{8\sqrt{2} * l^3} \tag{1.75}$$

The length of the edge of a TD, l, is related to the pore size, d_p, through eq.1.43,

$$d_p = 2\sqrt{2} * l \tag{1.76}$$

and fig.1.37 allows to write

$$h_{hex} = r_s - \frac{\sqrt{3}}{4} d_p$$
$$h_{sq} = r_s - \frac{1}{2} d_p \tag{1.77}$$

and it is possible to conclude that the expression of the specific surface area reported in eqs.1.74 and1.75 can be also considered as a function of the radius of the sphere, r_s, and the pore size, d_p.

A correlation which links the porosity of the foam to the parameters such as the radius of the sphere, the pore size and the windows diameter would be very useful. In fact, if for assigned porosity, φ, and windows diameter, d_w, it were possible to determine the characteristics of the cell and, mainly, the pore size, d_p, thanks to eqs.1.74, 1.75, 1.68 1.76, it would also be possible to calculate the specific surface area, in all cases.

To express the porosity as a function of the other parameters of the cell some further simple considerations are necessary. If the volume of the spherical cap cut out from the sphere are denoted with the symbols V_{sshex} and V_{sssq} in the two cases of the sphere

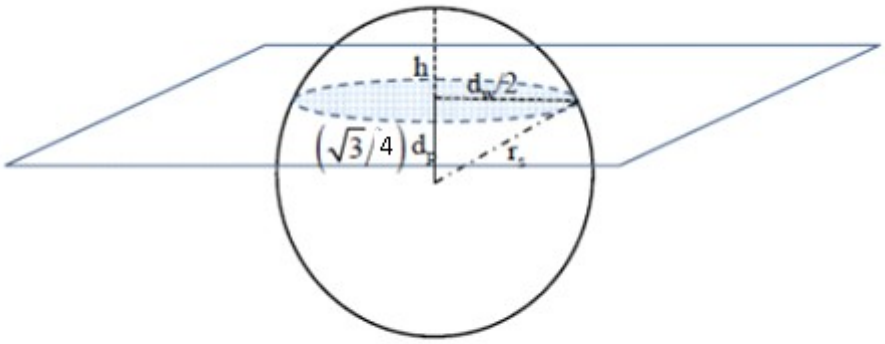

Figure 1.37. A sphere of radius r_s and a plane which cut off a spherical cap with base circle of diameter d_w. at a distance equal to $(\sqrt{3}/4)\mathrm{d_p}$ from the center.

segment onto hexagonal face and of the sphere segment onto square face, in the two considered cases of completly open cell and partially open cell we get

$$V_{os} = \frac{4}{3}\pi r_s^3 - 8\,V_{sshex} - 6\,V_{sssq}$$
$$V_{cs} = \frac{4}{3}\pi r_s^3 - 8\,V_{sshex} \tag{1.78}$$

Furthermore, geometrical considerations permit to write

$$V_{sshex} = \pi h_{hex}^2 (r_s - \frac{h_{hex}}{3})$$
$$V_{sssq} = \pi h_{hex}^2 (r_s - \frac{h_{sq}}{3}) \tag{1.79}$$

and, since it is possible to write

$$\varphi = \frac{V_o}{8\sqrt{2} * l^3}$$
$$\varphi = \frac{V_c}{8\sqrt{2} * l^3} \tag{1.80}$$

in the cases of the completly open cell and the partially open cell, if eqs.1.76 ÷ 1.79 are substituted into eq.1.80 the following two implicit equations are obtained in the two considered cases, respectively

$$(-6 - 4\sqrt{3})\pi d_p\left(d_w{}^2 + \frac{3d_p{}^2}{4}\right) + \pi(4d_w{}^2 + 3d_p{}^2)^{3/2} + d_p{}^3((2 + \sqrt{3})\pi + 4\varphi)) = 0 \tag{1.81}$$

$$-\sqrt{3}\pi d_p\left(d_w{}^2 + \frac{3d_p{}^2}{4}\right) + \pi\left(d_w{}^2 + \frac{3d_p{}^2}{4}\right)^{3/2} + d_p{}^3\left(\frac{\sqrt{3} * \pi}{4} + \varphi\right) = 0 \tag{1.82}$$

Equations 1.81 and 1.82 must be used when the disequations 1.70 and 1.72 are verified. They are substantially conditions onto the ratio of the sphere radius and the pore size, that, for an assigned windows diameter, can be transformed in suitable conditions on the porosities ranges. Imposing the appropriate conditions on the values of r_s, h_{hex} and h_{sq} in the limiting cases before substituting them into eq.1.80, it is possible to determine the applicabilty ranges of eqs.1.81 and 1.82, respectively.

The range of application of eq.1.81 is

$$0.6802 \leq \varphi < 0.9395 \tag{1.83}$$

obtained under the conditions $r_s = (\sqrt{3}/4)d_p$ and $h_{sq} = 0$ for the first inequality and by the conditions $h_{sq} = 0$ and $h_{hex} = d_p/2 - (\sqrt{3}/4)d_p$ for the second inequality.

The range of application of eq.1.82 is

$$0.9395 \leq \varphi < 0.9945 \tag{1.84}$$

obtained under the condition $r_s = (3/4\sqrt{2})d_p$.

In conclusion for assigned windows diameter, d_w, porosity, φ, and pore size, d_p, the implicit equations 1.81 or 1.82, can be solved numerically for this spherical model which, in turn, through eqs.1.68, 1.76 and 1.77 permits to evaluate the specific surface, S_v, with the aid of eqs. 1.74 and 1.75. In this paper the numerical procedure has employed the *Mathematica* software [42].

However, the applicability conditions of eqs.1.83 and 1.84 and the above cited experimental observations on the geometrical profile of the strut cross-section and the conclusions at the end of the previous sections suggest that the present spherical model can likely be applicable almost in the high range of porosity (0.97 ÷ 0.99) of the eq.1.84. Unfortunately, as it will be shown in next section, the available measured values of the surface per unit volume, S_v, found in the literature, refer to porosities less than 0.9 so that the eq.1.81 and 1.75 can be used and tested only in this range: i.e. exactly that which the author estimate less coherent and adapt.

1.17 Validation of the proposed correlations to calculate specific surface of a foam S_v

All the correlations proposed in the preceding sections for the prediction of the specific surface, S_v, are a function of the windows diameter, d_w, and of the porosity, φ, since, apart from its importance, all the measured values found in the literature and

reported in Table 1.7 and 1.9 refer to foams whose windows diameter and not pore size is known.

The triangular correlation, eq.1.62, the triangular inner-concave eq.1.63, the spherical described in the preceding section 1.16 are first considered. The reason is simply that, as anticipated in the previous section for the spherical model, in principle and on the basis of the images of real foams (ref.[16]) so like on the basis of the conclusions of the sections 1.13-1.14 those correlations are those that should

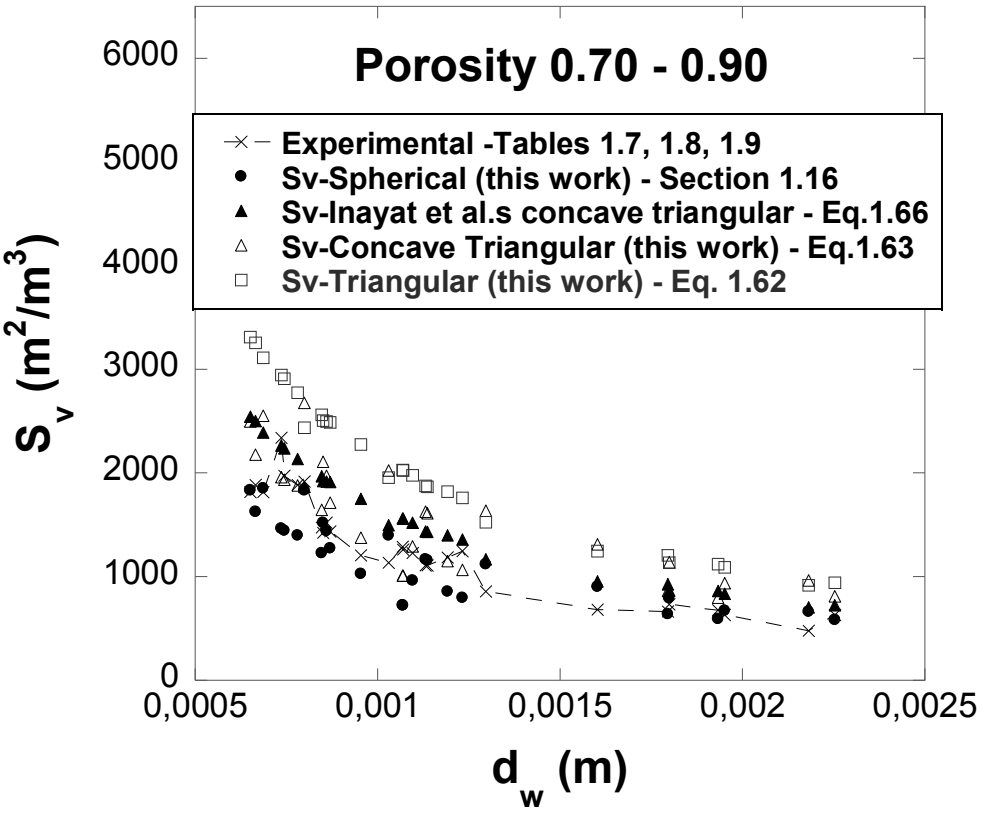

Fig. 1.39. Measured windows size vs. specific surface.

not fit well to the experimental data because it refers to geometrical profiles observed at more higher values of the porosity. At contrary, as confirmed by our analysis of the experimental data of the section 1.13-1.14 it is waited that, for porosity less than 0.90 how are those in the Table 1.7 and 1.9 generally the cross-section of the profile of the strut is circular, or that, as a minimum, this has not a cross-section with concave profile; which should then exclude the predictive capability of the spherical model or of the inner concave correlations of the eq.1.63 or 1.66.

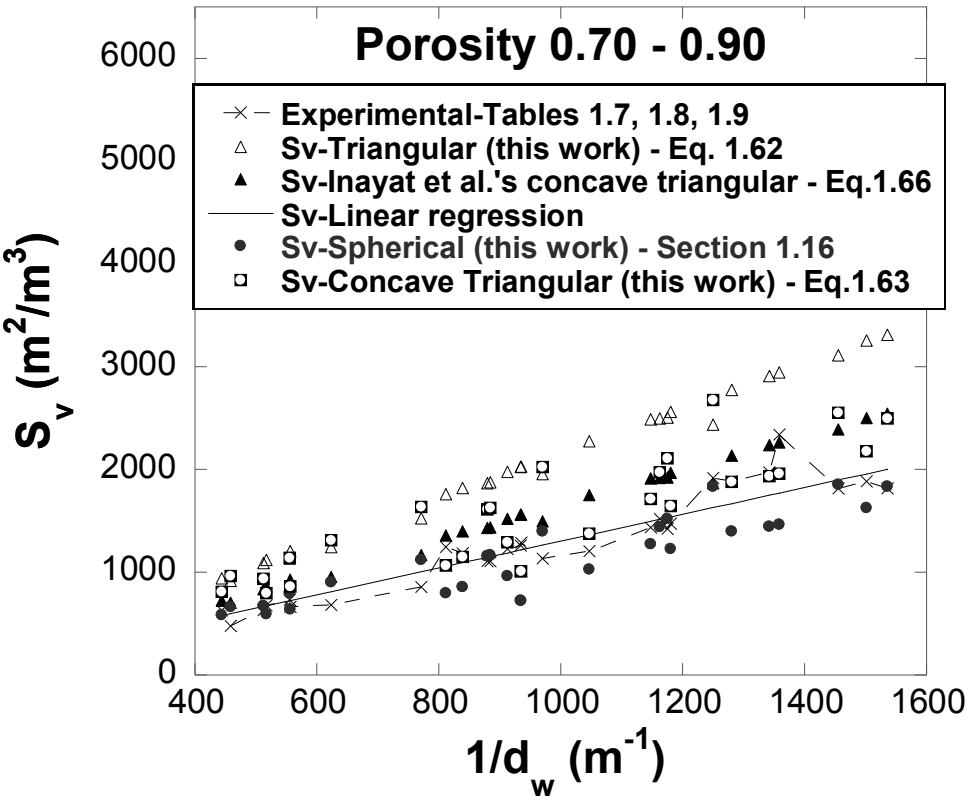

Fig. 1.40. Reciprocal of the measured windows size vs. specific surface.

Experimental and predicted values of the specific surface, S_v, as a function of the window diameter, d_w, for porosities less than 0.9, are reported in fig.1.39.

The specific surface area as a function of the window diameter, with experimental data taken from Table 1.7, and 1.8 and predictions of the Inayat et al.'s cylindrical model (eq.1.66), triangular model in this work (eq.1.62), concave-triangular model in this work (eq.1.63), spherical model in this work (eqs. 1.81 and 1.82)., in the 0.89÷0.94 porosity range, is reported in fig.1.39.

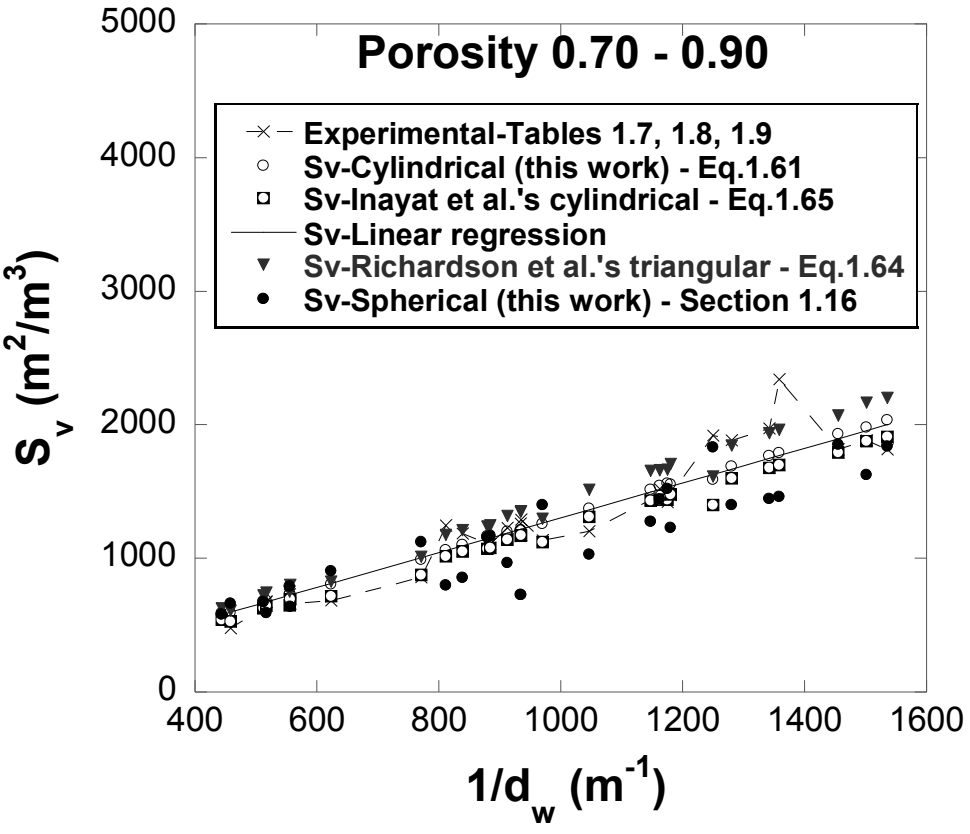

Fig. 1.41. Reciprocal of the measured windows size vs. specific surface.

Somewhat surprisingly the spherical correlations work better than the concave correlation, which, in turn, seems to work better than the concave Inayat et al.'s ones. However, the agreement is in all cases better than that for the triangular correlation that, it is again worthwhile to underline, is a first order approximation that does not take into account the contribution of the lumps; it can easily explain the overestimation of the specific surface area.

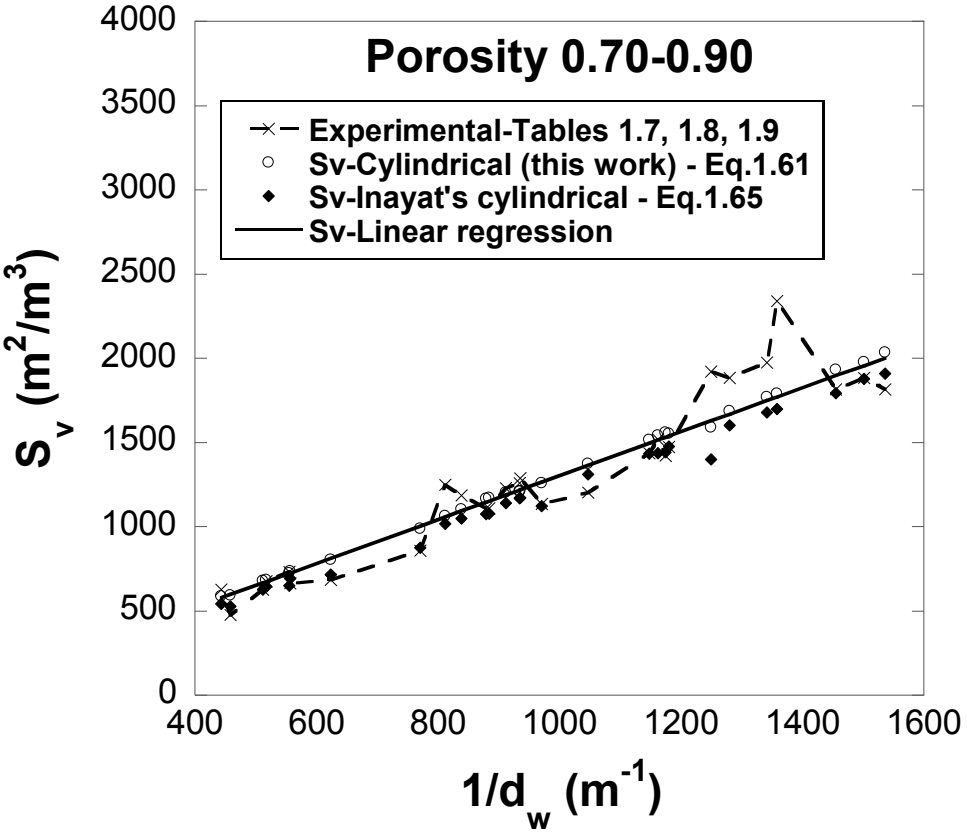

Fig. 1.42. Reciprocal of the measured windows size vs. specific surface.

A more detailed analysis is possible if the specific surface area is represented as a function of the reciprocal of the window diameter. Therefore, specific surface area as a function of the reciprocal of the window diameter, with experimental data taken from Table 1.7, 1.8 and predictions of the Inayat's cylindrical model (eq.1.66), triangular model in this work (eq.1.62), concave-triangular model in this work (eq.1.63), spherical model in this work (eqs. 1.81 and 1.82), the linear regression of the data, in the 0.70÷0.90 porosity range, is reported in fig.1.40.

The specific surface area as a function of the reciprocal of the window diameter, with experimental data taken from Table 1.7, 1.8 and predictions of the Inayat's cylindrical model (eq.1.65), Richardson et al.'s triangular model (eq.1.64), cylindrical model in this work (eq.1.61), spherical model in this work (eqs. 1.81 and 1.82), the linear regression of the data, in the 0.70÷0.90 porosity range, is reported in fig.1.41.

It should be pointed out that eq.1.64 makes implicit reference to triangular struts, without any limitations in the porosity range for its application. On the contrary, the other two predicting correlations for cylindrical struts apply for porosities lower than 0.9, according to Bhattacharya et al. [13] and according to the results herein obtained (see sections 1.13-1.14).

Figure 1.41 clearly shows that the triangular concave and the spherical models are the best among those chosen and work acceptably even though they were designed for larger porosities. One can also notice that all the models exhibit a nearly linear trend even though the corresponding correlations exhibit a dependence on the porosity; on the contrary, the triangular concave model shows a marked sensivity to porosity variations that alone can to explain the larger scattering of data.

Also the experimental data are largely scattered, as it was to be expected considering the difficulty in measuring the specific surface, the roughness of the surface, the irregularities of the structure and the different measuring techniques used. Again a linear regression has been proposed for these data implicitly admitting that the

dependence of the surface per unit volume S_v on the porosity is negligible according to the theoretical models considered, as fig.1.41 points out, except for the triangular model, that exhibits the worst prediction of measured data.

Figure 1.42, where the same quantities as those in fig.1.41 are reported, apart from predictions of eq.1.64 and sections 1.16, shows that the cylindrical correlation herein proposed (eq.1.61) matches very well with linear regression of the data, that is, the agreement of such correlation with experimental data is certainly the best one. Also the Inayat's cylindrical correlation works well, even though worse than the other. In any case, however, it has been already underlined that in the author opinion such a correlation has a doubtful theoretical base and gives incoherent results.

1.18 Conclusions

In this chapter the morphology of the actual open-cell foams have been reviewed.

Some geometrical idealizations of the actual random reticular structure are possible. Polyhedral solids as cubes, tetrakaidecahedrons (TDs), pentagonal dodecahedrons (PDs) are considered useful basic units of an idealized, but yet realistic, structure which resembles to a typical ceramic or metallic foam.

The ligaments of the reticular structure are located where there are the edges of polyhedrons and can be either hollow or not. Their cross-sections are assumed to be circular, triangular or concave triangular as many experimental evidences clearly show. The thickness of struts is then appropriately defined, taking into account their cross sections.

The typical and useful correlations used in the literature link the main morphological parameters of the foams, such as the porosity, the strut thickness, the strut length, the cell size or the windows size with a functional relation, according to the assumed basic unit geometry. In particular, since only polyhedra which fill the space without overlaps neither voids have been considered, for the case of PD cell, a suitable

correlation has been taken from the literature which reduces it to an equivalent cubic structure.

The principal and conventional morphological correlations have been considered and studied and new correlations have been proposed. Furthermore. correlations which express the functional dependence of the interfacial surface area per unit volume on the windows diameter and the porosity have been presented, taking into account the different cross-sections in different porosity ranges.

Finally, all correlations and experimental data have been compared.

The results show that:

- differently from what is reported in the literature, a clear distinction has to be made between the cell size and the windows size and, therefore, different correlations have been proposed as a function of them;
- four ranges of porosity can be distinguished (0.70 ÷ 0.90, 0.90 ÷ 0.94, 0.94 ÷ 0.97, 0.97 ÷ 0.99,) each of them implying a different cross-section and, then different correlations, must be used and have been successfully used;
- in agreement with the previous conclusion and with experimental data, the predicted cross-sections tend to transform first from circular into triangular and , then, into concave triangular with the rise in the porosity;
- the herein proposed correlations generally agree with experimental data better than correlations found in the literature;
- the cylindrical correlation of the interfacial surface area per unit volume proposed in this work gives the best prediction of experimental data in the allowed (< 0.90) porosity field of investigation.

This more accurate modeling of the foam morphology can become useful when a realistic geometric representation of the open-cell foams is needed.

2 Radiative heat transfer in open cells metallic and ceramic foams

2.1 State of art

2.1.1 Introduction

Thanks to the technological progress and to the recent development in the areas of processing, manufacturing, analysis and design of the open cell foams (metallic, ceramic or carbon based), these materials are nowadays widely used in a large number of structures and systems. Their specific thermo-mechanical characteristics, in particular in terms of stiffness-strength ratio, lightness, tortuosity, good flow-mixing capability, high surface area density (i.e. surface area of the solid-air or solid-fluid interface per unit volume) which, for metal foams, is in the 1.000 ÷ 3.000 m^2/m^3 range and can reach values as high as 8.000 m^2/m^3 after compression [43], are very useful in many cases [44–46].

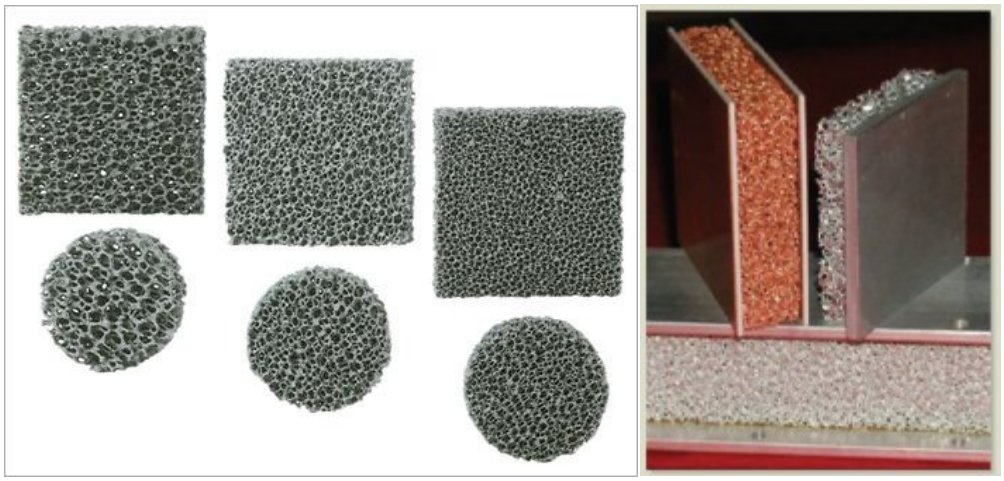

Fig. 2.1. Ceramic foams burners (on the left) and metal foams brazed or soldered to a substrate to form heat sinks (on the right).

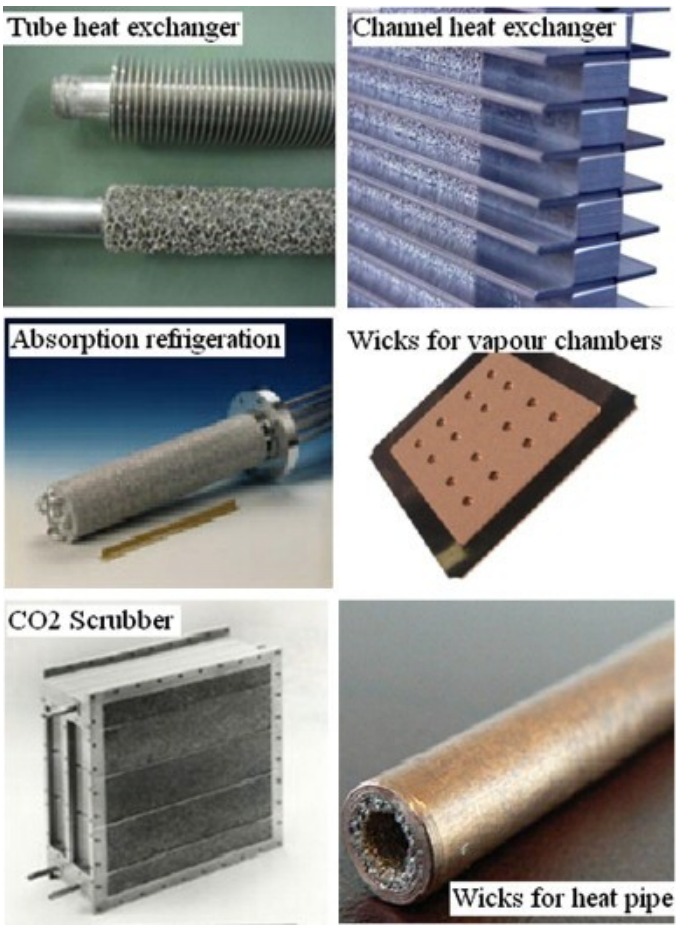

Figure 2.2. Some examples of metallic foams applications.

In fact, the efficiency of the foams removing heat is unique and attractive in a great variety of industrial sectors and practical or scientific applications where heat transfer is important, from the solar thermal or thermochemical applications [47–61] to the thermal control of electronic systems, where high heat fluxes must be removed [43] and to automotive and aeronautic sectors [62–64]. In all these applications the lightness and low density requirements, stiffness/strength of the structures together with low production costs are very important.

Ceramic [65, 66] and metallic foams [44, 45, 66, 67] are widely used in many applications, such as thermal insulation and protection systems in aircrafts (specially

C/SiC, SiC/SiC) [65]; molten-metal and diesel-engine-exhaust filters [68, 69]; porous radiant burners [70]; catalyst supports [71]; volumetric absorbers in receivers of concentrator solar systems for thermal applications or thermochemical reactors [47–49, 54]; fire barriers [72]; compact heat exchangers [32]; impact-blast energy absorption systems; sound absorbers; electrodes for electric battery; catalytic reactors for biodiesel [44,45]; matrices for absorption and desorption; steam reformers for

fuel cells, wicks for heat pipes and vacuum chambers [43, 73–82]. Some examples of applications f open cell foams are reported in figs. 2.1 and 2.2.

In most of the previously mentioned applications the good knowledge of the thermal behavior of the foam is essential. Moreover, they generally imply high temperatures and, thus, the radiative heat transfer plays a significant role and, therefore, it must be accounted for.

2.1.2 Modeling of the radiative heat transfer: analytical, numerical and experimental analysis

The analysis of the radiative heat transfer in heterogeneous and porous media, where the opaque phase is usually solid, is complex. In fact, the absorption, the emission and scattering of radiative energy by the solid phase occur, and, strictly, they depend not only on the porous structure of the phase, which is inherently randomly distributed in the fluid phase, but also on its optical properties, that are hardly available at high temperature.

Porous or heterogeneous materials can be classified as semi-transparent or dispersed media and their radiative characteristics can be evaluated by means of an analytical or numerical modeling of the heat transfer together with an experimental approach based on direct measurements of the reflectance and the transmittance or, alternatively, on a ray-tracing Monte Carlo simulation [83, 84].

In general, two orders of problems must be addressed for the dispersed materials: the determination or, better, the modeling of the radiative energy transfer in the heterogeneous media, in terms of a suitable solution of the radiative transfer equation (RTE) that, in turn, can be adequately and variously formulated and the determination of the fundamental radiative properties that affect the heat transfer [85].

Two methods are commonly used to account for the foams microstructural level.

The first consist in building analytical models of the medium in such a way that they link the geometry and the pore level, i.e. the microstructure of the foam or of the dispersed phases (one or more, transparent or not) of the medium, to the radiative properties of an equivalent continuum medium i.e. a pseudo-continuum. Subsequently, the related RTE, or the RTEs, are solved at the continuum level, analytically or numerically. In order to solve the RTE, a continuous standard formulation or, alternatively, a discrete formulation can be adopted, that make use of a continuous or discontinuous representation of the medium, respectively. Analytical methods and Monte Carlo simulation are usually used in the two formulations, respectively.

The second consists in directly simulating, at the pore level, the radiation heat transfer.

In any cases, however, in the most part of works the validity of geometrical optics is assumed (since wavelengths of the involved radiation generally can be assumed to be far shorter than the characteristic dimension of the solid scattering elements) together with the assumption of independent scattering particles [85].

The theoretical and experimental approaches to the models of radiative heat transfer in foams are reviewed in [43] and in [85].

In a semi-transparent continuum or pseudo-continuum medium the radiative energy transfer is governed by the already mentioned RTE. For a participating medium, i.e.

a scattering, absorbing and emitting medium, a radiative balance can be made, that describes the radiative intensity field $I_\lambda(r,\ \hat{s})$ within the enclosure containing the medium as a function of vector position, $\boldsymbol{r}$, the unit direction vector, $\hat{\boldsymbol{s}}$, and wavelength, λ. Taking into account the contributions in all directions and all wavelengths it obtains

$$\frac{dI_\lambda(r,\hat{s})}{ds} = -\beta_\lambda I_\lambda(r,\hat{s}) + \kappa_\lambda I_{\lambda b}(r,\hat{s}) + \frac{\sigma_\lambda}{4\pi}\int_{4\pi} I_\lambda(r,\hat{s}')\ \Phi_\lambda\ (\hat{s}',\hat{s})d\Omega' \tag{2.1}$$

$$\beta_\lambda = \sigma_\lambda + \kappa_\lambda \tag{2.2}$$

where

- σ_λ is the *monochromatic scattering coefficient*, which quantifies the energy flux removed and redirected by the material from the incident direction without absportion,
- κ_λ is the *monochromatic absorption (emission) coefficient,*
- β_λ is the *monochromatic extinction coefficient*, that represents the fraction of radiative intensity that is removed by a pencil of rays around a certain direction $\hat{\boldsymbol{s}}$ by scattering or absorption per unit length in that direction.

All the listed quantities are measured in m^{-1} and their reciprca represent the mean free path of a photon before it is scattered, absorbed or extinct. In addition, the *single scattering albedo*, $\omega_\lambda = \sigma_\lambda/\beta_\lambda$ is frequently used and measured.

The term $I_{\lambda b}(\mathbf{r},\hat{s})$ in the equation 2.1 is the black body intensity whilst the third term containing the integral take into account the radiant energy per unit time that moving from all directions are by scattering redirected in direction $\hat{s}$.

Equation 2.1 is a formulation of the radiant energy balance at a local level and the *phase function of scattering*, $\Phi_\lambda(\hat{s}', \hat{s})$ [83, 84] describes (but it is not equal to) the probability that radiation moving from the direction $\hat{s}'$ is scattered in the direction $\hat{s}$. We have the following normalization condition

$$\frac{1}{4\pi}\int_{4\pi} \Phi_\lambda\,(\hat{s}', \hat{s})\mathrm{d}\Omega' = 1 \tag{2.3}$$

Referring to a one-dimensional problem for which the temperature gradient exists only (or substantially) in the direction of the z axis, the relation between $I_\lambda(r, \hat{s})$ and the total radiation heat flux parallel to the gradient is obtained by integrating over all the directions

$$q_r^z(z) = 2\pi \int_0^\infty \mathrm{d}\lambda \int_{-1}^{1} \mathrm{I}_\lambda(\mathrm{z}, \mu)\mu\mathrm{d}\mu \tag{2.4}$$

where $\mu = \cos(\theta)$, θ is the polar angle about the z direction and cylindrical symmetry holds.

As a consequence, in order to describe radiative heat transfer within a semi-transparent medium, the radiative characteristics of the medium, such as the phase scattering function and the absorption and the scattering coefficients, must be somehow obtained by means of experiments, numerical simulations, theoretical approaches to model the involved phenomena or a mix among them. For example, theoretical approaches can use either a combination of the geometric optics and of the diffraction theory or alternative methods, such as Mie theory based on Rayleigh scattering or Rayleigh-Debye-Gans scattering from the others [85–87], as a function of the ratio of the wavelength to the typical dimensions of the target. Results of radiation transmitted through, reflected by or scattered by the foam, together with the solutions of RTE and the simulations by means of numerical-analytical techniques

based on Monte Carlo method can be used, too [88, 89]. Naturally, the Geometrical Optic Approximation (GOA) greatly simplifies the theoretical approach and it is very often used in with foams whose typical dimensions (the pore diameter, d_p, and the thickness of strut, d) are in the order of hundreds of micrometers so that the size parameter $x = \pi^* d_p/\lambda$ is typically far larger than 1 for temperatures in the order of hundreds of Kelvin degrees and GOA can be adopted.

In general, when it is necessary, porous media geometry can be implemented by geometrical approximations [87, 90–93] or using data from X-ray Computer Tomography (CT) [66, 94–99]. In any cases, the very problem is the determination of the radiative characteristics of the pseudo-continuous medium. Tancrez and Taine [100] proposed a method to directly identify the absorption and scattering coefficients and the phase function starting from their physical definitions. With the usual geometrical optical approximation and assuming a porous medium with statistically isotropic distribution, a Monte Carlo ray tracing method, for a sufficiently large number of rays, was used to evauate the significant radiative parameters. The same method was applied for the evaluation of extinction and absorption coefficients with anisotropic phase function in highly porosity metallic or ceramic foams. The morphology at the microstructure level necessary for the Monte Carlo ray tracing method was obtained in some cases with the aid of the X-ray CT [101, 102] and in other cases thanks to an appropriate geometric approximation of the open basic cell of the foams, as in [91], where both tetrakaidecahedron (TD) and pentagonal dodecahedron (PD), with a triangular cross-section of the strut, were used to represent the unit cell. Placido et al. and Coquard et al. [93, 103] developed a geometrical cell model to predict the radiative and conductive properties of various types of insulating foams, such as expanded polystyrene, extruded polystyrene and polyurethane foams with different morphologic structures. The effective thermal conductivity of foams was compared to experimental data. The same type of solution will be adopted in this work (sections 2.2 and 2.3), making use of the results and the correlations proposed and validated in Chapter I. This approach is works very well in

the design and the optimization of the engineering devices.

For scientific purposes the Monte Carlo method is frequently used in conjunction with a 3-D tomographic representation of the foam microstructure. Besides the already mentioned authors, Petrasch et al. [94] investigated theoretically the radiative heat transfer in reticulated porous ceramics, in order to define the representative elementary volume (REV), that represents from a statistical point of view the medium for the continuum domain. Subsequently, the works of Loretz et al. [95], Akolkar and Petrasch [98], Coquard et al. [99] moved along a similar approach to represent the morphology of foams.

However, the most part of the studies that analyze the media as a continuum and solve the RTE make use of the Homogeneous Phase Approach (HPA) It assumes a composite medium as equivalent to an optically homogeneous medium, in such a way that a unique RTE, like that in eq.2.1 and a unique intensity of radiation can be used to model the thermal radiation. Alternatively, the discrete modeling of foams, that overcomes some difficulties met in the HPA approach, makes reference to an equivalent medium and combines it with implicit or inverse techniques [43,88].

Baillis et al. [104, 105] used the HPA to model radiative heat transfer in carbon foams for aeronautic and spatial thermal insulation. The authors used a combination of the geometric optics laws and of the diffraction theory to study foams constituted of randomly arranged struts with triangular cross-sections. The reflectivity of the material was identified by means of bi-directional transmittance measurements in the 0.2 - 2.1 μm wavelength range. Loretz et al. [95] reviewed analytical models for the computation of radiative characteristics of foams for a wide variety of cells shapes and struts cross sections. The authors determined the model and the microstructure that best simulate the radiative behaviour of high porosity metal foams, comparing predictions by the model with results of spectrometric measurements. The above cited model was used by Coquard et al. [106,107] in the prediction of coupled conductive and radiative heat transfer in metallic foams at fire temperature. The same

authors [107] investigated the coupled conductive/radiative heat transfer for NiCrAl and FeCrAl foams and ceramic foams using thermograms obtained from laser-FLASH measurements. They concluded that three thermal parameters, the effective conductivity of the foam, the extinction coefficient and the scattering albedo coefficient (defined as the ratio of the scattering coefficient to the extinction coefficient) can roughly determine the thermal radiation behaviour in porous foams.

More recently a refined multi-phase approach (MPA) has been suggested to model heterogeneous participating media constituted of two transparent, semitransparent or opaque homogeneous phases [97, 108, 109]. The approach is substantially continuum-based and is applied both for open cell metal foams and closed cell polymer foams [97]. The MPA method is an extension of HPA and introduces two RTEs: one for the solid phase and one for the fluid phase, each-other coupled. If the boundary conditions at the interfaces of the two phases are suitably addressed and the exact morphology of the microstructure is known, the coupled equations can be solved by means of the stochastic ray tracing based on Monte Carlo method [108,109]. The morphology to solve the problem is exactly determined by means of X-ray CT which furnishes a 3-D mesh of the detailed structure. The spatial averaging theorem is applied to rigorously derive continuum-scale equations of the radiative transfer in two-phase media consisting of arbitrary-type phases in the limit of geometrical optics [109].

Going back to the methods to solve the RTE in a continuum medium (eq.2.1), it is important to illustrate one of them, the *Rosseland approximation* [83, 84], frequently used and particularly useful in the design and the optimization of heat transfer in optically thick porous media.

Details about the optically thick approximation or diffusion approximation can be found in ref. [83, 84]. Here the final steps of the approach are reported. Let η be the wave number associated to the wavelength, λ, the spectral radiative heat flux in a certain direction, that is, the heat flux within a unitary wave number range, and

perpendicular to an infinite plane at constant temperature *T* in the direction *z* is given by the following equation

$$q_{r,\eta} = -\frac{4\pi}{3\beta_\eta(T)}\frac{dI_{b\eta}}{dz} \tag{2.5}$$

that, integrated on all wave numbers, gives the total radiative heat flux

$$q_r = -\frac{4\bar{\sigma}}{3\beta_R(T)}\frac{d(n^2T^4)}{dz} \tag{2.6}$$

where $\bar{\sigma}$ is Stefan-Boltzmann constant, *n* is the refraction index of the medium and $\beta_R(T)$ is the *Rosseland-mean extinction coefficient,* defined as

$$\frac{1}{\beta_R} \equiv \int_0^\infty \frac{1}{\beta_\eta}\frac{dI_{b\eta}}{dz}d\eta \Big/ \int_0^\infty \frac{dI_{b\eta}}{dz}d\eta = \frac{1}{4\bar{\sigma}T^3}\int_0^\infty \frac{1}{\beta_\eta}\frac{dI_{b\eta}}{dz}d\eta \tag{2.7}$$

Equation 2.9, valid for an optically thick medium, i.e. for $\beta_R(T)\cdot L \gg 1$, with *L* the thickness of the foam, has the same form as the Fourier's law of heat diffusion and the Fick's law of mass diffusion, from which the alternative name of *diffusion approximation* follows. Thanks to this approximation it is possible to directly introduce a radiative conductivity

$$k_R = \frac{16n^2\bar{\sigma}\,T^3}{3\beta_R(T)} \tag{2.8}$$

in such a manner that the radiative heat diffusion can be treated as a "conduction" problem with a conductivity strongly dependent on the temperature

$$q_r = -k_R(T)\frac{dT}{dz} \tag{2.9}$$

Thanks to eq.2.8 the radiative conductivity is strictly coupled to the temperature-dependent specific anisotropic extinction coefficient $\beta_R(T)$, that is to be determined by experimental-numerical approaches [91, 95], such as inverse methods [43, 88, 108] or Monte Carlo simulations [91, 94, 95, 100–102].

In general, however, the solution of the RTE allows the evaluation of the radiative heat flux, q_r, between two parallel plates placed at distance L and at the temperatures T_h and T_c. It is then possible to calculate the k_r by means of the following eq.2.10, that is obtained integrating eq.2.9 and assuming a linear gradient of the temperature (this hypothesis is valid for samples having a small thickness)

$$k_r = q_r \frac{L}{T_h - T_c} \tag{2.10}$$

The above method has been used in the models proposed in this thesis for sufficiently thick samples. If samples aren't optically thick the radiative conductivity coefficient can depend on sample thickness, temperatures and emissivity of the cold and hot plate [110–112], as it will be discussed in sections 2.2.6 and 2.3.5.

An expression such as eq.2.10 is very useful in the solution of radiative heat transfer, especially because of the importance of the coupled conductive-radiative heat transfer in the practical applications of metallic and ceramic foams. The problem has been treated by Zhao et al. from an experimental point of view in the case of steel alloy FeCrAlY foams with various pores sizes and porosities [113]. The data of Zhao et al. have been used in this work with the aim to test two new models of radiative heat transfer, which can be considered an evolution and refinement of a Zhao et al.'s analytical approach [92], since they better predict the radiative conductivity. Also Coquard et al. [107, 110] investigated experimentally the coupled heat transfer in

metallic and ceramic foams at high temperature using the laser-FLASH technique on several sample foams of NiCrAl, FeCrAl, Mullite and PsZ. They measured the effective thermal conductivity at high temperatures and two radiative properties of the equivalent homogeneous semi-transparent materials associated with the foams (the extinction coefficient and the albedo scattering) to analyze the heat transfer. The authors concluded that the coupled heat transfer is relatively weak;[107,110] the total heat transferred through the foams can be simply obtained summing the contributes of conduction and radiation obtained separately with the Fourier expressions

$$q = -k_{eff}\frac{dT}{dz} \tag{2.11}$$

with

$$k_{eff} = k_r + k_c \tag{2.12}$$

This approximation, used also by Zhao et al. in their attempt to model the radiative heat transfer [92], greatly simplifies the problem still being accurate enough. This is also assumed in the present work (sections 2.2.2 and 2.3.2) and ensures that the approaches and the analysis proposed to evaluate the radiative heat conductivity make sense in the high temperature practical applications.

Glicksman et al. [114, 115], Lee and Cunnington [116, 117], and Caps et al. [118] modeled thermal radiation in fibrous insulations by using a diffusion approximation based on a combination of the geometric optics laws and diffraction theory. Very interesting were the works of Glicksman et al., in particular from an engineering point of view. The authors, in fact, use a type of ideal geometric approximation of the unit cell which was discussed in section 1.12 of this work, i.e. a pentagonal dodecahedron (PD) with a triangular cross-section. On the basis of empirical considerations and experiments, they suggest a correlation which links directly the

extinction coefficient to the porosity of the foam and to the pore size [110,114,115]. This approach has many common points with the approach used in this work, that is to try to determine methodologies and suitable correlations that allow to evaluate the radiative conductivity as a function of the temperature and the significant morphological parameters for a fixed geometry of the unit cell. In other words, the objective is to identifying the parameters of the foams that characterize their thermal behavior. A similar approach would be very useful in many fields of applications making easier the design and the optimization of the practical devices as recognized by other authors, too [110]).

Zhao et al. [119] developed a numerical model for the study of the radiative heat transfer in metallic foams. However, it seems to be not quite suitable in engineering applications because of the complicated optical theories which make the underlying physics implicit. Consequently, the authors, successively abandoned the effective medium approach and proposed a rather simple explicit analytical model, based on a discrete representation of foams, in order to establish functional relationships between the cellular structure and the radiative transfer characteristics, in terms of radiative conductivity of metallic foams [92]. The radiation in open-cell metallic foams is described with reference to cells having an ideal morphology. The model assumes a simple cubic cell consisting of slider cylinders as unit cell. The predicted effective radiative conductivities were compared with those of FeCrAlY foams measured by the same authors in vacuum [113]. The Zhao's et al. model was also used by Andreozzi et al. [120] to evaluate the local radiative conductivity and the effect of radiative heat transfer in a two-dimensional conductive-convective-radiative problem involving a forced fluid flow within a heated channel filled with a metallic foam. However, the test performed on the model showed that it led to inaccurate predictions of the actual heat transfer rate.

In order to improve the predictive capability of the Zhao et al.'s analytical model a numerical approach to calculate view factors and coefficients different from those

evaluated in [92] is proposed as the first step in section 2.2 of this thesis. In particular, Monte Carlo simulations [83,84,121][83, 84] realized with ray tracing software *TracePro* [122] are used to calculate the view factors which cannot be obtained by means of analytical methods [121]. Nevertheless, the predicted radiative conductivity was in the section 2.2 of this thesis 10% - 20% lower than the measured one. It is argued, in agreement with Zhao et al., that, likely, this is due to the simplified description of the foam geometrical structure [92]. Therefore, in section 2.3 of the present work the theoretical approach proposed by Zhao et al. is used to develop a radiative heat transfer model based on a more realistic representation of metallic or ceramic open cell foams. The tetrakaidecahedric (TD) geometry proposed by Lord Kelvin has been chosen as the basic unit cell of the model. The analytical method is combined with numerical simulations based onto ray-tracing Monte Carlo (MCRT) realized with software *TracePro* [122] used, again, to calculate the involved view factors, and with an iterative procedure implemented by means of the matrix algebra and the software *Mathematica* [42], used to consistently calculate the involved view factors. Then the radiative conductivity of foams has been predicted by means of the proposed model and has been compared with both the experimental results obtained on several metal foams by Zhao et al. [113] and with the values predicted by a simplified model based on a cubic representation of the foam unit cell.

Zhao et al. [92] and by Coquard et al. [110] used the Geometrical Optic Approximation (GOA), a widely used approach, that has also been adopted in the present work.

Coquard et al., in particular, accurately discussed also the often implicit assumption of Independent Scattering Approximation (ISA) [110]. They proved, in agreement with other researchers that, when $x \gg 1$ and GOA is applied, the ISA assumption is rather satisfying and can surely be adopted with little error for high porosity foams.

2.2 Simplified model of the radiative heat transfer based on simple cubic morphology: a variant of the Zhao et al.'s analytical model [92]

2.2.1 Introduction

Zhao et al. [92] proposed a rather simple explicit analytical model, based on a discrete representation of foams and on the evaluation of radiosities. Radiation in open-cell metallic foams, in terms of emissivity, reflectivity and view factors, was described, using cells with ideal morphologies. The model assumed a simple cubic cell as unitary idealized cell and predicted the correct trend of the experimentally measured conductivity versus temperature curve, although the predicted conductivity was, in general, lower than that measured.

The Zhao's et al. model was used by Andreozzi et al. [120] to evaluate the local radiative conductivity and the effects of radiation heat transfer in a two-dimensional conductive-convective-radiative problem involving a forced fluid flow within a heated channel filled with a metallic foam.

In the present section reference is made to open-cell metallic foams and to the model proposed by Zhao et al. [92], in order to improve its capability to predict a correct value of radiative conductivity for high, very high or top porosity samples ($0.80 \leq \varphi < 0.99$) where the porosity ranges are those referred in section 1.1. Coefficients in the Zhao et al.'s iteration model are recalculated and different assumptions are made to evaluate the involved view factors. When it is necessary, they are calculated by means of numerical methods based onto ray-tracing Monte Carlo method, that is more accurate than the Zhao et al.'s analytical approach. An iterative procedure is implemented by means of the software *Mathematica* [42], used to consistently calculate the view factors and coefficients. The radiative conductivity of foams is evaluated. Predictions are compared to both experimental results obtained on several metal foams by Zhao et al. [113] and predictions given by the Zhao et al.'s model

[92]. As in [92], a simplified representative elementary cubic volume of the foam is assumed, with reference to the correlations proposed by Calmidi [13,28] and the radiative heat flux is evaluated by computing radiosities and view factors.

The analytical approach proposed in this paragraph slightly modifies some coefficients of the original model. The comparison of values predicted by the proposed model with experimental results shows that they are more accurate than the values predicted by the original model.

2.2.2 Assumptions of the radiation heat transfer model

As it has been shown in section 1.1, the Weaire-Phelan cell is the ideal basic unit cell which well minimizes the surface energy per unit volume of a foam cell (fig.1.6). This is an aggregation of 8 cells, 6 constituted of 14 faces (12 pentagonal and 2 hexagonals) and 2 constituted of a pentagonal dodecahedron (PD) which represents a partition of the space without overlaps and voids. As a consequence, according to Calmidi [13, 28] (section 1.12), the microstructure of a typical open cell metallic foam can be assumed to be made up of ligaments that form a network of interconnected dodecahedric cells of characteristic size d'_p, as shown in fig. 2.3. The ligaments are randomly orientated and their length fluctuates, too. The cells are mostly homogeneous in size and shape. The ligaments are composed by metal struts and lumpings of solid material in their intersection points. The porous medium is characterized by the porosity, φ, and by the pore density that is referred to in Pores Per Inch, *PPI*, units. As concluded in the previous chapter the geometry of the cross section of the metal struts varies from a circular to a triangular shape in the 0.85 ÷ 0.94 porosity range and from a triangular to an inner concave triangular shape in the 0.94 ÷ 0.98 porosity range [123]. In the following, similarly to the assumption of Zhao et al. [92] the effect of different cross section strut geometries on radiative

conductivity is neglected and a circular section is assumed in all cases. Reference is made to a d'_s diameter of the cylindrical struts.

Since the dodecahedron is not a partition of the space without voids and overlaps and in order to simplify the modeling of the radiation heat transfer in this complex geometry, the Calmidi correlations reported in section 1.12 are used to define an equivalent open cell foam made up of uniformly distributed, equal-sized, cubic cells. In particular, reference is made to an s thick foam sample, sandwiched between two L long and W wide plates, sketched in fig.2.3. A cubic unit cell is chosen, at first, as the basic cell to represent the foam, since its simplicity allows the evaluation of approximate closed-form solutions for significant heat transfer parameters.

In the next section of this chapter, instead, a more realistic representation of the foam based on the Lord Kelvin cell will be done. In particular, the cubic unit cell, shown in fig.2.4b, is composed by equivalent cylinders of diameter d_s and length d_p, intersecting in three mutually perpendicular directions, that, for simplicity, are assumed to be parallel to the x, y, z coordinates. The sizes of the simple cubic (sc) unit cell are calculated assuming a porosity of the model foam equal to that of an idealized foam based on a pentagonal dodecahedric cell.

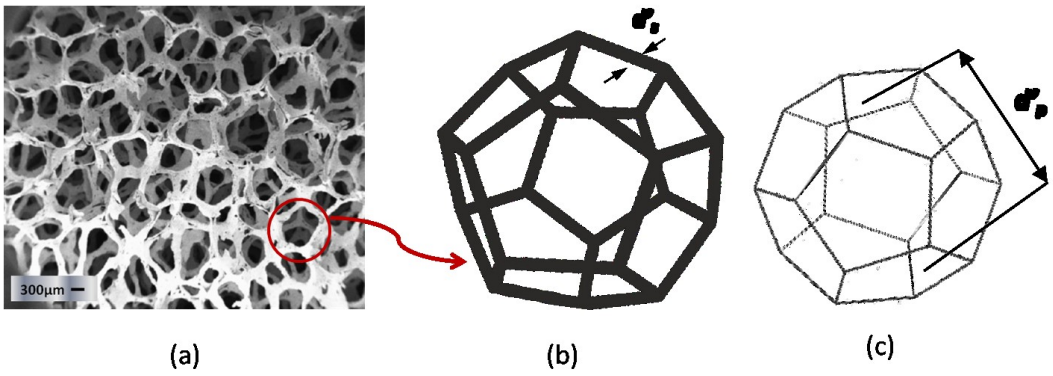

Figure 2.3. A pentagonal dodecahedron of size d_p' with ligaments of thickness d_s' is a possible ideal representation of the basic cell of the foam. This is assumed in this paragraph.

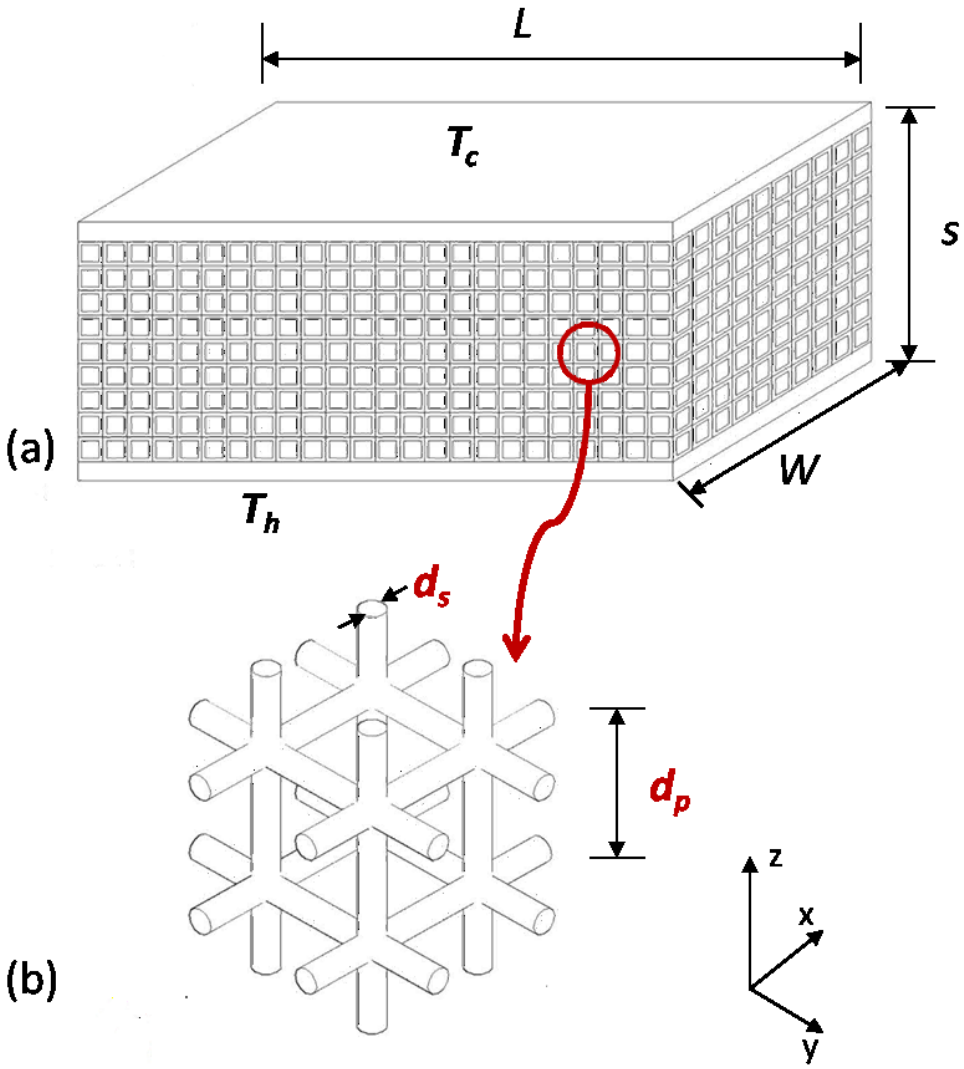

Figure 2.4. Scheme assumed to analyze the radiation heat transfer in foams (a). Calmidi [13,28] correlations of the par. 1.12 are used to reduce the actual reticular structure to a more simple cubic one (b).

The relationship between d'_p and d_p based on the same porosity was obtained by Calmidi et al.[22], as

$$d_p = 0.59\, d'_p \tag{2.13}$$

Then, the strut diameter, d_s, can be correlated to the pore size, d_p, of the cubic cell in the following way (eq.1.52)

$$\frac{d_s}{d_p} = 2\sqrt{\frac{(1 - \varphi)}{3\pi}}\frac{1}{G} \tag{2.14}$$

where $G = 1 - \exp(-(1 - \varphi)/0.04)$ is a shape function that introduces a corrective term which accounts for the dependence of the strut diameter on the porosity [28].

Both plates are thin enough as to allow to assume the top and the bottom plates to be at uniform temperatures, T_c and T_h, respectively. We also assume that T_h is higher than T_c and that the sandwich structure is under vacuum and thermally insulated at the side walls. The condition $T_h > T_c$ implies a radiation heat flux, q_r, in the positive z direction, as represented in fig.2.4. In a unit cell the top and bottom surfaces (voids) are referred as A and E, and each lateral surface is denoted as C. The twelve solid struts are labeled with numbers from 1 to 12. Note that only a quarter of each strut is included in the unit cell, the remaining three quarters belonging to the neighboring cells. Under vacuum, convection does not occur and heat is transferred by conduction and radiation. Generally, conduction and radiation are non-linearly coupled in high porosity metal foams, since radiation can be assumed to be exchanged mostly through voids of neighbouring cells. Therefore, conduction and radiation can be considered decoupled and the temperature can be assumed to depend linearly on z [92]. Assuming that the foam sample is sufficiently thick ($s >> d_p$), differences in the temperature within the unit cell can be neglected and a unique value of the temperature can be assigned at each cell in each x y plane. Finally, the grey body assumption is also made.

The objective is now to evaluate the conductivity due to thermal radiation alone, namely the radiative conductivity.

2.2.3 Analysis

The difference in the temperatures of two cells in adjacent planes along the z direction is

$$\Delta T = \frac{T_h - T_c}{N_p - 1} \tag{2.15}$$

where $N_p = s/d_p$ is the total number of cells in the z direction.

In the following, the analysis will be carried out with reference to the N_p-1 planes parallel to x y plane. Once the center-plane between planes in contact with plates at T_h (z=0) and T_c ($z = s$) is assumed as the 0 plane (reference plane), planes will be numbered from – (N_p - *1*)/2 at $z = 0$ to + (N_p – 1)/2 at $z = s$ and the temperature T of the cells in the ith plane is

$$T = \bar{T} - \frac{T_h - T_c}{N_p - 1}\,\mathrm{i} \tag{2.16}$$

where $\bar{T} = T_h + T_c$ /2 is the average temperature. The heat flux between two adjacent cells along the z direction is sustained by the temperature difference ΔT, whereas no heat is transferred along the x and y directions, where the temperature gradient is zero.

The radiative conductivity, k_r, can be evaluated by the following equation

$$k_r = q_r \frac{s}{T_h - T_c} \tag{2.17}$$

Therefore, the radiative heat flux, q_r, is now to be calculated.

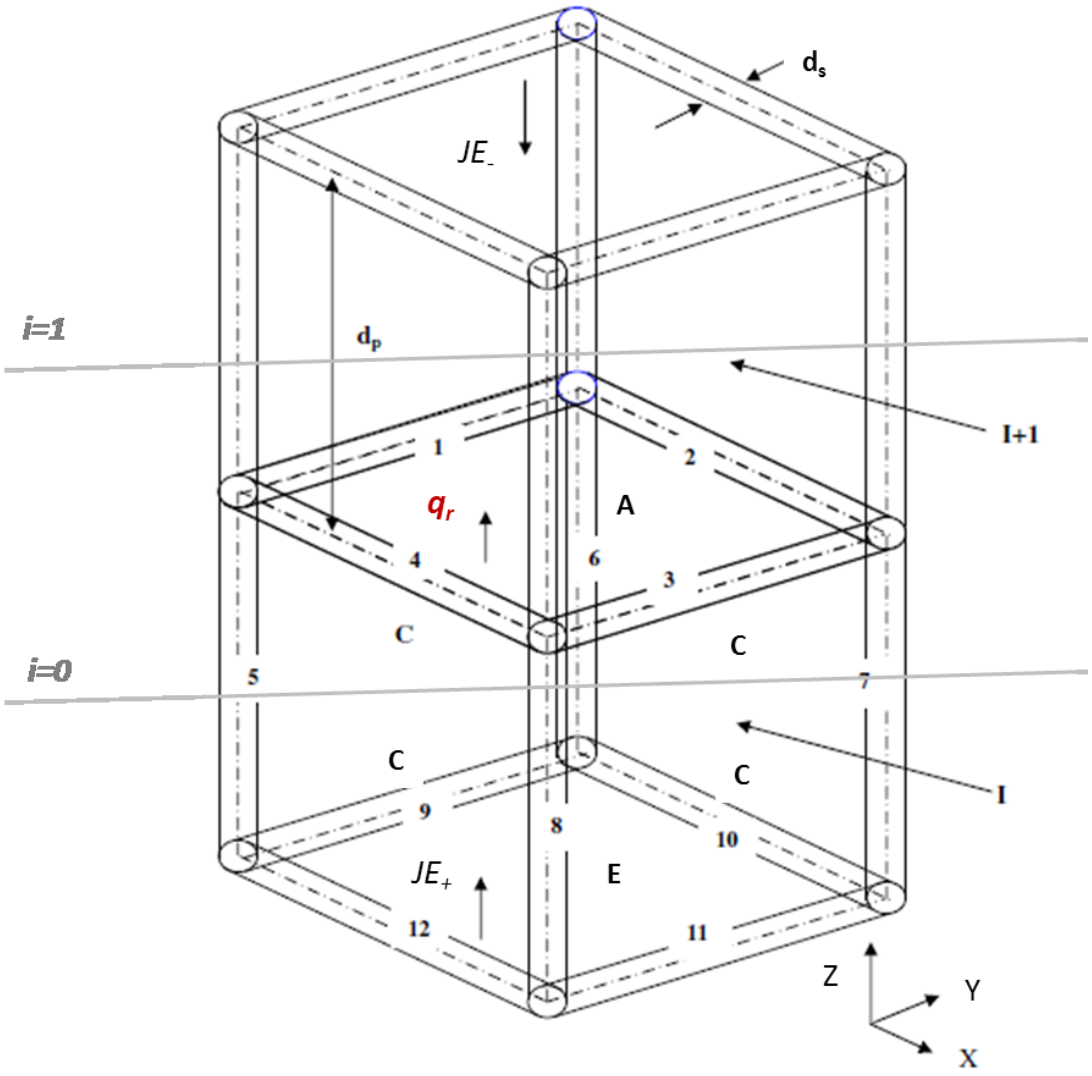

Figure 2.5. Two contiguous cells in *z* direction corresponding to two consecutive planes of cells labeled with consecutive values of the index *i*. Involved heat flux through voids A and E of each cells are shown. Heat flux direction is upward between the separation planes.

With reference to fig.2.5 and to the area A_{sq} of the square in the *x y* plane, whose side length is d_p, the radiative heat flux, q_r, can be calculated as the difference between the radiosities of the top void A, *JA,* in the opposite direction

$$q_r = \frac{(JA_{+}^{(0)} - JA_{-}^{(1)})A_A}{A_s} \tag{2.18}$$

where superscripts refer to the planes where radiation comes from and plus and minus subscripts denote the irradiation in the positive *z* direction and in the negative *z* direction, respectively.

In order to compute the radiosities $JA_{+}^{(0)}$ and $JA_{-}^{(1)}$ an iterative procedure has been implemented, that takes into account the irradiation from all the other planes, step by step, up to the farthest ones, in direct contact with the external plates at temperatures T_h and T_c. In particular, three are the contributions to the radiosity of the top surface of a cell in the reference plane: one arises directly from the radiative emission of internally faced struts, characterized by its emissivity, ε; one arises from the radiosity of the opposite bottom void, $JE^{(i)}$; one comes from the four lateral surfaces C that delimit cells in the same plane (see fig.2.5). The expressions of radiosities $JA_{\pm}^{(i)}$, $JC_{\pm}^{(i)}$, $JE_{\pm}^{(i)}$, with reference to the two directions, i.e. planes above or below the surface, are the following

$$JA_{\pm}^{(i)} = \beta_1\, \varepsilon\, \sigma\, (T(0) \pm i * \Delta T)^4 + \beta_2\, JE_{\pm}^{(i)} + \beta_3\, JC_{\pm}^{(i)} \tag{2.19}$$

$$JC_{\pm}^{(i)} = \alpha_1\, \varepsilon\, \sigma\, (T(0) \pm i * \Delta T)^4 + \alpha_2\, JE_{\pm}^{(i)} \tag{2.20}$$

$$JE_{\pm}^{(i)} = JA_{\pm}^{(i\pm1)} \tag{2.21}$$

where coefficients α_1, α_2, β_1, β_2, β_3 are a function of view factors, that will be presented in the following subsection.

As far as the farthest boundary planes, in direct contact with the external plates, are concerned, their radiosities are

$$JE_{+}^{-(Np-1)/2} = \varepsilon\,\sigma\,T_h^4 \tag{2.22}$$

$$JE_{-}^{+(Np-1)/2} = \varepsilon\,\sigma\,T_c^4 \tag{2.23}$$

Let

$$a_1 = \beta_1 + \alpha_1\,\beta_3 \tag{2.24}$$

$$a_2 = \beta_2 + \alpha_2\,\beta_3 \tag{2.25}$$

by substituting equ 2.20 into eq. 2.19, one obtains

$$JA_{\pm}^{(i)} = a_1\,\varepsilon\,\sigma\,(T(0) \pm i * \Delta T)^4 + a_2\,JE_{\pm}^{(i)} \tag{2.26}$$

By means of algebraic expressions, the coefficients a_1 and a_2 can be correlated to the geometrical characteristics of the cells through both the areas involved and the view factors between the geometric elements.

2.2.4 The calculus of the model coefficients

Coefficients β_1, β_2, β_3 as a function of view factors between of the struts and voids are

$$\beta_1 = \frac{A_s(4\,F_{5\mathrm{A}} + 4\,F_{9\mathrm{A}})}{A_{\mathrm{E}}} + \frac{11\,A_s(4\,F_{5\mathrm{A}} + 4\,F_{9\mathrm{A}})F_{ss}\,\rho}{A_{\mathrm{E}}} \tag{2.27}$$

$$\beta_2 = F_{\mathrm{EA}} + \frac{4\,A_s\,{F_{5\mathrm{A}}}^2\,\rho}{A_{\mathrm{E}}} \tag{2.28}$$

$$\beta_3 = 4\,F_{\mathrm{CA}} + \left(\frac{8\,A_{\mathrm{s}}\,F_{5\mathrm{A}}F_{9\mathrm{A}}}{A_E} + \frac{2\,A_{\mathrm{s}}F_{9\mathrm{A}}(F_{5\mathrm{A}} + F_{9\mathrm{A}})}{A_{\mathrm{E}}} + \frac{A_{\mathrm{s}}\,F_{9\mathrm{A}}(2\,F_{5\mathrm{A}} + F_{9\mathrm{A}})}{A_{\mathrm{E}}}\right)\rho \tag{2.29}$$

where $F_{\mathrm{j}\Pi}$ is the view factor between the internal faced quarter of the jth strut (j = 1 - 12) and the void Π (A, E, C*)*, A_{s} is the area of the strut surface, A_{E} is the area of the E void surface, $\rho = 1 - \varepsilon$ is the reflectivity of the metal strut, $F_{\Pi\Omega}$ is the view factor between the void Π and the void Ω and F_{ss} is the average strut-strut view factor.

In order to calculate the coefficients β_1, β_2 and β_3 two contributions are to be considered: the direct one and the reflected one, the latter being calculated by neglecting second order reflections. The former is obtained by summing up the following contributions to the radiosity of the top void A, $JA_{\pm}^{(i)}$: the Stefan-Boltzmann radiation of each internal faced quarter strut, the radiation of the faced void E, the radiation of the four lateral voids C. They are given by the first term on the right side of the eqs.2.27, 2.28 and 2.29, respectively. The latter is obtained by summing up the contributions of the radiation first emitted by the struts or irradiated by the voids E and C toward each internal faced strut surface and then reflected toward the top void A. The contributions of the reflection are represented by the second term on the right side of the eqs.2.27, 2.28 and 2.29, respectively.

The contribution of the strut emission from neighbouring cells of same order and that of the radiosity of their cell voids can be evaluated taking into account the inward

radiosity of a current C void of the reference cell. It is, therefore, necessary to express coefficients α_1 and α_2 as a function of view factors. To this aim the radiosity of a C void, $JC_{\pm}^{(i)}$, can be expressed as follows

$$JC_{\pm}^{(\mathrm{i})} = \delta_{\,1} JC_{\pm}^{(\mathrm{i})} + \delta_2\, \varepsilon\, \sigma\, (T(0) \pm i * \Delta T)^4 + \delta_3\, JE_{\pm}^{(\mathrm{i})} \tag{2.30}$$

On the right side of the eq.2.30 the first term represents the contribution to the void irradiance on C from the radiosity of other facing C voids; the second term represents the contribution of direct emission from struts both direct, i.e. from strut to void without reflections, that from strut to the void after one strut reflection (contribute of multiple reflections are neglected); the third term is due to radiosity of the bottom void E, either with or without the contribute of one reflection by the struts. The first term is frontal and has a view factor indicated as F_{CCf}; the other two are located laterally and have a view factor indicated as F_{CCl}. The coefficients δ_1, δ_2 , δ_3 can be expressed as a function of the external area of the struts, A_{S}, the area of the void, A_{E}, and the above mentioned view factors by means of the following correlations

$$\delta_1 = F_{\mathrm{CCf}} + 2F_{\mathrm{CCl}} + \left(\frac{4\, A_s\, F_{5\mathrm{A}}\, F_{9\mathrm{A}}}{A_{\mathrm{E}}} + \frac{2\, A_{\mathrm{s}}\, {F_{9\mathrm{A}}}^2}{A_{\mathrm{E}}} + \frac{4\, A_s\, F_{5\mathrm{A}}(F_{5\mathrm{A}} + F_{9\mathrm{A}})}{A_{\mathrm{E}}}\right)\rho \tag{2.31}$$

$$\delta_2 = \frac{A_s(4\, F_{5\mathrm{A}} + 4\, F_{9\mathrm{A}})}{A_{\mathrm{E}}} + \frac{11\, A_s(4\, F_{5\mathrm{A}} + 4\, F_{9\mathrm{A}})F_{ss}\, \rho}{A_{\mathrm{E}}} \tag{2.32}$$

$$\delta_3 = F_{\mathrm{EC}} + \left(\frac{4\, A_s\, F_{5\mathrm{A}}\, F_{9\mathrm{A}}}{A_{\mathrm{E}}} + \frac{A_s\, {F_{9\mathrm{A}}}^2}{A_{\mathrm{E}}}\right)\rho \tag{2.33}$$

Since, because of symmetry, the view factors F_{iA} between the strut i and the void A are equal to F_{jC} for the appropriate strut j, from eqs. 2.20 and 2.30 one can obtain

$$\alpha_1 = \frac{\delta_2}{1 - \delta_1} \tag{2.34}$$

$$\alpha_2 = \frac{\delta_3}{1 - \delta_1} \tag{2.35}$$

and, therefore,

$$\alpha_1 = \frac{\mathrm{A}}{1 - F_{\mathrm{CCf}} - 2\,F_{\mathrm{CCl}} - \mathrm{C}} \tag{2.36}$$

$$\alpha_2 = \frac{\mathrm{B}}{1 - F_{\mathrm{CCf}} - 2\,F_{\mathrm{CCl}} - \mathrm{C}} \tag{2.37}$$

where

$$C = \left(\frac{4\,A_s\,F_{5\mathrm{A}}\,F_{9\mathrm{A}}}{A_{\mathrm{E}}} + \frac{2\,A_s\,F_{9\mathrm{A}}{}^2}{\mathrm{A_E}} + \frac{4\,\mathrm{A}_s\,\mathrm{F}_{5\mathrm{A}}(\mathrm{F}_{5\mathrm{A}} + \mathrm{F}_{9\mathrm{A}})}{\mathrm{A_E}}\right)\rho \tag{2.38}$$

$$A = \frac{A_s(4\,F_{5\mathrm{A}} + 4\,F_{9\mathrm{A}})}{A_{\mathrm{E}}} + \frac{11\,A_s(4\,F_{5\mathrm{A}} + 4\,F_{9\mathrm{A}})F_{ss}\,\rho}{A_{\mathrm{E}}} \tag{2.39}$$

$$B = F_{\mathrm{EC}} + \left(\frac{4\,A_s\,F_{5\mathrm{A}}\,F_{9\mathrm{A}}}{\mathrm{A_E}} + \frac{A_s\,F_{9\mathrm{A}}{}^2}{\mathrm{A_E}}\right)\rho \tag{2.40}$$

Since $F_{\mathrm{CCl}} = F_{\mathrm{EC}}$ and $F_{\mathrm{CCf}} = F_{\mathrm{EA}}$, no further view factor needs to be introduced in addition to those already reported in eqs. 2-27-2.29.

Heat flux from each lateral C_i void toward all struts (1-12) and, thanks to the reflection toward void A, from each strut must be accounted for in eq. 2.29. Because of the symmetry (see next section) the contributes of the voids C_i are equal and they sum up, as reported in eq.17; moreover only two view factors describe the involved

thermal contact (different from zero) between the voids and the struts of the cell, F_{5A} and F_{9A}.

Similar considerations can be made when reference is made to eqs.2-31, 2.32, 2.33, for heat flux from each void C toward the other. Consequently, the coefficients in theeEqs. 2.36 and 2.40 are fairly different with respect to those analogous Zhao et al.'s equations reported in the reference [92].

2.2.5 The Monte Carlo ray-tracing and the evaluation of the view factors

View factors on which the above presented coefficients depend are now evaluated. Because of the geometrical symmetry, the following correlations hold

$$F_{5A} = F_{6A} = F_{7A} = F_{8A} \tag{2.41}$$

$$F_{9A} = F_{10A} = F_{11A} = F_{12A} \tag{2.42}$$

$$A_i \, F_{iA} = A_A \, F_{Ai} \tag{2.43}$$

In order to evaluate F_{5A} and F_{9A} view factors, cylindrical struts and planes with fixed sizes, that are directly related to the foam geometric parameters, have been considered. In particular, the above mentioned view factors were evaluate using known analytical correlations [83] and common reciprocity correlations. The software *Mathematica* [42] was used to implement an iterative routine and the numerical integration.

For the strut-strut view factors, a unique value has been used in all investigated cases, as reported by Zhao et al. [92]. However, whereas they evaluated all view

factors analytically, in the present paper an average strut-strut view factor, F_{ss}, numerically calculated, was referred to for the F_{ij}s view factors.

In the evaluation of F_{EC} and F_{EA} view factors and of view factor $F_{j\Pi}$ between the Π void perimetral struts and the void, two cases have been distinguished: low (90%) and high (95%) porosity. For the lower porosity the strut diameter, d_s, was considered not negligible and a direct numerical procedure based on the Monte Carlo ray-tracing was used to evaluate F_{EC}, F_{EA} and $F_{j\Pi.}$ This is a numerical standard procedure [83, 84, 121] and for the scope the commercial software *TracePro* was used as ray-tracer [122]. For the higher porosity (95%), instead, d_s has been neglected with respect to d_p and the aforementioned view factors were calculated as reported by Zhao et al. [92]. They proposed, as to F_{EC} and $F_{EA,}$ the following cross-relationship

$$4\,F_{EC} + F_{EA} = 1 \tag{2.44}$$

that, once the void size d_p- d_s, is assumed to be equal to d_p, gives $F_{EC} = F_{EA} = 0.2$.

The view factor $F_{j\Pi}$ was assumed to be zero, as it was proposed by Zhao et al. [92].

2.2.6 Results and discussion

In order to validate the model, predicted values of the radiative conductivity are compared with experimental results in the 300 - 750 K range, for FeCrAlY (Fe 75%, Cr 20%, Al 5%, Y 2%) metallic foams, produced via sintering route presented by Zhao et al. [113]. They used a guarded-hot-plate apparatus for the measurements under vacuum of total conductivity of steel alloy foams. The radiative contribution to the total conductivity measured under vacuum, was derived by means of the analytical model of solid conduction proposed by Zhao et al. [113]. In particular, reference is made to four samples, S3, S4, S5, S6 equal to those used by Zhao et al.

[113]. S4 and S6 had a 90% high porosity and 30 and 60 Pores Per Inch; S3 and S5 had 95% very high porosity and 30 and 60 Pores Per Inch, respectively. The characteristics of the considered foams, as measured by SEM, the nominal values of the porosity and cell size, as given by the manufacturers, are reported in Table 2.1. In all simulations, the measured morphological characteristics have been considered.

Radiative conductivity has been evaluated with a step procedure, taking into account the irradiation from all other planes (namely also orders), up to the farthest ones in direct contact with the external plates at T_h and T_c, if necessary. In fact, preliminary evaluations showed that number of orders higher than 15 must be reached to stabilize

Table 2.1. Morphological parameter of the foams studied. Data extracted from [113].

	Samples			
	S3	**S4**	**S5**	**S6**
Pores Per Inch (1/inch)	30	30	60	60
Nominal porosity (%)	95	90	95	90
Measured relative density (%)	95.9	90.7	94.5	90.8
Nominal cell size (mm)	0.847	0.847	0.423	0.423
Measured cell size (mm)	1.999	2.089	0.975	0.959
Struts diameter (mm)	0.215	0.267	0.124	0.154

the predicted value of the radiative conductivity. The radiative conductivity as a function of the number of orders, at different temperatures, for the S3 sample and a 0.6 emissivity of the solid, is reported in fig.2.6. In all simulations, however, since a high enough computation speed was checked, a number of orders equal to 25 has been considered.

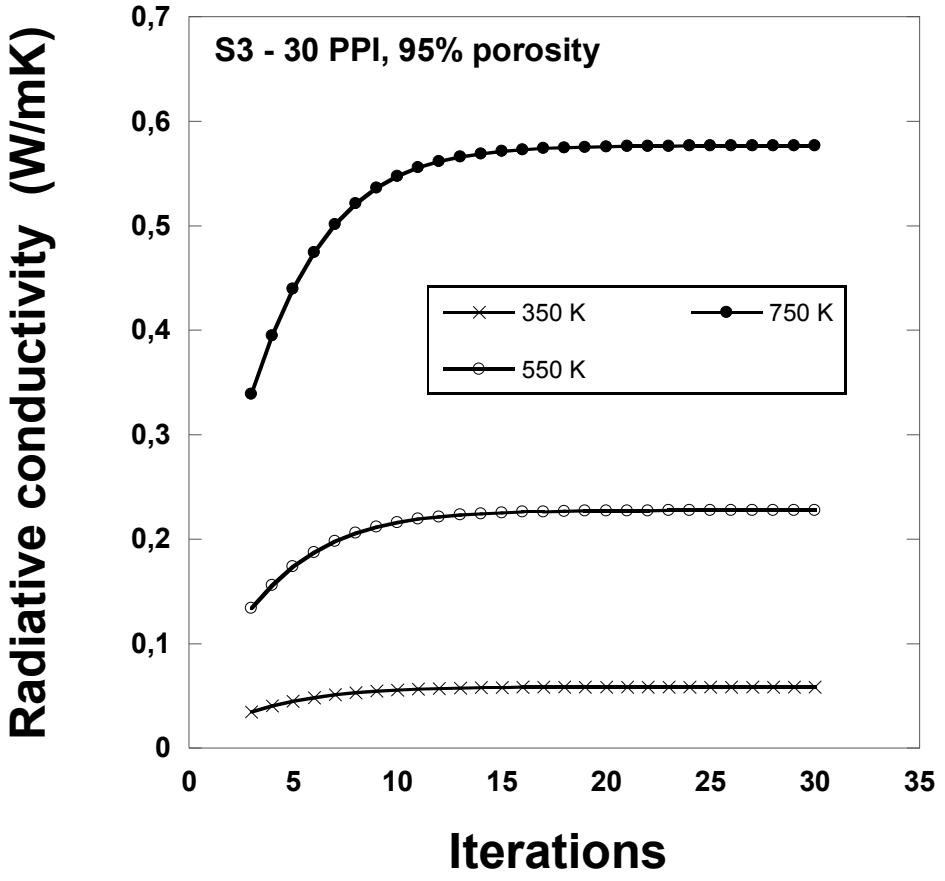

Figure 2.6. Radiative conductivity *vs* number of iterations for the sample S3.

It is worth to underline that for samples with a thickness less than twice the minimum order of stabilization, i.e. less than about $30 \bullet d_c$, the model presented in this paper predicts a radiative conductivity that depends on the sample thickness. This was already pointed out in [110 – 112] and it plays a significant role when radiative conductivity is to be measured.

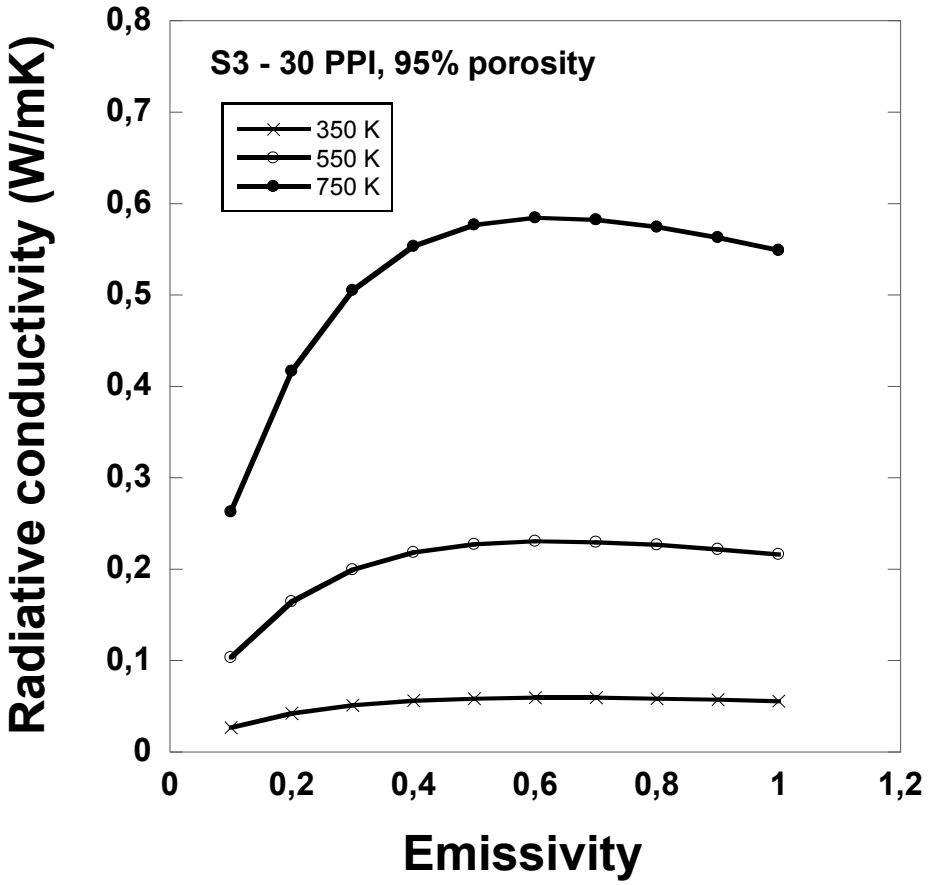

Figure 2.7. Radiative conductivity *vs* emissivity for the sample S3.

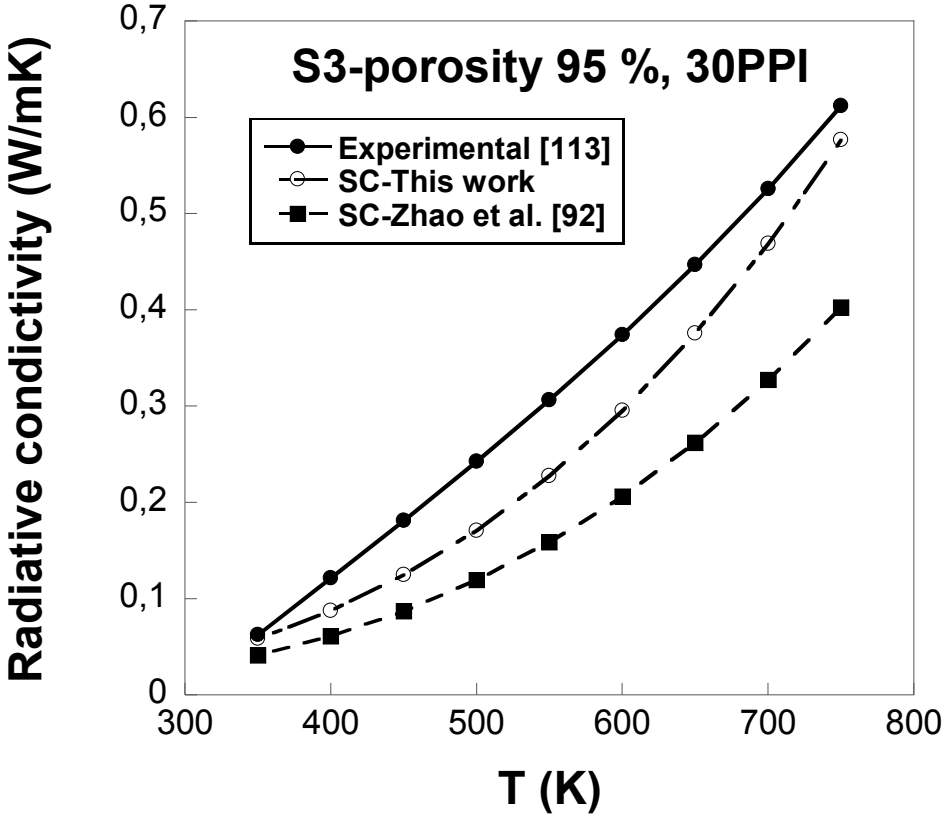

Figure 2.8. Radiative conductivity *vs* temperature for the sample S3.

More, it is worthwhile to remark that if the sample cannot be considered optically thick, that is its thickness is below the 30•d_c threshold, for which the boundary conditions are eqs.2.10 and-2.11, the radiative conductivity depends also on the emissivity of the plates.

A 0.6 foam solid face emissivity has been assumed, that is the value for the FeCrAlY alloy given by [84] and used in [92]. The radiative conductivity as a function of the emissivity, at different temperatures, for the S3 sample is reported in fig.2.7. One can

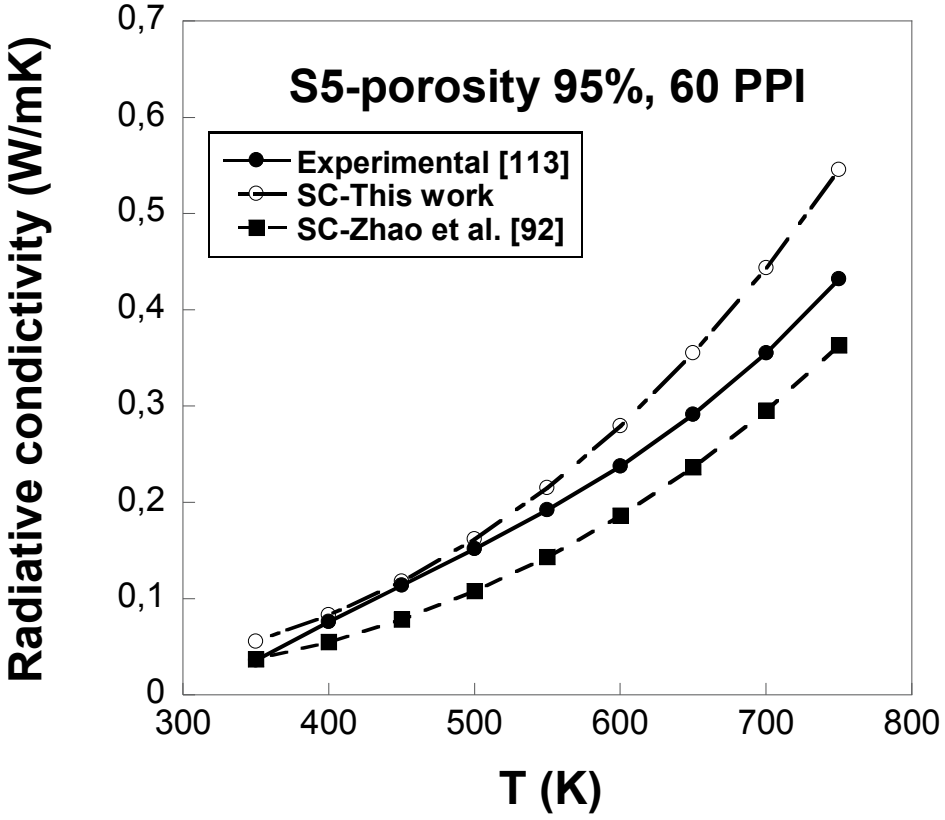

Figure 2.9. Radiative conductivity *vs* temperature for the sample S5.

notice that in the range of the investigated temperatures deviations of the emissivity from the 0.6 typical value are nearly negligible.

Finally, a grey foam solid face emissivity has been assumed.

This last assumption was also made in Zhao et al.'s paper. In particular, the authors highlighted that the relatively poor accuracy of their model results could be just due to this simplification and to the idealized geometry used (simple cubic) [92].

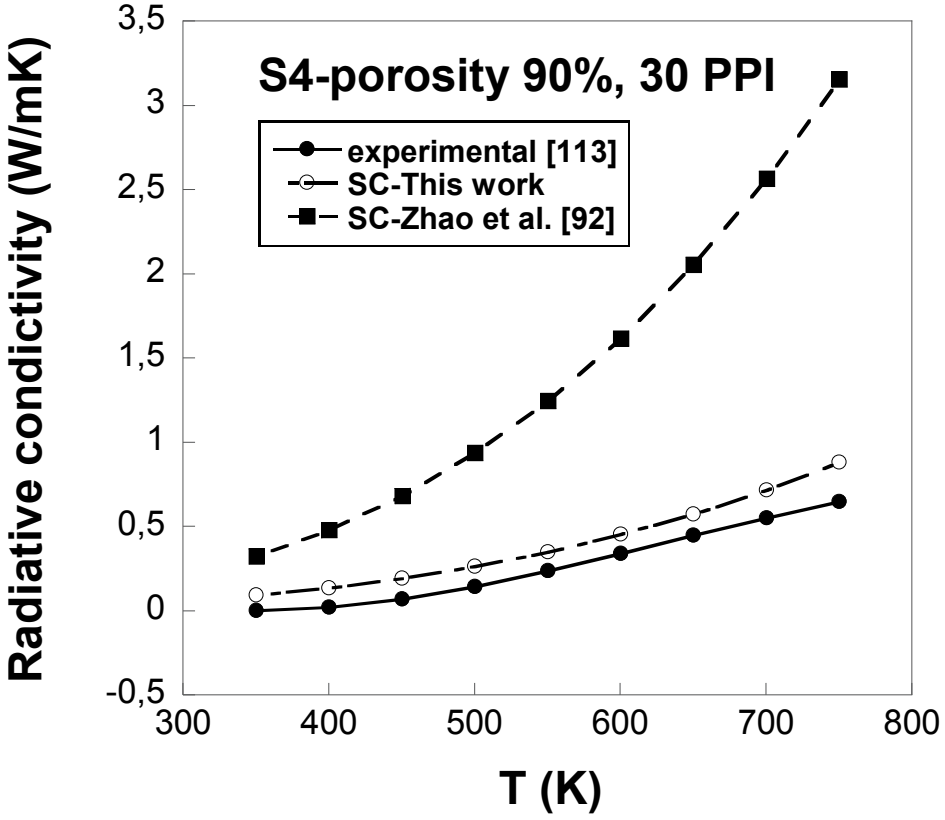

Figure 2.10. Radiative conductivity *vs* temperature for the sample S4.

The assumption of a grey emissivity is too difficult to overcome and it is convenient to maintain it.

Instead, with the aim to improve the model predictability, the geometrical representation has been made more realistic in this work, by modifying the

coefficients and by adopting a Monte Carlo numerical procedure for the evaluation of the configuration factors [83, 84, 121].

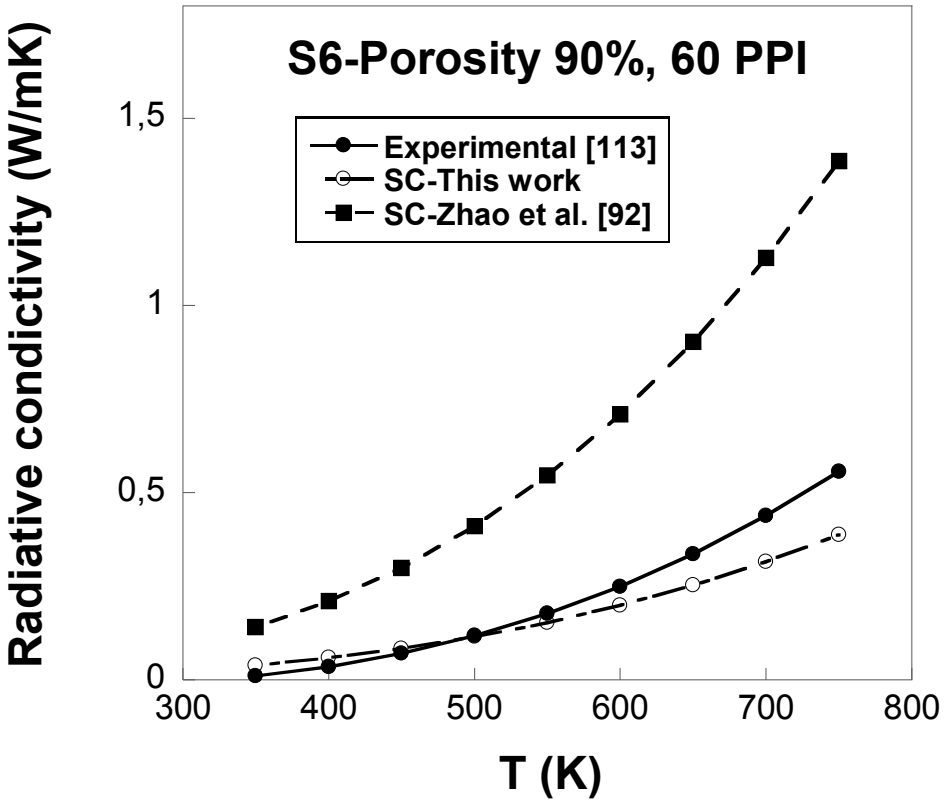

Figure 2.11. Radiative conductivity *vs* temperature for the sample S6.

Figures 2.8 and 2.9 show that for a 95% foam porosity, both the values predicted by the present and the Zhao et al's models agree well with the experimental data. It is worth noticing that the proposed model works better than the model proposed by Zhao et al. [92].

Figures 2.10 and 2.11, for a 90% foam porosity, point out large differences between the values of radiative conductivity predicted by the Zhao's model and the

experimental ones, whereas a good agreement can be observed between experimental data and predictions by the model presented in this section.

Figures 2.10 and 2.11, for a 90% foam porosity, point out large differences between the values of radiative conductivity predicted by Zhao et al. [113] and the experimental ones, whereas a good agreement can be observed between experimental data and predictions by the model presented in this work.

In all cases results show that the values of radiative conductivity predicted by the proposed model are in better agreement with the values measured at different temperatures [113] than the predictions obtained by means of the Zhao et al's model [92].

2.3 Semi-analytical modeling of the radiative heat transfer based on a Lord Kelvin idealized morphology [2] of the open-cell foams

2.3.1 Introduction

A radiative heat transfer model based on the tetrakaidecahedric (TD) representation of the foam cells proposed by Lord Kelvin has been developed in this section with the aim to overcome one of the simplification of the original analysis (see section 2.2.6).

The analytical approach has been combined with numerical simulations based onto ray-tracing Monte Carlo method [83, 84, 121] and with a matrix algebra implemented procedure, used to consistently calculate the involved view factors. The radiative conductivity of foams has been evaluated by means of the proposed model. Predictions are compared both with experimental results from the literature, obtained on several metallic foams, and with predictions given by the simplified model

proposed by Zhao et al. [92] based on a cubic representation of the foam unit cell and described in previous section. Concerning to the ability to predict the experimental results, the TD model described in this section works better than both, the simplified cubic model proposed in section 2.2 and the model [92].

In the present study, however, with reference to metal open cell foams, the theoretical approach developed in the section 2.2 has again been used to further refine the model and to obtain a model based on a more realistic representation of the foam cells. The radiative conductivity of foams has been evaluated by means of the proposed model.

2.3.2 The assumptions of the model

It is worth reminding that both ceramic and metallic open-cells foams can be considered as a net of interconnected solid rods whose transverse section has a form that can be circular, triangular, triangular with concave sides. The body of the rods (struts) can be either empty or full. The dimensions of the struts are variable along their length and lumps of material are often present at the intersections of the ideal geometry that represents the cell. It has a tetrakaidecahedron (TD) shape with the characteristic size d_p, as shown in fig.2.12. The cells are randomly oriented and mostly homogeneous in size and shape. Finally, external solid surfaces have often a remarkable roughness that sometimes concurs to make difficult the geometrical characterization.

In order to simplify the modeling of heat transfer in this complex geometry, reference has been made to an open cell foam sample made up of uniformly distributed, equal-sized cells, sandwiched between two cylindrical plates. The sandwich thickness is s. The sample configuration is sketched in fig.2.13. The TD geometry proposed by Lord Kelvin, formed by 6 square and 8 hexagonal faces, was chosen as the basic cell of the model.

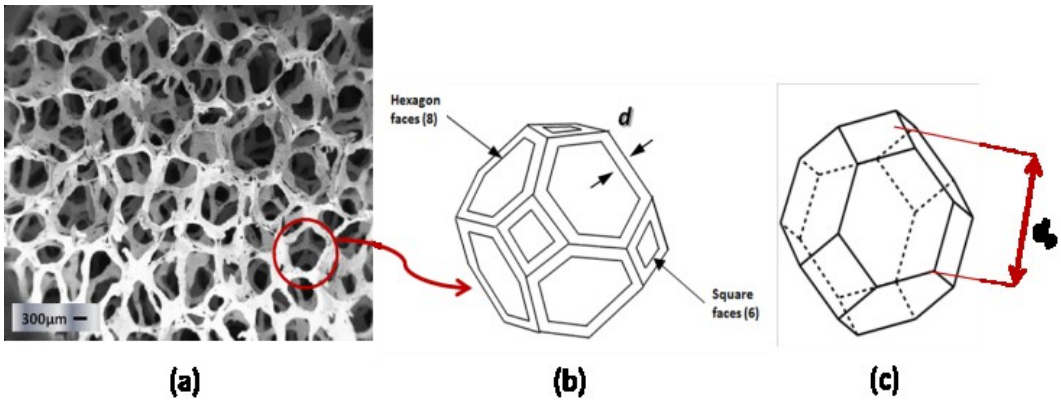

Figure 2.12. Sketch of a typical open cell metal foam: a) SEM morphology; b) foam cell with triangular strut; c) TD geometry.

As already shown in section 1.2 the porous medium is characterized by the porosity φ, and by the pore density, that is referred to in Pores Per Inch, PPI, units. In the following reference will be made to porosities up to about 0.90 and, therefore, a circular cross section of the metal struts will be assumed according to conclusions of chapter 1 and similarly to what is reported in ref. [123].

The correlation between the total porosity, φ_t, and the relative density, ρ_r, is

$$\rho_r = \frac{V_s}{V_o} = \frac{V_o - V_I}{V_o} \equiv 1 - \varphi_t \tag{1.4}$$

where

$$\varphi_t \equiv \frac{V_I}{V_o} \tag{1.5}$$

and V_s is the volume of the solid strut, V_I is the volume of the total inner void spaces (inclusive of the hollow spaces into strut body, if any) and V_o is the outer volume of the entire sample. As remarked in section 1.2, in fact, very often the struts of real foams are hollow and, therefore, both the really accessible surface for fluids and the radiating, reflecting and absorbing surfaces involved in the radiation heat exchange

Table 2.2. Characteristics of foams [31]

Quantity	**Sample**			
	S-3	**S-4**	**S-5**	**S-6**
Pores Per Inch (1/inch*)*	30	30	60	60
Nominal relative density (%)	5	10	5	10
Measured relative density (%)	4.1	9.3	5.5	9.2
Nominal cell size (mm)	0.847	0.847	0.423	0.423
Measured cell size (mm)	1.999	2.089	0.975	0.959
Struts diameter (mm)	0.215	0.267	0.124	0.154
Effective porosity (%)	0.917	0.879	0.898	0.852

are the outer surfaces of the struts. As a consequence it is useful to introduce an effective porosity, φ, as that which involves only the inner part of each open cell but without considering the not accessible inner surface of the struts, if any. When the struts are hollow a fictitious density, $\rho^* = V_{strut}/V_o = 1 - \varphi$ is defined. . To validate the thermal model of this paragraph this aspect, together with the already mentioned

more realistic unitary cell is considered. As consequence it is introduced the so named outer or effective porosity φ as that which involves only the inner part of each open cell but without considering the not accessible inner volume of the struts if there is. If the strut are hollow a fictitious density $\rho^*=V_{strut}/V_o=1-\varphi$ must be introduced. To test the thermal model of this paragraph this aspect, together with the

already mentioned more realistic unitary cell is considered. According to Fuller et al. [31], the values of porosities have been corrected in the following way

$$\varphi = 1 - \rho_r \left(\frac{1}{1 - (d_i/d)^2} \right) \tag{2.45}$$

where d_i is the diameter of the internal hollow as estimated by SEM measurements and d is the external diameter of the cylindrical strut.

The samples used for the comparison are again those in [113] S-3, S-4, S-5 and S-6, whose morphological parameters are those listed in Table 2.2.

2.3.3 Analysis of the heat transfer

Reference is made to the configuration reported in fig.2.4. Both plates are thin enough as to allow to assume the top and the bottom plates to be at uniform temperatures, T_c and T_h, respectively. We also assume that T_h is higher than T_c and that the sandwich structure is under vacuum and thermally insulated at other ends. The $T_h > T_c$ assumption implies a net radiation heat transfer in the positive z-direction. In a cell the top and bottom square surfaces (voids) are referred as A and E and each of the four lateral square surfaces is denoted as C. The eight hexagonal surfaces on the upper and lower halves of the cell are referred as B and D, respectively. The struts are numbered clockwise starting from the contour of surface A. For the sake of clarity of the image numbering was not shown in the figure. Under vacuum, convection does not occur and heat is transferred by conduction and radiation. Though, generally, conduction and radiation are non-linearly coupled, one can assume that in highly porous metal foams radiation is transferred mostly through voids of neighbouring cells. Therefore, conduction and radiation can be considered decoupled and temperature can be assumed to depend linearly on z [92]. Finally, the grey body assumption is made.

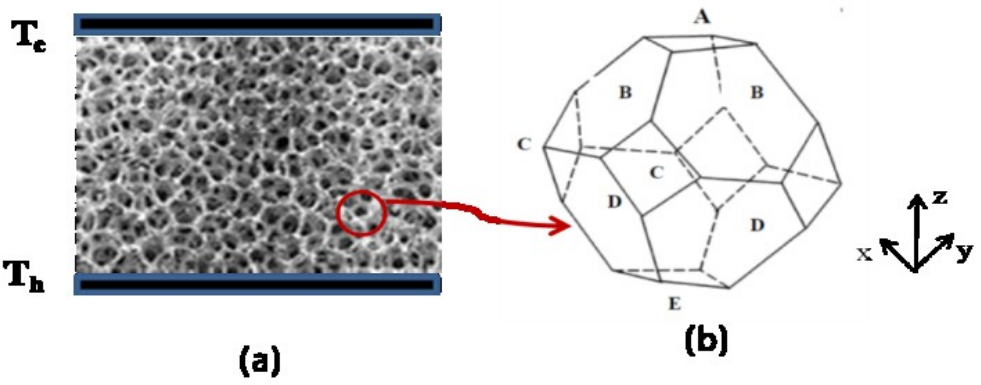

Figure 2.13. Sample configuration: a) sketch; b) Lord Kelvin geometry.

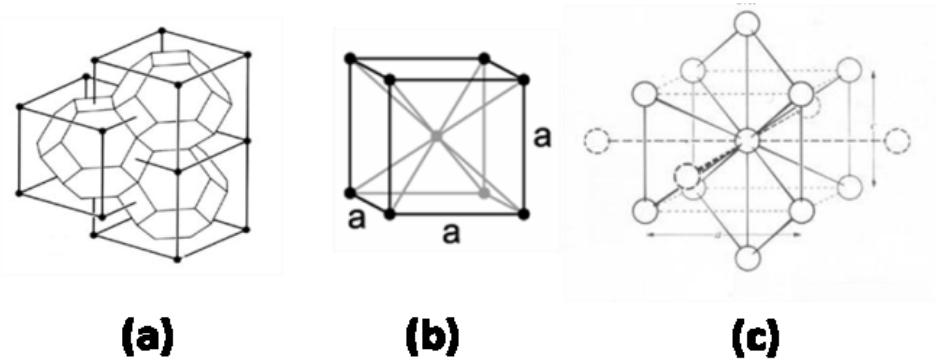

Figure 2.14. Wigner-Seitz cells: a) connected cells; b) body centered cubic lattice; c) reticular distances.

Assuming a thick enough foam sample ($s >> d_p$), variations of the temperature within the unit cell can be neglected and a uniform temperature can be assigned to each cell, that, for the sake of simplicity, can be represented as a node.

Consequently, the usual approach of crystallography is now inverted. In fact, in cristallography the tetrakaidecahedric cell associated to each node is well known as the Wigner-Seitz cell of a body centered cubic lattice (*bcc*), as reported in fig.2.14. The Wigner-Seitz cell is obtained by bisecting with planes the 14 segments that

connect each node with the 8 nearest neighbouring nodes and the 6 second neighbouring nodes. It is worth noticing that the distance between a couple of opposite square surfaces, *a*, is equal to the distance between aligned nodes of the bcc lattice (fig.2.14b). Thanks to this representation, the heat transfer between two adjacent nodes can be regarded to flow through virtual segments (continuous lines in fig.2.14c).

The difference between the temperatures of nodes belonging to two adjacent planes containing vertically aligned nodes is

$$\Delta T = \frac{T_h - T_c}{N_p - 1} \tag{2.46}$$

Thus, heat is transferred in the *z* direction and along the diagonal under temperature differences equal to ΔT and $\Delta T/2$, respectively, whereas no heat is transferred in the x and *y* directions, along which the temperature gradient is zero.

The radiative conductivity, k_r, can be evaluated by the following equation

$$k_r = q_r \frac{s}{(T_h - T_c)} \tag{2.47}$$

once the heat flux, q_r, is evaluated.

In the following, calculations will be carried out with reference to the $2N_p$ - 1 planes that contain faces of the bcc lattice parallel to the *xy* plane. Once the center-plane between planes in contact with plates at T_h ($z = 0$) and T_c ($z = s$) is assumed as the 0 plane, planes will be numbered from – (N_p -1) at $z = 0$ to + (N_p – 1) at $z = s$.

With reference to fig.2.15 and to the area of the square surface in the *xy* plane, A_{bcc}, whose center is the node *n1* in the reference plane 0 and whose side is *a*, the heat flux can be calculated as the sum of the difference between the radiosities of the top void,

JA (fig.2.13b), in the opposite directions, and the differences between the radiosities of the four voids, *JB,* (fig.2.13b), in the opposite directions

$$q_r = \frac{A_A\,(JA_+^{(0)} - JA_-^{(-2)}) + 4\,A_B\,(JB_+^{(0)} - JB_-^{(-1)})}{A_{bcc}} \qquad (2.48)$$

where superscripts refer to the planes where nodes exchanging heat with node *n1* are located. The plane # -1 (fig.2.15) contains nodes *n3*, *n4*, *n5*, *n6*, exchanging heat with the node *n1* in the diagonal direction while the node *n2* exchanging heat with *n1* in the *z* direction is contained in the plane # - 2. Plus and minus subscripts denote the direction of the heat flux: plus for irradiation in the positive *z* direction and minus for the irradiation in the opposite direction.

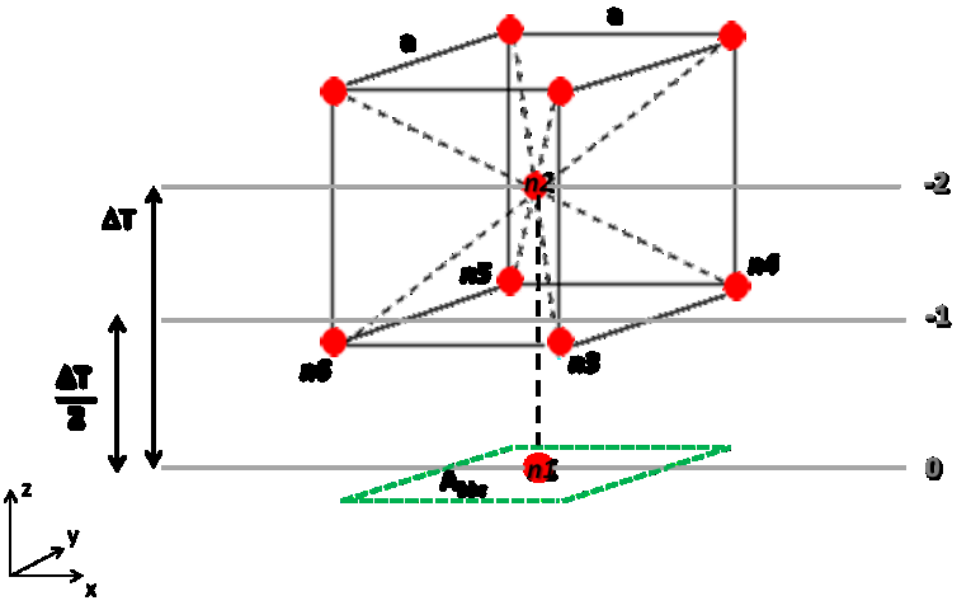

Figure 2.15**.** Scheme for the heat flux calculation.

In order to compute the radiosities $JB_{\pm}^{(0)}$, $JB_{\pm}^{(-1)}$, $JA_{\pm}^{(0)}$, $JA_{\pm}^{(-2)}$ an iterative procedure has been implemented, that takes into account the irradiation from all the other planes, step by step, up to the farthest ones, in direct contact with the external plates at temperatures T_h and T_c. As far as the radiosities are concerned, in particular, the contribution from all the voids and the struts of the cells has to be taken into account.

In eqs.2.49 and 2.50 the radiosities of the top surface, $\mathrm{JA}_{\pm}^{(\mathrm{i})}$, and of the four lateral surfaces in the upper half of the cell, $\mathrm{JB}_{\pm}^{(\mathrm{i})}$, of the i-th plane can be obtained adding up four contributions. The first is the radiation emitted from the surfaces of the struts facing the inner region of the cell. The second is due to the radiosities of the four lateral surfaces *D* in the lower half of the cell. The third is due to the radiosities of the four lateral surfaces, *C*, where the radiosity $JC_{\pm}^{(\mathrm{i})}$, as reported in eq.2.51, is the sum of the emission of the ligaments and of the radiosities of the surfaces placed on the half bottom *E* and *D*. The fourth is due to the radiosity of the bottom surface, $JE_{\pm}^{(\mathrm{i})}$.

$$JA_{\pm}^{(\mathrm{i})} = \alpha_1\,\varepsilon\,\sigma\,(T(0) \pm i\,\Delta T/2)^4 + \alpha_2\,JD_{\pm}^{(\mathrm{i})} + \alpha_3\,JC_{\pm}^{(\mathrm{i})} + \alpha_4\,JE_{\pm}^{(\mathrm{i})} \tag{2.49}$$

$$JB_{\pm}^{(\mathrm{i})} = \beta_1\,\varepsilon\,\sigma\left(T(0) \pm i \bullet \frac{\Delta T}{2}\right)^4 + \beta_2\,JD_{\pm}^{(\mathrm{i})} + \beta_3\,JC_{\pm}^{(\mathrm{i})} + \beta_4\,JE_{\pm}^{(\mathrm{i})} \tag{2.50}$$

$$JC_{\pm}^{(\mathrm{i})} = \gamma_1\,\varepsilon\,\sigma(T(0) \pm i \bullet \Delta T/2)^4 + \gamma_2\,JD_{\pm}^{(\mathrm{i})} + \gamma_3\,JC_{\pm}^{(\mathrm{i})} + \gamma_4\,JE_{\pm}^{(\mathrm{i})} \tag{2.51}$$

Coefficients α_1, β_1, γ_1 weigh the contribution of the radiative emission of the struts at the temperature of a cell, *T(i)*, to the radiosity of the void *A*, all the voids *B*, all the voids *C*, respectively. Coefficients α_2, β_2, γ_2 weigh the contribution of the *D* void radiosity to the radiosity of the voids *A*, *B*, *C*, respectively. Coefficients α_3, β_3, γ_3 weigh the contribution of the *C* void radiosity to the radiosity of the voids *A*, *B* and *C*, respectively. Coefficients α_4, β_4, γ_4 weigh the contribution of the *E* void radiosity to the radiosity of the voids *A*, *B*, *C*, respectively.

Coefficients α_i, β_i, γ_i, are expounded in the next section and in the Appendix A.

Observing fig.2.14a one can easily derive also the following correlations

$$JD_{\pm}^{(\mathrm{i})} = JB_{\pm}^{(\mathrm{i}-1)} \tag{2.52}$$

$$JE_{\pm}^{(\mathrm{i})} = JA_{\pm}^{(\mathrm{i}-2)} \tag{2.53}$$

Boundary conditions are

$$JE_{+}^{(\mathrm{Np}-1)} = \varepsilon\, \sigma\, T_h^4 \tag{2.54}$$

$$JE_{-}^{-(\mathrm{Np}-1)} = \varepsilon\, \sigma\, T_c^4 \tag{2.55}$$

$$JD_{+}^{(\mathrm{Np}-1)} = \varepsilon\, \sigma\, T_h^4 \tag{2.56}$$

$$JD_{-}^{-(\mathrm{Np}-1)} = \varepsilon\, \sigma\, T_c^4 \tag{2.57}$$

2.3.4 Coefficients and view factors

Coefficients α_i, β_i, γ_i, depend on the ratio of the surface area of the void or the strut where radiation is coming from to the area of surfaces *A*, *B*, *C* and can be calculated

considering the view factors and the areas of the voids and struts involved in each case. The expressions of coefficients α_i, β_i, γ_i, as it will be expounded in the Appendix A, are the following

$$\alpha_1 = \frac{A_s\, Tr(\boldsymbol{sA})}{A_E} + \frac{35\, A_s\, \rho\, F_{st,av}\, Tr(\boldsymbol{sA})}{A_E} \tag{2.58}$$

$$\alpha_2 = 4\, F_{DA} + \rho\, \frac{A_s}{A_E} Tr(\boldsymbol{DA}) \tag{2.59}$$

$$\alpha_3 = 4\, F_{CA}\, \frac{A_D}{A_E} + \rho\, \frac{A_s}{A_E}\, Tr(\boldsymbol{CA}) \tag{2.60}$$

$$\alpha_4 = F_{EA} + \rho\, \frac{A_s}{A_E}\, Tr(\mathbf{EA}) \tag{2.61}$$

$$\beta_1 = \frac{A_s\, Tr(\boldsymbol{sB})}{A_D} + \frac{35\, \rho\, A_s\, F_{st,av}\, Tr(\boldsymbol{sB})}{A_D} \tag{2.62}$$

$$\beta_2 = 4\, F_{DB}\, \frac{A_E}{A_D} + \rho\, \frac{A_s\, Tr(\boldsymbol{DB})}{A_D} \tag{2.63}$$

$$\beta_3 = 4\, F_{CB} + \rho\, \frac{A_s\, Tr(\boldsymbol{CB})}{A_D} \tag{2.64}$$

$$\beta_4 = F_{EB}\, \frac{A_E}{A_D} + \rho\, \frac{A_s\, Tr(\boldsymbol{EB})}{A_D} \tag{2.65}$$

$$\gamma_1 = \frac{A_s\, Tr(\boldsymbol{sC})}{A_C} + \frac{35\, \rho\, F_{s-t,av}\, A_s\, Tr(\boldsymbol{sC})}{A_C} \tag{2.66}$$

$$\gamma_2 = 4\, F_{DC}\, \frac{A_D}{A_C} + \frac{\rho\, A_s\, Tr(\boldsymbol{DC})}{A_C} \tag{2.67}$$

$$\gamma_3 = 3\, F_{CB}\, \frac{A_c}{A_E} + \frac{\rho\, A_s\, Tr(\boldsymbol{CC})}{A_E} \tag{2.68}$$

$$\gamma_4 = F_{EC}\, \frac{A_E}{A_C} + \frac{\rho\, A_s\, Tr(\boldsymbol{EC})}{A_C} \tag{2.69}$$

In eqs. 2.58 – 2.69 the first term accounts for the direct irradiation on a surface and the second term takes into account the irradiation on a surface after the first reflection occurred. Since in the following reference is be made to foams with porosity in the 0.85 – 0.94 range and a 0.6 reflectivity, larger than the first order reflections by the struts can be neglected. In cylindrical struts, the area of their lateral surface, facing the inner region of the cell, has the following expression, common to all 36 struts of the cell,

$$A_s = \frac{\pi}{3}\, l_s\, d \tag{2.70}$$

The areas of the square void surfaces *A*, *C*, *E* and those of the hexagonal void surfaces *B*, *D* are, respectively,

$$A_A = A_C = A_E = l^2 \tag{2.71}$$

$$A_B = A_D = \frac{3\sqrt{3}}{2}\, l^2 \tag{2.72}$$

where *l* is the length of the side of the square void, that is a function of the cell size d_p for the TD.

Tr are the traces of the matrixes presented in the Appendix A, as a function of view factors.

$\rho = 1 - \varepsilon$ is the reflectivity of the strut which is assumed completely diffuse because the scale of the surface irregularities considered is supposed greater than the wavelengths.

F_{CA}, F_{DA}, F_{EA}, F_{CB}, F_{DB}, F_{EB}, F_{DC} are the void-void view factors; $F_{st,\,av}$ is the average value of the strut-strut view factors $F_{s\text{-}t}$. Two approaches have been followed to calculate the view factors. The former numerical approach makes use of ray-tracing simulations based on Monte Carlo method. As already highlighted this is a numerical standard procedure [83,84,121] and for the scope the commercial software *TracePro* [122] was used as ray-tracer. The latter employs an appropriate geometrical approximation of the voids in the TD.

Before presenting the above said geometrical approximation, it is worthwhile reminding that, with reference to the surface of a sphere, the view factor between either a finite (area *S*) or infinitesimal (area d*S*) irradiating portion of the sphere and an infinitesimal (area d*A*) irradiated portion of it, $F_{S(dS)dA}$, is given by

$$F_{S(dS)dA} = \frac{dA}{4\,\pi\,r^2} \tag{2.73}$$

where *r* is the radius of the sphere. Similarly, the view factor between either a finite (area *S*) or infinitesimal (area d*S*) irradiating portion of the sphere and a finite (area A_{irr}) irradiated portion of it, $F_{S(dS)A_{irr}}$, can be written as

$$F_{S(dS)A_{irr}} = \frac{A_{irr}}{4\,\pi\,r^2} \tag{2.74}$$

Equations 2.73 and 2.74 show that in a sphere the view factor between two portions of its surface depends only on the area of the irradiated surface and is independent of the size of the irradiating surface and of the location of both surfaces.

If now a sphere is chosen whose diameter, d_s, is such that portions of its surface area approximate the area of the voids, eq.2.74 can be used in the evaluation of view factors between voids. In the easiest way reference is made to a sphere whose diameter is equal to the distance between two opposite square voids, d_p, and, therefore, the sphere is tangent to all the six square voids. In this case, because of a little area, for cells of sufficiently big size, they can be all well approximated by the spherical caps tangent to the square voids and having the same areas. This naturally it is not the only possible sphere which approximates well the square voids, as a consequence does not exist only one method to determine them, and the numerical values of the obtained configuration factors will be very similar each other if the spheres used to fit the square voids are all a good approximation.

Ultimately then the guide criterion for the choice of one sphere or another is only that of the usefulness. In particular, would be very useful if the sphere could be chosen, in such a manner that a simple formula analogue to eq.2.74 can be used also for all the eight hexagonal voids.

At this aim, let d_w, be the diameter of a circle having a same area as the hexagon, we can determine a sphere with a diameter d_S, such that the plane containing the hexagon cuts off a spherical cap whose circular base has the diameter d_w. Such a sphere has the following diameter (see section 1.16 and eq.1.68 too)

$$d_S = \sqrt{\frac{3\,{d_p}^2}{4} + {d_w}^2} \tag{2.75}$$

where d_p is the distance between opposite square voids of the cell and, therefore, $(\sqrt{3}/2)\,d_p$ is the distance between opposite hexagonal voids. At first, since d_s is not

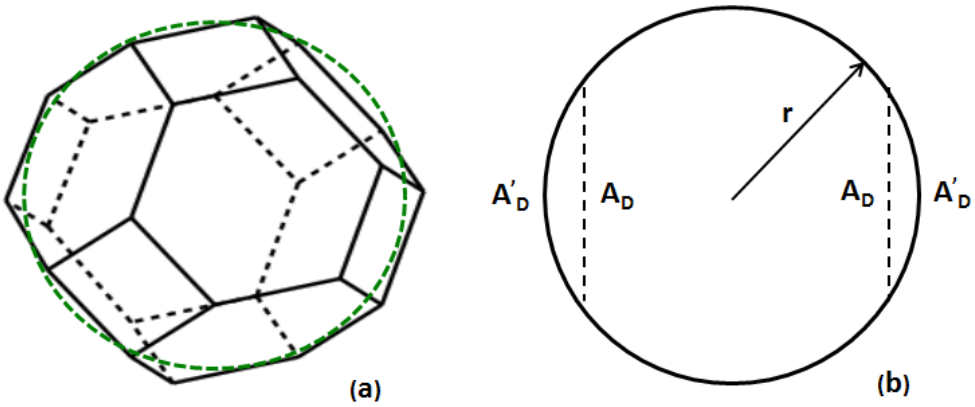

Figure 2.16. (a) Spherical approximation of the TD cell. (b) Section of the sphere: with A_D area of the facing hexagons and A'_D area of the subtended caps.

far different from d_p for typical d_w values, the sphere with the d_s diameter is not tangent to square voids but well approximates them. The above defined sphere allows a very accurate evaluation, using an equation very similar to eq.2.74, of the configuration factors involving the hexagonal voids.

As far as the view factors between two hexagonal voids are concerned, some other simple considerations must be made. Reference is made now to two spherical caps whose base are two circles of diameter d_w, i.e. circles with same area as that of a hexagonal void of the cell, A_D. Applying eq.2.74 for two, facing or not facing,spherical caps with two such subtended circles (fig.2.16b) we obtain, that for each couple of hexagons or equivalent circles

$$F_{A'_D A_D} = F_{A'_D A'_D} = \frac{A'_D}{4\,\pi\,r^2} \tag{2.76}$$

since each optical ray moving from one cap of area A'_D (or from any other surface) and intercepting another cap intercepts also the subtended circle; that is,: the cap-cap view factors are equal to circle (hexagon)-cap view factors and to cap-circle view factors. If the first and the third term in eq.2.76 are multiplied by A'_D and the view

factor reciprocity correlation is applied to the first term ($A'_D\, F_{A'_D A_D} = A_D\, F_{A_D A'_D} = A_D\, F_{A_D A_D}$), one can conclude that the following correlation holds for the view factors between each couple of hexagonal voids

$$F_{D_i B_j} = F_{B_i D_j} = \frac{A'_D}{A_D}\,\frac{A'_D}{4\,\pi\,r^2} \tag{2.77}$$

where A'_D is also equal to

$$A'_D = 2\,\pi\,r\,h \tag{2.78}$$

with *h* the height of the spherical cap and

$$h = r - \frac{\sqrt{3}}{4}\,d_p \tag{2.79}$$

Similar considerations allow to derive the correlation for view factors between an hexagonal and a square void as well as between two square voids

$$F_{AD_j} = F_{EB_j} = \frac{A'_E}{A_E}\,\frac{A'_D}{4\,\pi\,r^2} \cong \frac{A'_D}{4\,\pi\,r^2} \tag{2.80}$$

$$F_{D_j A} = F_{B_j E} = \frac{A'_D}{A_D}\,\frac{A'_E}{4\,\pi\,r^2} \tag{2.81}$$

$$F_{AE} = F_{EA} = F_{AC} = F_{EC} = \frac{A'_E}{A_E}\,\frac{A'_E}{4\,\pi\,r^2} \cong \frac{A'_E}{4\,\pi\,r^2} \tag{2.82}$$

where again for the segment of the spheres related to the hexagonal faces is used the primed symbol such as that relate to the square faces A'_E which, as already outlined, can be assumed to be equal to the area A_E of the square.

2.3.5 Validation of the model and discussion

In order to validate the model, predicted values of the radiative conductivity are compared with experimental results presented by Zhao et al. [113], in the 300 ÷ 750 K temperature range, on metal foams produced via the sintering route. Reference is made to four the samples, S-3, S-4, S-5, S-6, equal to those used by Lu et al.[30], whose characteristics are reported in Table 2.2.

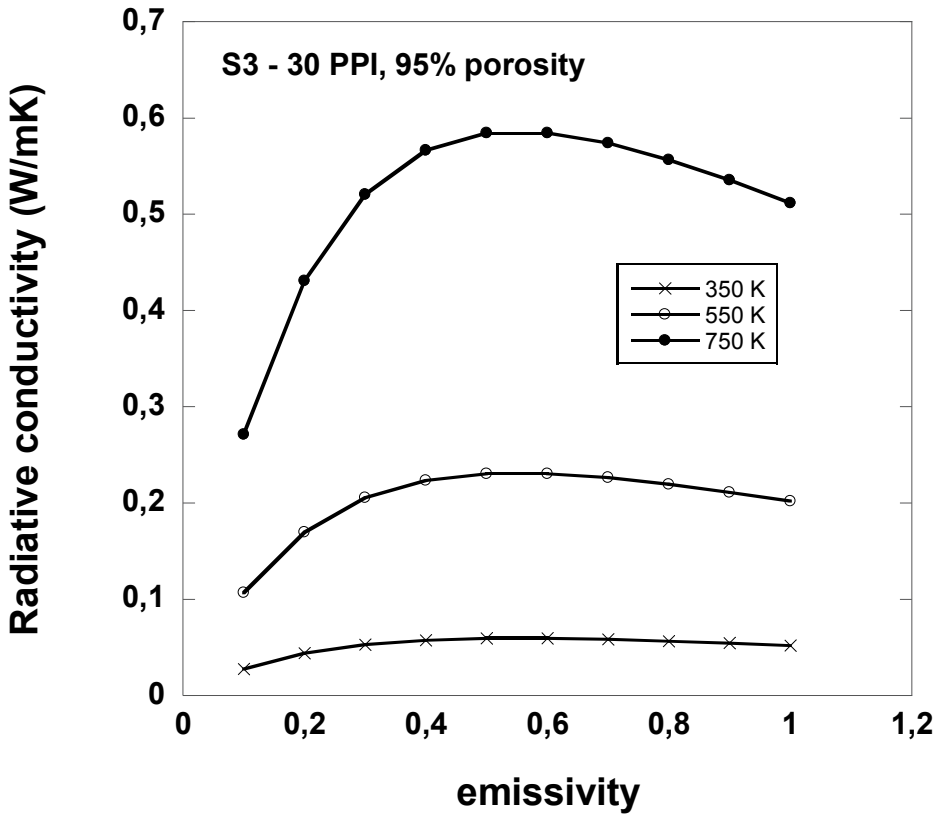

Figure 2.18. Radiative conductivity *vs* emissivity for the sample S3.

Table 2.3. Coefficients in Eq [113].

	C_0 (W/mK)	C_1 (W/mK^2)	C_2 (W/mK^3)	C_3 (W/mK^4)
S-3	- 0.4353	0.00184	- 1.7266E-6	1.5126E-9
S-4	1.3076	- 0.00859	1.6989E-5	- 8.9502E-9
S-5	- 0.5337	0.00283	- 4.6439E-6	3.4488E-9
S-6	0.05551	- 0.00051	-1.3333E-5	9.1125E-9

Experimental results have been correlated by the following third grade polynomial

$$k_r = C_0 + C_1 T + C_2 T^2 + C_3 T^3 \qquad (2.1)$$

whose coefficients are reported in Table 2.3 [113].

Radiative conductivity is evaluated with a step by step procedure by means of eqs.2.49 and 2.50.

As for the *sc* geometric representation analyzed in the previous section the evaluation of the dependence of the radiative conductivity on the order of iterations, i.e. of the number of planes of nodes involved in the calculus, showed that orders higher than about 15 must be reached to stabilize the predicted conductivity value.

The radiative conductivity as a function of the number of orders, at different temperatures, for the S3, S4, S5 and S6 samples and a 0.6 emissivity of the solid, is reported in fig.2.17. In all simulations, however, since a high enough computation speed was checked, a number of orders equal to 25 has been considered.

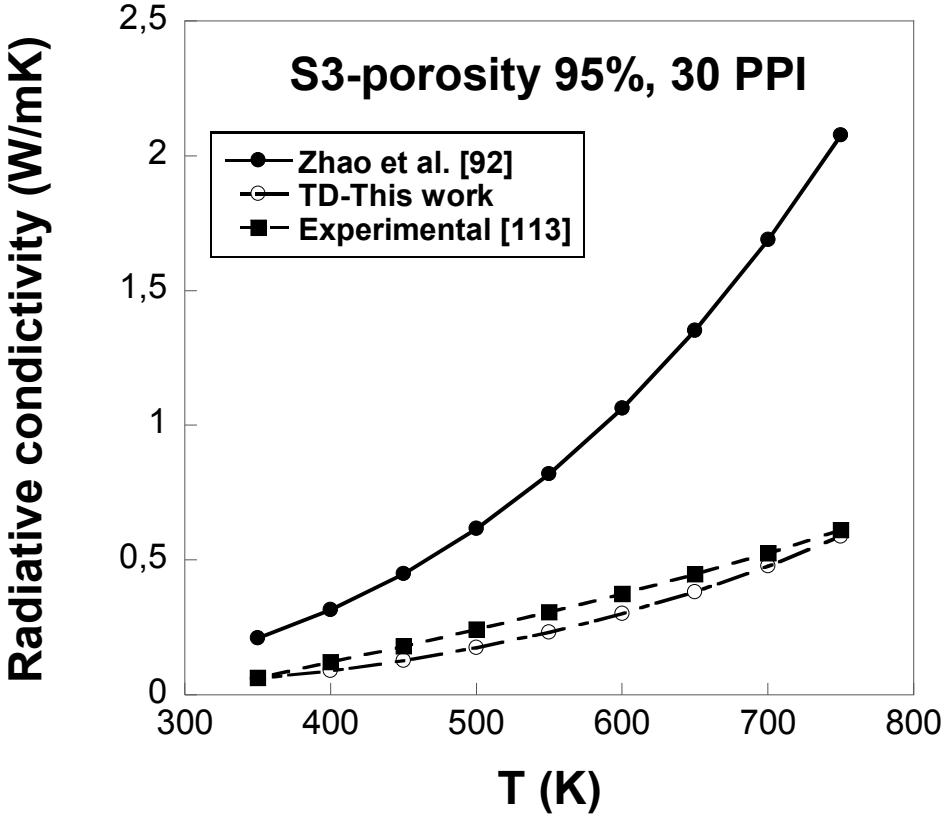

Figure 2.19. Radiative conductivity *vs* temperature for the sample S3.

Just like in the *sc* case, the thickness above which the radiative conductivity becomes independent of the sample thickness is nearly equall to $30 \cdot d_c$. In fact, eq.1.53 gives $d_c = 0.59\ d_p$ for the *sc* case and $d_c = 0.5\ d_p$ for the case of the tetrakaidecahedric cell.

Considerations similar to those made in paragraph 2.2.6 can be made with reference to the emissivity. A 0.6 foam solid face emissivity has again been assumed and the radiative conductivity as a function of the emissivity, at different temperatures, for the S3 sample is reported in fig.2.18. In this case, too, we can remark that in the

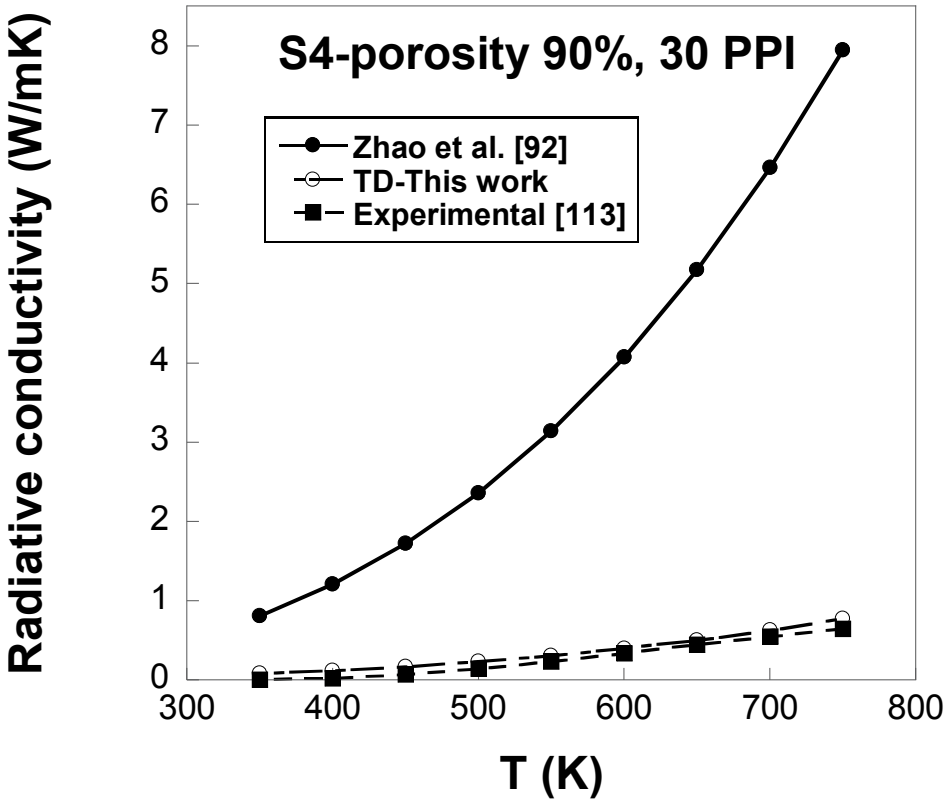

Figure 2.20. Radiative conductivity *vs* temperature for the sample S4.

range of the investigated temperatures deviations of the emissivity from the 0.6 typical value are nearly negligible. Also in this case, if the sample is sufficiently thin ($s < 15 \cdot d_p$) the boundary conditions, eqs.2.42-2.45, imply that the predicted values can depend on the emissivity of the external plates, too.

Predicted radiative conductivity for the samples S-3, S-4, S-5, S-6, in the 350 - 750 K temperature range, are compared to experimental data presented by Zhao et al. [113]

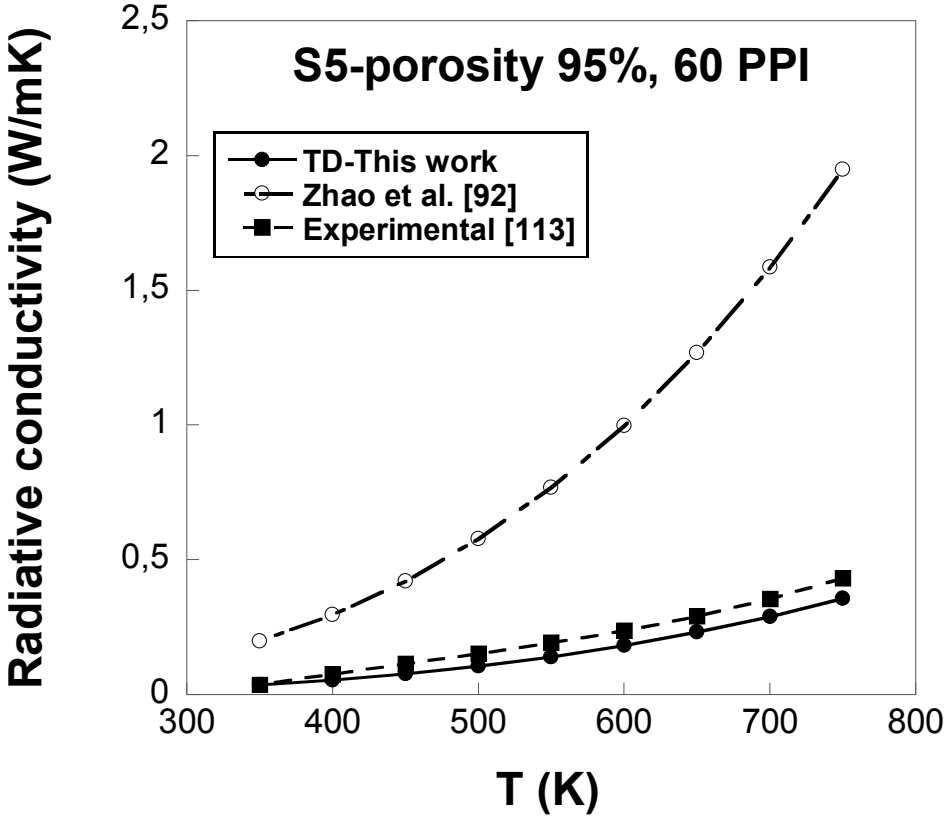

Figure 2.21. Radiative conductivity *vs* temperature for the sample S5

and to radiative conductivities obtained by means of the model presented in [92] in figs.2.19-2.22. Effective porosity values are assumed both for the TD and *sc* models.

The agreement between predictions derived by means of the proposed model and experimental results is good and far better than that between predictions by the simplified model and experimental results, particularly for the samples S-3, S-5 and S-6.

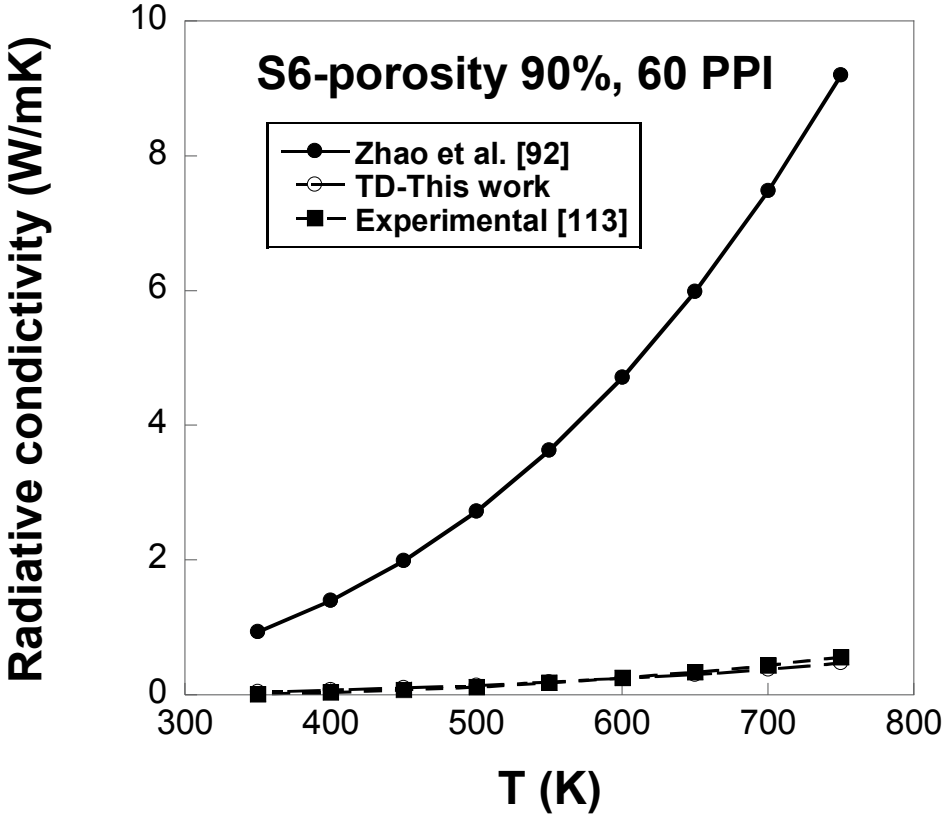

Figure 2.22. Radiative conductivity *vs* temperature for the sample S6

Radiative conductivity as a function of the temperature, for the samples S3, S4, S5, S6 and for the samples S4, S5, is presented in figs.2.23 and 2.24, respectively.

First, both figures show that the larger the pore size the higher the thermal conductivity, for a given porosity. In particular, we can notice that twice the pore size twice the radiative conductivity, that suggests a proportionality between them. This is no wonder, since, the porosity and, then, the relative density being unchanged, increasing the size of the cell, the same quantity of material can occupy the same

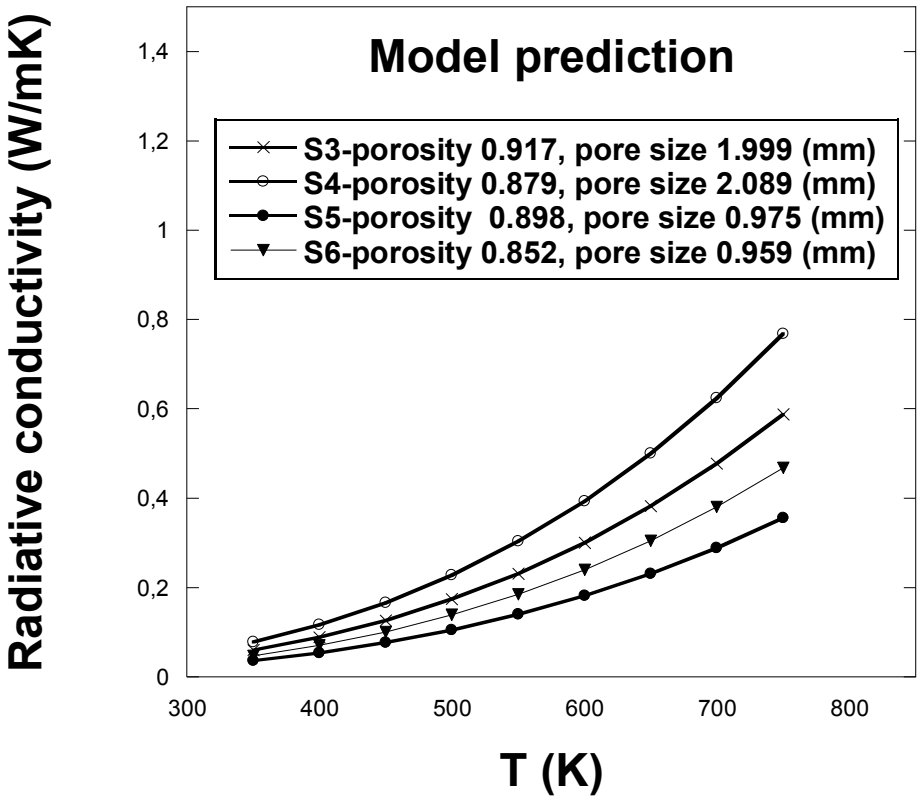

Figure 2.23. Model predicted radiative conductivities *vs* temperature for the samples S3, S4, S5 and S6

volume, with a less branched reticulated structure. Consequently, the solid-vacuum interface, where the radiation is reflected and absorbed, interrupting the heat flux exchanged between the two facing plates, increases. In other words the "penetration thickness" becomes larger and the radiative conductivity increases.

This an important remark, since Zhao et al. [92], on the contrary, concluded that a larger cell size implies a larger solid-vacuum interface, which, in turn, should result

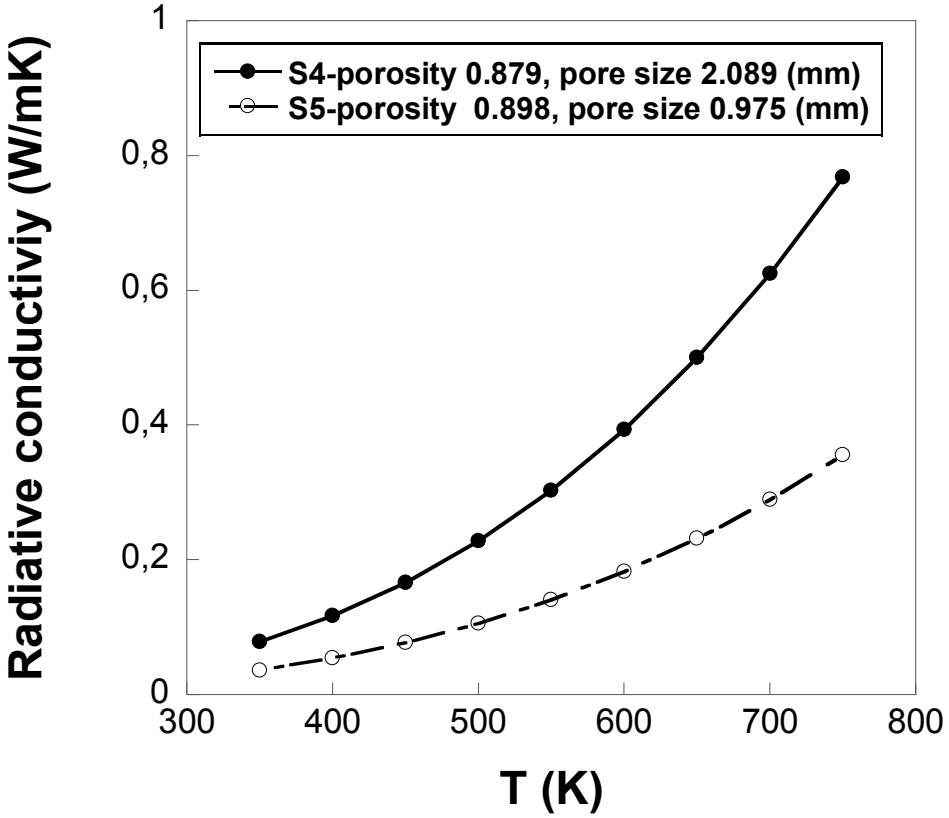

Figure 2.24. Model predicted radiative conductivities *vs* temperature for the samples S4, S5 having approximately the same porosity but pore double one of another

in a larger "penetration thickness". From two wrong implications an exact conclusion followed. In fact, a larger cell size cannot imply a larger solid-vacuum interface (i.e. a more branched reticular structure), while a larger absorption cannot imply a larger“penetration thickness", but, rather, the opposite.

Second, for an assigned pore size, the greater the porosity the lower the conductivity. This occurs, since a larger porosity implies, for a certain cell size, a smaller area of the solid-vacuum interface to the heat flux, with a decreasing diameter and an

unchanged length of the strut. An increase in the radiative conductivity occurs for the same reasons.

2.4 Conclusions

Radiation heat transfer in open cells foams was modelled by a simplified analytical-numerical method. It modified an analytical model taken from the literature. The original model involved a simplified foam discretization by a cubic representative elementary volume and allowed the evaluation of the foam radiative conductivity. The analytical-numerical approach proposed in this first phase slightly modified some coefficients of the original model. A more accurate evaluation of view factors was carried out in such cases by test ray-tracing and by numerical simulations based onto Monte Carlo method. Predictions by the original model and those by the modified proposed model were analyzed and compared to experimental results. The recalculated coefficients worked better than the original ones.

A more accurate evaluation of configurations factors between voids, by means of a numerical approach, was needed for foams with a density larger than 5%.

Results showed clearly that the radiative conductivity of the foam can markedly depend on its morphology and geometrical characteristics.

As underlined by Zhao et al. [92], the discrepancies between the values predicted by the model and experimental data have the following reasons:

1) the strong simplificative assumption of a linear temperature variation;

2) the assumed independence of the radiation properties of the wavelength;

3) the inherent uncertainty in the value of the solid emissivity;

4) the idealized structure of the foam.

The first three reasons are very difficult to tackle and to be overcome. On the contrary, there was room to build up a better idealized structure of the foam. It was

made in the subsequent part of this work. The model again involved a suitable discretization of the foam and asked for the evaluation of macroscopic parameters, such as radiosities and configuration factors but implied a more refined geometry than that of the previous model. In particular, a Lord Kelvin idealized geometry using as unit cell a TD, was employed for the discrete representation of the foams.

A more accurate evaluation of configuration factors was carried out, using both the numerical Monte Carlo method and an analytical methods with a suitable spherical approximation of the TD. The predictions of the model were again compared both with experimental data from the literature and with values predicted by a simplified model based on a simple cubic representation of the foam unit cell. The agreement between predictions by the improved model and experimental data was good and far better than that between predictions by the previous model and experimental data. One can, therefore, conclude that morphological characteristics should be adequately measured in order to model radiation heat transfer in foams since radiative models have a marked sensitivity to morphological properties of porous media**.**

Finally, the following conclusions on the essential characteristics of radiative heat transfer in foams can be made:

- the radiative conductivity of an open cell foam depends on the sample thickness when it is below a threshold limit, that is a multiple of the cell size; for the samples herein analyzed it is fifteen times the cell size;
- when the thickness is less than fifteen times the cell size, the radiative conductivity of the sample can be affected by the emissivity of the hot and cold external plates;
- when the thickness is larger than fifteen times the cell size, for which the "penetration thickness" is shorter than half the sample thickness, the radiative conductivity depends linearly on the cell size;
- the radiative conductivity of an open cell foam increases when the porosity increases.

APPENDIX A

The traces of matrixes in eqs.2.58 - 2.69, as a function of view factors, that are useful in the evaluation of coefficients α_i, β_i, γ_i in eqs.2.58 - 2.69, are expounded in the following, employing *Mathematica* software [42].

Besides of the notations for voids presented in section 2.1, the numbers of struts are now detailed and view factors are presented. Struts are numbered clockwise starting from the contour of the upper level void A; 1 – 4 at the first level; 5 – 8 at the second level; 9 – 16 at the third level; 17 – 20 at the fourth level; 21 – 28 at the fifth level; 29 – 32 at the sixth level; 33 – 36 at the seventh level.

$F_{s\Pi}$ is the view factor between the s-th strut (s = 1 - 36) and the void Π (A, B_i, C_i, D_i, E); $F_{\Pi\text{-}\Omega}$ is the view factor between a void Π and another void Ω; F_{st} is the view factor between a strut s and another strut t; $F_{st,\,av}$ is the average strut-strut view factor. Now we must take into account that there are one void A, four voids B, four voids C, four voids D, one void E. Voids B, C, D will be numbered in the following way: B_i, C_i, D_i; however, for the sake of brevity, subscripts will be omitted when unnecessary.

Let now introduce three 7x8 matrixes, denoted as $\boldsymbol{F_{s\text{-}A}}$, $\boldsymbol{F_{s\text{-}B}}$, $\boldsymbol{F_{s\text{-}C}}$, that contain the view factors between struts and voids A, B, C, respectively, are presented in eqs. A.1 – A.3. Rows refer to struts level from 1 to 7 and columns refer to the maximum number of struts in a level, i.e. 8 struts at level 3 and 5.Zero elements have been inserted in the rows that refer to levels 1, 2, 4, 6, 7, containing four struts. All the rotational symmetry properties of TD have been used in the matrixes, where only one value of common view factors is reported.

In a similar way three 7x8 matrixes, denoted as $\boldsymbol{F_{C\text{-}s}}$, $\boldsymbol{F_{B\text{-}s}}$, $\boldsymbol{F_{E\text{-}s}}$, are introduced, whose elements are the view factors between voids C, D, E and struts, respectively, in eqs. A.4 – A.6

$$\boldsymbol{F_{s-A} = F_{s-E}}$$

$$= \begin{pmatrix} F_{1A} & F_{1A} & F_{1A} & F_{1A} & 0 & 0 & 0 & 0 \\ F_{5A} & F_{5A} & F_{5A} & F_{5A} & 0 & 0 & 0 & 0 \\ F_{9A} & F_{9A} & F_{9A} & F_{9A} & F_{9A} & F_{9A} & F_{9A} & F_{9A} \\ F_{17A} & F_{17A} & F_{17A} & F_{17A} & 0 & 0 & 0 & 0 \\ F_{21A} & F_{21A} & F_{21A} & F_{21A} & F_{21A} & F_{21A} & F_{21A} & F_{21A} \\ F_{29A} & F_{29A} & F_{29A} & F_{29A} & 0 & 0 & 0 & 0 \\ F_{33A} & F_{33A} & F_{33A} & F_{33A} & 0 & 0 & 0 & 0 \end{pmatrix} \quad \text{(A.1)}$$

$$\boldsymbol{F_{s-B} = F_{s-D}}$$

$$= \begin{pmatrix} F_{1B} & F_{2B} & F_{3B} & F_{2B} & 0 & 0 & 0 & 0 \\ F_{1B} & F_{1B} & F_{7B} & F_{7B} & 0 & 0 & 0 & 0 \\ F_{1B} & F_{1B} & F_{11B} & F_{12B} & F_{13B} & F_{13B} & F_{12B} & F_{11B} \\ F_{1B} & F_{34B} & F_{35B} & F_{34B} & 0 & 0 & 0 & 0 \\ F_{17B} & F_{18B} & F_{19B} & F_{20B} & F_{20B} & F_{19B} & F_{18B} & F_{17B} \\ F_{25B} & F_{25B} & F_{27B} & F_{27B} & 0 & 0 & 0 & 0 \\ F_{29} & F_{30B} & F_{31B} & F_{30B} & 0 & 0 & 0 & 0 \end{pmatrix} \quad \text{(A.2)}$$

$$\boldsymbol{F_{s-C}}$$

$$= \begin{pmatrix} F_{1C} & F_{2C} & F_{2C} & F_{1C} & 0 & 0 & 0 & 0 \\ F_{5C} & F_{6C} & F_{7C} & F_{6C} & 0 & 0 & 0 & 0 \\ F_{9C} & F_{10C} & F_{11C} & F_{12C} & F_{12C} & F_{11C} & F_{10C} & F_{9C} \\ F_{33C} & F_{34C} & F_{34C} & F_{33C} & 0 & 0 & 0 & 0 \\ F_{9C} & F_{10C} & F_{11C} & F_{12C} & F_{12C} & F_{11C} & F_{10C} & F_{9C} \\ F_{5C} & F_{6C} & F_{7C} & F_{6C} & 0 & 0 & 0 & 0 \\ F_{1C} & F_{2C} & F_{2C} & F_{1C} & 0 & 0 & 0 & 0 \end{pmatrix} \quad \text{(A.3)}$$

$$\boldsymbol{F_{C-s}} = \begin{pmatrix} F_{C1} & F_{C1} & F_{C1} & F_{C1} & F_{C1} & F_{C1} & F_{C1} & F_{C1} \\ F_{C5} & F_{C5} & F_{C5} & F_{C5} & F_{C5} & F_{C5} & F_{C5} & F_{C5} \\ F_{C9} & F_{C9} & F_{C9} & F_{C9} & F_{C9} & F_{C9} & F_{C9} & F_{C9} \\ F_{C17} & F_{C17} & F_{C17} & F_{C17} & F_{C17} & F_{C17} & F_{C17} & F_{C17} \\ F_{C25} & F_{C25} & F_{C25} & F_{C25} & F_{C25} & F_{C25} & F_{C25} & F_{C25} \\ F_{C29} & F_{C29} & F_{C29} & F_{C29} & F_{C29} & F_{C29} & F_{C29} & F_{C29} \\ F_{C33} & F_{C33} & F_{C33} & F_{C33} & F_{C33} & F_{C33} & F_{C33} & F_{C33} \end{pmatrix} \quad \text{(A.4)}$$

$$\boldsymbol{F_{B-s}} = \boldsymbol{F_{D-s}} = \begin{pmatrix} F_{D1} & F_{D1} & F_{D1} & F_{D1} & F_{D1} & F_{D1} & F_{D1} & F_{D1} \\ F_{D5} & F_{D5} & F_{D5} & F_{D5} & F_{D5} & F_{D5} & F_{D5} & F_{D5} \\ F_{D9} & F_{D9} & F_{D9} & F_{D9} & F_{D9} & F_{D9} & F_{D9} & F_{D9} \\ F_{D17} & F_{D17} & F_{D17} & F_{D17} & F_{D17} & F_{D17} & F_{D17} & F_{D17} \\ F_{D25} & F_{D25} & F_{D25} & F_{D25} & F_{D25} & F_{D25} & F_{D25} & F_{D25} \\ F_{D29} & F_{D29} & F_{D29} & F_{D29} & F_{D29} & F_{D29} & F_{D29} & F_{D29} \\ F_{D33} & F_{D33} & F_{D33} & F_{D33} & F_{D33} & F_{D33} & F_{D33} & F_{D33} \end{pmatrix} \quad \text{(A.5)}$$

$$\boldsymbol{F_{A-s}} = \boldsymbol{F_{E-s}} = \begin{pmatrix} F_{E1} & F_{E1} & F_{E1} & F_{E1} & F_{E1} & F_{E1} & F_{E1} & F_{E1} \\ F_{E5} & F_{E5} & F_{E5} & F_{E5} & F_{E5} & F_{E5} & F_{E5} & F_{E5} \\ F_{E9} & F_{E9} & F_{E9} & F_{E9} & F_{E9} & F_{E9} & F_{E9} & F_{E9} \\ F_{E17} & F_{E17} & F_{E17} & F_{E17} & F_{E17} & F_{E17} & F_{E17} & F_{E17} \\ F_{E25} & F_{E25} & F_{E25} & F_{E25} & F_{E25} & F_{E25} & F_{E25} & F_{E25} \\ F_{E29} & F_{E29} & F_{E29} & F_{E29} & F_{E29} & F_{E29} & F_{E29} & F_{E29} \\ F_{E33} & F_{E33} & F_{E33} & F_{E33} & F_{E33} & F_{E33} & F_{E33} & F_{E33} \end{pmatrix} \quad \text{(A.6)}$$

where

$$F_{Cs} = F_{C_1 s} + F_{C_2 s} + F_{C_3 s} + F_{C_4 s}$$

$$F_{Ds} = F_{D_1 s} + F_{D_2 s} + F_{D_3 s} + F_{D_4 s} \qquad \text{(A.7)}$$

and, thanks to the symmetry of the cell, in each row of the matrixes the view factors have a common value.

The above presented six matrixes allow the evaluation of some coefficients in eqs.2.49 - 2.51. In fact, with reference to an irradiating void Π ($\Pi = A, B_i, C_i, D_i, E$) and an irradiated void Ω, the contribution of the void Π to the radiosity of the void Ω, after one reflection by a strut s, is given by the following correlation

$$J\Omega = \rho_s \frac{A_\Pi}{A_\Omega} F_{\Pi s} \; F_{s\Omega} \, J\Pi \qquad \text{(A.8)}$$

If reference is made to the bcc surface area, A_{bcc}, eq.A.8 becomes

$$J\Omega = \rho_s \frac{A_\Pi}{A_\Omega} F_{\Pi s} F_{s\Omega} \; J\Pi \frac{A_\Omega}{A_{bcc}} \qquad \text{(A.9)}$$

Summing up the radiosity in eq.A.9 over all struts, one obtains the total contribution of the irradiating void Π to the radiosity of the Ω void and, then, summing up over all voids and over the index i from 1 to 4, when it is necessary (i.e. for voids B, C, D), one obtains the total contribution of all irradiating voids Π to the radiosity of the A_{bcc} surface, orthogonal to the z direction. One can conclude that these algebraic operations are equivalent to extract the diagonal of the row by column product of matrix $\boldsymbol{F_{\Pi\text{-}s}}$ by the transpose of matrix $\boldsymbol{F^T_{s-\Pi}}$, that both represent the heat transferred.

Then we calculate the sum of components of the obtained vector: i.e. are equivalent to calculate the trace of the mentioned matrixes product.

For example, as to the heat transfer between all irradiating *C* voids and the irradiated void *A*, the contribution of irradiating *C* voids to the irradiated void *A* after one reflection by a strut *s*, $(JA)_C^{1r}$, is given by the following correlation

$$(JA)_C^{1r} = \rho_s \frac{A_c}{A_\Omega} Tr\,(\boldsymbol{F_{C-s}}\,\boldsymbol{F_{s-A}^T})\,JC\,\frac{A_\Omega}{A_{bcc}} \tag{A.10}$$

where $\boldsymbol{F_{C-s}}\,\boldsymbol{F_{s-A}^T}$ represents the matrix $\boldsymbol{CA}$ in Eq.2.48. All other similar coefficients in eqs.2.46-2.57 can be expressed in the same way as $(JA)_C^{1r}$.

Let us now consider the interaction between struts and voids after one reflection from struts. To this aim the same matrix approach and similar symbols can be used to indicate the product of matrixes $\boldsymbol{sA}$, $\boldsymbol{sB}$ and $\boldsymbol{sC}$ when reference is made to the interaction of a strut with the respective void

$$\begin{aligned} \boldsymbol{sA} = \boldsymbol{sE} &= F_{st,av}\mathbf{1}\cdot\boldsymbol{F_{s-A}^T} \\ \boldsymbol{sB} = \boldsymbol{sD} &= F_{st,av}\mathbf{1}\cdot\boldsymbol{F_{s-B}^T} \\ \boldsymbol{sC} &= F_{st,av}\mathbf{1}\cdot\boldsymbol{F_{s-C}^T} \end{aligned} \tag{A.11}$$

where $F_{st,av}$ is the average strut-strut view factor and $\mathbf{1}$ is the unitary matrix.

The contribution of any strut arbitrarily set at the emissive power after one reflection to the radiosity in eqs.2.58, 2.62 and 2.66.can, therefore, be expounded in the following way

$$(JA)_s^{1r} = (JE)_s^{1r} = 35\,\rho\,\frac{A_s}{A_u}\,Tr(\boldsymbol{sA})\,\sigma\,\varepsilon\,T^4$$

$$(JB)_s^{1r} = (JD)_s^{1r} = 35\,\rho\,\frac{A_s}{A_u}\,Tr(\boldsymbol{sB})\,\sigma\,\varepsilon\,T^4 \qquad \text{(A.12)}$$

$$(JC)_s^{1r} = 35\,\rho\,\frac{A_s}{A_u}\,Tr(\boldsymbol{sC})\,\sigma\,\varepsilon\,T^4$$

where account has been taken that the heat reflected by a strut seems to radiate directly from that strut, apart from of the loss by reflection and that there are 35 equal terms, as many as are the couples involved in the emissions and reflections by the generic and originary selected strut. Therefore, the contributions of direct emission of the strut toward voids must be added to eq.A.12, in order to obtain eqs.2.58, 2.62 and 2.66. The terms are the following

$$(JA)_s^{1d} = (JE)_s^{1d} = \frac{A_s\,Tr(\boldsymbol{sA})}{A_E}\;\sigma\,\varepsilon\,T^4$$

$$(JB)_s^{1d} = (JD)_s^{1d} = \frac{A_s\,Tr(\boldsymbol{sB})}{A_D}\;\sigma\,\varepsilon\,T^4 \qquad \text{(A.13)}$$

$$(JC)_s^{1d} = \frac{A_s\,Tr(\boldsymbol{sC})}{A_C}\;\sigma\,\varepsilon\,T^4$$

The number of independent view factors that allow the evaluation of the coefficients or, best, of their reflected components, can be reduced, by using both the reciprocity property and symmetry correlations.

NOMENCLATURE

Symbol	Quantity	Unit
a	Distance between bcc nodes or cell size	m
a_i, b_i	Coefficients in eqs.2.24-2.25	dimensionless
A	Area of the strut cross-section	m^2
A_{ac}	Area of surface in eq.1.37	m^2
A_{ic}	Area of the strut with concave cross-section	m^2
A_{bcc}	bcc surface area	m^2
A_e	Area of the hexagonal voids	m^2
A_{ext}	Factor correction of the area in eq.1.59	m^2
A_i	Square void surface area (section 2.2)	m^2
A_I	Void surface area (section 2.3)	m^2
A_{irr}	Irradiated surface area of a sphere	m^2
A_r	Aspect ratio (h/l)	dimensionless
A_s	Strut surface area	m^2
A_{sq}	Area of the square	m^2
c	Geometrical parameter in eqs.1.30	m

C	Number of cells (in eq.1.6)	dimensionless
C_1, C_2	Coefficients in eqs. 1.9, 1.10	dimensionless
d	Diameter of a cylindrical strut (theoretical)	µm, mm, m
d_1	Diameter of the sphere tangent to the squares of a TD	µm, mm, m
d_2	Diameter of the sphere tangent to the hexagons of a TD	µm, mm, m
d_f	Measured diameter of a cylindrical strut	µm, mm, m
d_i	Average inner diameter of the hollow struts	µm, mm, m
d_{ic}	Apparent diameter of a concave strut (theoretical)	µm, mm, m
$d_{In\text{-}c}$	Diameter of a cylindrical strut by Inayat et al.	µm, mm, m
$d_{In\text{-}con\text{-}a}$	Apparent diameter of a concave strut by Inayat et al.	µm, mm, m
$d_{In\text{-}con\text{-}e}$	Effective diameter of a concave strut by Inayat et al.	µm, mm, m
d_N	Nominal diameter of a strut	inch
d_p	Characteristic cell size (diameter)	µm, mm, m
d'_p	Side of a cubic pore	µm, mm, m

d_s	Measured diameter of cylindrical struts	µm, mm, m
d_S	Diameter of the sphere	µm, mm, m
d'_s	Diameter of a cubic REV strut	µm, mm, m
d_{tc}	Apparent diameter of a convex strut (theoretical)	µm, mm, m
d_w	Windows size (diameter)	µm, mm, m
E	Number of edges (in eq.1.6)	dimensionless
F, f	Number of faces (in eq.1.6)	dimensionless
$F_{i\Pi}$	Strut-void view factor	dimensionless
$F_{s\text{-}s}$	Strut-strut view factor	dimensionless
$F_{s\text{-}\Pi}$	Strut-void view factor	dimensionless
$F_{\Pi\text{-}\Omega}$	Void-void view factor	dimensionless
$F_{s\text{-}s,\,av}$	Average strut-strut view factor	dimensionless
$F_{S1\text{-}S2}$	View factor between surfaces S_1 and S_2 finite or infinitesimal	dimensionless
G	Parameter in eq.2.14	dimensionless
h	Height of the sphere segment or height of a prism	m
h_{hex}	Height of spherical caps onto hexagons	m

h_{sq}	Height of spherical caps onto squares	m
$I_{b\lambda}$	Black body radiative intensity field	W/μm m^2 sr
I_{λ}	Monochromatic radiative intensity field	W/μm m^2 sr
$JA^{(i)}$	A void radiosity	W/m^2
$JB^{(i)}$	B void radiosity	W/m^2
$JC^{(i)}$	C void radiosity	W/m^2
$JD^{(i)}$	D void radiosity	W/m^2
$JE^{(i)}$	E void radiosity	W/m^2
k_c	Thermal conductivity	W/m K
k_r	Radiative conductivity	W/m K
k_R	Rosseland radiative conductivity	W/m K
k_{eff}	Effective conductivity	W/m K
l	Void side length, edge length of a polyhedron or strut length	μm, mm, m
L	Length of the plate	m
l_c	Length of a cylindrical strut (theoretical)	μm, mm, m
l_{ga}	Length of a triangular strut by Gibson and Ashby	μm, mm, m
l_{ic}	Length of a concave strut (theoretical)	μm, mm, m

$l_{In\text{-}c}$	Length of a cylindrical strut by Inayat et al.	μm, mm, m
$l_{In\text{-}t}$	Length of a triangular strut by Inayat et al.	μm, mm, m
l_s	Measured strut length	μm, mm, m
l_t	Length of a triangular strut (theoretical)	μm, mm, m
n	Index of refraction	dimensionless
n_i	Nodes	dimensionless
N_p	Number of cells along z	dimensionless
PPI	Pores Per Inch	1/inch
q_r	Heat flux	W/m^2
$q_{r,\eta}$	Monochromatic radiative heat flux	W/m^2
q_r^z	Heat flux in z direction	
r_s	Radius of a sphere	m
s	Sample thickness	m
S	Irradiating surface area of a sphere	m^2
S_o	Area of the internal surface of an open cell for the spherical model	m^2
S_c	Area of the internal surface of a partially closed cell for the spherical model	m^2
Sv	Interfacial surface per unit volume	m^2/m^3

Sv_c	Interfacial surface per unit volume of a partially closed cell for the spherical model	m^2/m^3
$Sv_{In\text{-}con\text{-}e\ c}$	Interfacial surface per unit volume for cylindrical strut (theoretical)	m^2/m^3
Sv_{ic}	Interfacial surface per unit volume for concave strut (theoretical)	m^2/m^3
$Sv_{In\text{-}c}$	Interfacial surface per unit volume for cylindrical strut by Inayat et al.	m^2/m^3
$Sv_{In\text{-}con\text{-}e}$	Effective interfacial surface per unit volume for concave strut by Inayat et al.	m^2/m^3
Sv_o	Interfacial surface per unit volume of an open cell for the spherical model	m^2/m^3
Sv_{rich}	Interfacial surface per unit volume for triangular strut by Richardson et al.	m^2/m^3
Sv_t	Interfacial surface per unit volume for triangular strut (theoretical)	m^2/m^3
t	Generic side length of the triangular cross-section of a strut	µm, mm, m
t_{ga}	Side length of the triangular cross-section of a strut by Gibson and Ashby	µm, mm, m
t_m	Side length of the square cross-section of a strut	µm, mm, m

t_{meas}	Measured thickness of a strut in Table 1.4	mm
t_o	Generic thickness of a strut	μm, mm, m
t_s	Side length of the triangular cross-section of a strut (theoretical)	μm, mm, m
t_{rich}	Side length of the triangular cross-section of a strut by Richardson et al.	μm, mm, m
T	Temperature	K
T_c	Temperature of the cold plate	K
T_h	Temperature of the hot plate	K
V	Number of vertexes of a polyhedron	dimensionless
V_{hollow}	Hollow volume internal to the struts	m^3
V_I	Volume of the empty space in a foam external to the struts	m^3
V_o	Block volume	m^3
V_{cs}	Volume of the empty space in a partially closed cell for spherical model	m^3
V_{os}	Volume of the empty space in a opened cell for spherical model	m^3
V_s	Solid volume	m^3
V_{sshex}	Volume of spherical caps onto hexagonal	m^3

	faces	
V_{sssq}	Volume of spherical caps onto square faces	m^3
V_{strut}	Strut volume	m^3
V_{TD}	Tetrakaidecahedron volume	m^3
W	Width of the plate	m
x	Geometrical parameter in eqs.1.30	m
x, y, z	Cartesian coordinates	m
Z_e	Edge connectivity	dimensionles
Z_f	Face connectivity	dimensionles
Greek letters		
$\alpha_i, \beta_i, \gamma_i$	Coefficients in eqs.2.24-2.25, 2.49-2.51	dimensionless
$\beta_\lambda, \beta_\eta$	Monochromatic extinction coefficient	m^{-1}
β_R	Rosseland-mean extinction coefficient	m^{-1}
δ_i	Coefficients in eqs 2.34-2.35	dimensionless
ε	Emissivity	dimensionless
η	Wave number	μm^{-1}
φ, Φ	Porosity or effective porosity	dimensionless
Φ_λ	Phase function of scattering	dimensionless

φ_t	External or outer porosity	dimensionless
κ_λ	Monochromatic absorption (emission) coefficient	dimensionless
λ	Wavelength	μm
σ_λ	Monochromatic scattering coefficient	dimensionless
ω_λ	Ssingle scattering albedo coefficient	dimensionless
φ_t	External or outer posity	dimensionless
ΔT	Temperature difference	K
ρ^*	Fictitious relative density for empty struts	dimensionless
ρ_o	Foam density	kg/ m^3
ρ_s	Solid density	kg/m^3
ρ_r	Relative density	dimensionless
$\bar{\sigma}$	Stephan-Boltzmann constant	W/m^2 K^4
Subscripts		
c	Cold plate	
h	Hot plate	
i	i-th plane	
Π, Ω	Refers to voids	

Superscripts	
$^{-}$	Average

REFERENCES

[1] Gibson L. J., and Ashby M. F., 1999, Cellular solids: structure and properties, Cambridge Univ Pr.

[2] Thomson W., 1887, "LXIII. On the division of space with minimum partitional area," Philosophical Magazine Series 5, **24**(151), pp. 503–514.

[3] Weaire D., 2008, "Kelvin's foam structure: a commentary," Philosophical Magazine Letters, **88**(2), pp. 91–102.

[4] Princen H. ., and Levinson P., 1987, "The surface area of Kelvin's minimal tetrakaidecahedron: The ideal foam cell (?)," Journal of Colloid and Interface Science, **120**(1), pp. 172–175.

[5] Weaire D., and Phelan R., 1994, "A counter-example to Kelvin's conjecture on minimal surfaces," Philosophical Magazine Letters, **69**(2), pp. 107–110.

[6] Ashcroft N. W., and Mermin N. D., 2010, "Solid State Physics (Saunders College, Philadelphia, 1976)".

[7] Inayat A., Freund H., Zeiser T., and Schwieger W., 2011, "Determining the specific surface area of ceramic foams: The tetrakaidecahedra model revisited," Chemical Engineering Science, **66**(6), pp. 1179–1188.

[8] Duan D. L., Zhang R. L., Ding X. J., and Li S., 2006, "Calculation of specific surface area of foam metals using dodecahedron model," Materials Science and Technology, **22**(11), pp. 1364–1367.

[9] Twigg M. V., and Richardson J. T., 2007, "Fundamentals and Applications of Structured Ceramic Foam Catalysts," Ind. Eng. Chem. Res., **46**(12), pp. 4166–4177.

[10] Incera Garrido G., Patcas F. C., Lang S., and Kraushaar-Czarnetzki B., 2008, "Mass transfer and pressure drop in ceramic foams: A description for different pore sizes and porosities," Chemical Engineering Science, **63**(21), pp. 5202–5217.

[11] De Hoff., Rhines, 1968,,"Quantitative Microscopy", McGraw–Hill, New York.

[12] Richardson J. T., Peng Y., and Remue D., 2000, "Properties of ceramic foam catalyst supports: pressure drop," Applied Catalysis A: General, **204**(1), pp. 19–32.

[13] Bhattacharya A., Calmidi V. V., and Mahajan R. L., 2002, "Thermophysical properties of high porosity metal foams," International Journal of Heat and Mass Transfer, **45**(5), pp. 1017–1031.

[14] Richardson J. T., Peng Y., and Remue D., 2000, "Properties of ceramic foam catalyst supports: pressure drop," Applied Catalysis A: General, **204**(1), pp. 19–32.

[15] Mancin S., Zilio C., Cavallini A., and Rossetto L., 2010, "Heat transfer during air flow in aluminum foams," International Journal of Heat and Mass Transfer, **53**(21–22), pp. 4976–4984.

[16] S.Mancin, 2008, "Single-Phase Heat Transfer and Fluid Flow through Enhanced Surfaces and in Microgeometries," Ph.D. Thesis, University of Padova.

[17] Huu T. T., Lacroix M., Pham Huu C., Schweich D., and Edouard D., 2009, "Towards a more realistic modeling of solid foam: Use of the pentagonal dodecahedron geometry," Chemical Engineering Science, **64**(24), pp. 5131–5142.

[18] Bianchi E., Heidig T., Visconti C. G., Groppi G., Freund H., and Tronconi E., 2012, "An appraisal of the heat transfer properties of metallic open-cell foams for strongly exo-/endo-thermic catalytic processes in tubular reactors," Chemical Engineering Journal, **198-199**, pp. 512–528.

[19] Giani L., Groppi G., and Tronconi E., 2005, "Mass-Transfer Characterization of Metallic Foams as Supports for Structured Catalysts," Ind. Eng. Chem. Res., **44**(14), pp. 4993–5002.

[20] Große J., Dietrich B., Martin H., Kind M., Vicente J., and Hardy E. H., 2008, "Volume image analysis of ceramic sponges," Chemical Engineering and Technology, **31**(2), pp. 307–314.

[21] Bhattacharya A., Calmidi V. V., and Mahajan R. L., 1999, "An Analytical-Experimental Study for the determination of the effective thermal conductivity of high porosity fibrous foams," ASME Applied Mechanics Dvision-Publications-AMD, **233**, pp. 13–20.

[22] Calmidi V. V., and Mahajan R. L., 2000, "Forced convection in high porosity metal foams," Journal of Heat Transfer, **122**, p. 557.

[23] Boomsma K., and Poulikakos D., 2001, "On the effective thermal conductivity of a three-dimensionally structured fluid-saturated metal foam," International Journal of Heat and Mass Transfer, **44**(4), pp. 827–836.

[24] Twigg M. V., and Richardson J. T., 2002, "Theory and applications of ceramic foam catalysts," Chemical Engineering Research and Design, **80**(2), pp. 183–189.

[25] Buciuman F. C., and Kraushaar-Czarnetzki B., 2003, "Ceramic Foam Monoliths as Catalyst Carriers. 1. Adjustment and Description of the Morphology," Ind. Eng. Chem. Res., **42**(9), pp. 1863–1869.

[26] Inayat A., Schwerdtfeger J., Freund H., Körner C., Singer R. F., and Schwieger W., 2011, "Periodic open-cell foams: Pressure drop measurements and modeling of an ideal tetrakaidecahedra packing," Chemical Engineering Science, **66**(12), pp. 2758–2763.

[27] Calmidi V. V., 1998, "Transport phenomena in high porosity fibrous metal foams," University of Colorado.

[28] Ghosh I., "Heat transfer correlation in high-porosity open-cell foam," International Journal of Heat and Mass Transfer, **52**(5), pp. 1488–1494.

[29] Zhao C. Y., Tassou S. A., and Lu T. J., 2008, "Analytical considerations of thermal radiation in cellular metal foams with open cells," International Journal of Heat and Mass Transfer, **51**(3–4), pp. 929–940.

[30] Lu T. J., Zhao C. Y., Kim T., and Hodson H. P., 2004, "Thermal Transport in High Porosity Cellular Metal Foams," Journal of Thermophysics and Heat Transfer, **18**(3), pp. 309–317.

[31] Fuller A. J., Kim T., Hodson H. P., and Lu T. J., 2005, "Measurement and interpretation of the heat transfer coefficients of metal foams," Proceedings of the Institution of Mechanical Engineers, Part C: Journal of Mechanical Engineering Science, **219**(2), pp. 183–191.

[32] Lu T. J., Stone H. A., and Ashby M. F., 1998, "Heat transfer in open-cell metal foams," Acta Materialia, **46**(10), pp. 3619–3635.

[33] G Fourie J., and P Du Plessis J., 2002, "Pressure drop modelling in cellular metallic foams," Chemical Engineering Science, **57**(14), pp. 2781–2789.

[34] Du Plessis P., 1994, "Pressure drop prediction for flow through high porosity metallic foams," Chemical Engineering Science, **49**(21), pp. 3545–3553.

[35] Stemmet C. P., Van Der Schaaf J., Kuster B. F. M., and Schouten J. C., 2006, "Solid Foam Packings for Multiphase Reactors," Chemical Engineering Research and Design, **84**(12), pp. 1134–1141.

[36] Grosse J., Dietrich B., Garrido G. I., Habisreuther P., Zarzalis N., Martin H., Kind M., and Kraushaar-Czarnetzki B., 2009, "Morphological Characterization of Ceramic Sponges for Applications in Chemical Engineering," Industrial & Engineering Chemistry Research, **48**(23), pp. 10395–10401.

[37] Moreira E. A., and Coury J. R., 2004, "The influence of structural parameters on the permeability of ceramic foams," Brazilian Journal of Chemical Engineering, **21**(1), pp. 23–33.

[38] Krishnan S., Murthy J. Y., and Garimella S. V., 2006, "Direct Simulation of Transport in Open-Cell Metal Foam," Journal of Heat Transfer, **128**(8), p. 793.

[39] Ashby M. F., 2000, Metal Foams: A Design Guide, Elsevier.

[40] Druma A. M., Alam M. K., and Druma C., 2004, "Analysis of thermal conduction in carbon foams," International Journal of Thermal Sciences, **43**(7), pp. 689–695.

[41] Peng H. X., Fan Z., Evans J. R. G., and Busfield J. J. C., 2000, "Microstructure of ceramic foams," Journal of the European Ceramic Society, **20**(7), pp. 807–813.

[42] 2008, Wolfram Mathematica, Wolfram Research.

[43] Zhao C. Y., 2012, "Review on thermal transport in high porosity cellular metal foams with open cells," International Journal of Heat and Mass Transfer, **55**(13), pp. 3618–3632.

[44] Ashby M. F., Evans T., Fleck N. A., Hutchinson J. W., Wadley H. N. G., and Gibson L. J., 2000, Metal Foams: A Design Guide: A Design Guide, Butterworth-Heinemann.

[45] Ashby M. F., and Lu T., 2003, "Metal foams: a survey," Science in China Series B: Chemistry, **46**(6), pp. 521–532.

[46] Xu H. J., Qu Z. G., and Tao W. Q., 2011, "Thermal transport analysis in parallel-plate channel filled with open-celled metallic foams," International Communications in Heat and Mass Transfer, **38**(7), pp. 868–873.

[47] Fend T., 2010, "High porosity materials as volumetric receivers for solar energetics," Optica Applicata, **11**(2), pp. 271–284.

[48] Fend T., Hoffschmidt B., Pitz-Paal R., Reutter O., and Rietbrock P., 2004, "Porous materials as open volumetric solar receivers: experimental determination of thermophysical and heat transfer properties," Energy, **29**(5), pp. 823–833.

[49] Fend T., Pitz-Paal R., Reutter O., Bauer J., and Hoffschmidt B., 2004, "Two novel high-porosity materials as volumetric receivers for concentrated solar radiation," Solar energy materials and solar cells, **84**(1), pp. 291–304.

[50] Ávila-Marín A. L., 2011, "Volumetric receivers in solar thermal power plants with central receiver system technology: a review," Solar Energy, **85**(5), pp. 891–910.

[51] Buck R., Muir J. F., and Hogan R. E., 1991, "Carbon dioxide reforming of methane in a solar volumetric receiver/reactor: the CAESAR project," Solar energy materials, **24**(1), pp. 449–463.

[52] Chavez J. M., and Chaza C., 1991, "Testing of a porous ceramic absorber for a volumetric air receiver," Solar energy materials, **24**(1), pp. 172–181.

[53] Villafán-Vidales H. I., Abanades S., Caliot C., and Romero-Paredes H., 2011, "Heat transfer simulation in a thermochemical solar reactor based on a volumetric porous receiver," Applied Thermal Engineering, **31**(16), pp. 3377–3386.

[54] Wu Z., Caliot C., Flamant G., and Wang Z., 2011, "Coupled radiation and flow modeling in ceramic foam volumetric solar air receivers," Solar Energy, **85**(9), pp. 2374–2385.

[55] Gokon N., Osawa Y., Nakazawa D., and Kodama T., 2009, "Kinetics of CO< sub> 2</sub> reforming of methane by catalytically activated metallic foam absorber for solar receiver-reactors," International journal of hydrogen energy, **34**(4), pp. 1787–1800.

[56] Kodama T., Ohtake H., Shimizu K. I., and Kitayama Y., 2002, "Nickel catalyst driven by direct light irradiation for solar CO2-reforming of methane," Energy & fuels, **16**(5), pp. 1016–1023.

[57] Kodama T., 2003, "High-temperature solar chemistry for converting solar heat to chemical fuels," Progress in Energy and Combustion Science, **29**(6), pp. 567–597.

[58] Chen C. C., and Huang P. C., 2012, "Numerical study of heat transfer enhancement for a novel flat-plate solar water collector using metal-foam blocks," International Journal of Heat and Mass Transfer.

[59] Wu Z., Caliot C., Bai F., Flamant G., Wang Z., Zhang J., and Tian C., 2010, "Experimental and numerical studies of the pressure drop in ceramic foams for volumetric solar receiver applications," Applied Energy, **87**(2), pp. 504–513.

[60] Wu Z., Caliot C., Flamant G., and Wang Z., 2011, "Numerical simulation of convective heat transfer between air flow and ceramic foams to optimise volumetric solar air receiver performances," International Journal of Heat and Mass Transfer, **54**(7), pp. 1527–1537.

[61] Clyne T. W., Golosnoy I. O., Tan J. C., and Markaki A. E., 2006, "Porous materials for thermal management under extreme conditions," Philosophical Transactions of the Royal Society A: Mathematical, Physical and Engineering Sciences, **364**(1838), pp. 125–146.

[62] Chang Y. J., Wang C., and Chang W. J., 1994, "Heat transfer and flow characteristics of automotive brazed aluminum heat exchangers," ASHRAE Transactions, pp. 643–652.

[63] Kim S. Y., Paek J. W., and Kang B. H., 2000, "Flow and Heat Transfer Correlations for Porous Fin in a Plate-Fin Heat Exchanger," Journal of Heat Transfer, **122**(3), p. 572.

[64] Sahnoun A., and Webb R. L., 1992, "Prediction of Heat Transfer and Friction for the Louver Fin Geometry," Journal of Heat Transfer, **114**(4), p. 893.

[65] Tseng C. C., Sikorski R. L., Viskanta R., and Chen M. Y., 2012, "Effect of Foam Properties on Heat Transfer in High Temperature Open-Cell Foam Inserts," Journal of the American Ceramic Society.

[66] Lipinski W., Wyss P., and Steinfeld A., 2010, "Tomography-based heat and mass transfer characterization of reticulate porous ceramics for high-temperature processing," Journal of Heat Transfer, **132**, pp. 023305–1.

[67] Nettleship I., 1996, "Applications of Porous Ceramics," Key Engineering Materials, **122-124**, pp. 305–324.

[68] Matthews A. L., 1996, "Ceramic Filters for the Cast Metal Industry," Key Engineering Materials, **122-124**, pp. 293–304.

[69] Van Setten B. A. A. ., Bremmer J., Jelles S. ., Makkee M., and Moulijn J. ., 1999, "Ceramic foam as a potential molten salt oxidation catalyst support in the removal of soot from diesel exhaust gas," Catalysis Today, **53**(4), pp. 613–621.

[70] Barra A. J., Diepvens G., Ellzey J. L., and Henneke M. R., 2003, "Numerical study of the effects of material properties on flame stabilization in a porous burner," Combustion and Flame, **134**(4), pp. 369–379.

[71] Dhamrat R. S., and Ellzey J. L., 2006, "Numerical and experimental study of the conversion of methane to hydrogen in a porous media reactor," Combustion and Flame, **144**(4), pp. 698–709.

[72] Lu T. J., and Chen C., 1999, "Thermal transport and fire retardance properties of cellular aluminium alloys," Acta Materialia, **47**(5), pp. 1469–1485.

[73] "ERG Materials & Aerospace – Duocel® Metal Foam, Introduction to Duocel Application." [Online]. Available: http://www.ergaerospace.com. [Accessed: 08-Jan-2013].

[74] "Dunlop Equipment, Retiment, 2007." [Online]. Available: http://www.dunlop-equipment.com [Accessed: 08-Jan-2013].

[75] "Metafoam - Products.Metafoam, Metafoam Technical Fact Sheet, 2010." [Online]. Available: http://www.metafoam.com. [Accessed: 08-Jan-2013].

[76] "Cryo Tech and New Cooling Technologies You Have Never Seen - FrostyTech.com" [Online]. Available: http://www.frostytech.com. [Accessed: 08-Jan-2013].

[77] Albanakis C., Missirlis D., Michailidis N., Yakinthos K., Goulas A., Omar H., Tsipas D., and Granier B., 2009, "Experimental analysis of the pressure drop and heat transfer through metal foams used as volumetric receivers under concentrated solar radiation," Experimental Thermal and Fluid Science, **33**(2), pp. 246–252.

[78] Yu H., Chen H., Pan M., Tang Y., Zeng K., Peng F., and Wang H., 2007, "Effect of the metal foam materials on the performance of methanol steam micro-reformer for fuel cells," Applied Catalysis A: General, **327**(1), pp. 106–113.

[79] Yu X., Wen Z., Lin Y., Tu S.-T., Wang Z., and Yan J., 2010, "Intensification of biodiesel synthesis using metal foam reactors," Fuel, **89**(11), pp. 3450–3456.

[80] Mellouli S., Dhaou H., Askri F., Jemni A., and Ben Nasrallah S., 2009, "Hydrogen storage in metal hydride tanks equipped with metal foam heat exchanger," International Journal of Hydrogen Energy, **34**(23), pp. 9393–9401.

[81] T'Joen C., De Jaeger P., Huisseune H., Van Herzeele S., Vorst N., and De Paepe M., 2010, "Thermo-hydraulic study of a single row heat exchanger consisting of metal foam covered round tubes," International Journal of Heat and Mass Transfer, **53**(15–16), pp. 3262–3274.

[82] Wood S., and Harris A. T., 2008, "Porous burners for lean-burn applications," Progress in Energy and Combustion Science, **34**(5), pp. 667–684.

[83] Modest M. F., 2003, Radiative heat transfer, Academic press.

[84] Siegel R., and Howell J. R., 2002, Thermal Radiation Heat Transfer, Taylor & Francis.

[85] Baillis D., and Sacadura J. F., 2000, "Thermal radiation properties of dispersed media: theoretical prediction and experimental characterization," Journal of Quantitative Spectroscopy and Radiative Transfer, **67**(5), pp. 327–363.

[86] Lipinski W., and Steinfeld A., 2005, "Transient radiative heat transfer within a suspension of coal particles undergoing steam gasification," Heat Mass Transfer, **41**(11), pp. 1021–1032.

[87] Singh B. P., and Kaviany M., 1992, "Modelling radiative heat transfer in packed beds," International Journal of Heat and Mass Transfer, **35**(6), pp. 1397–1405.

[88] Osinga T., Lipinski W., Guillot E., Olalde G., and Steinfeld A., 2006, "Experimental Determination of the Extinction Coefficient for a Packed-Bed Particulate Medium," Experimental Heat Transfer, **19**(1), pp. 69–79.

[89] Hale M. J., and Bohn M. S., 1992, Measurement of the radiative transport properties of reticulated alumina foams, National Renewable Energy Lab., Golden, CO (United States).

[90] Argento C., and Bouvard D., 1996, "Modeling the effective thermal conductivity of random packing of spheres through densification," International Journal of Heat and Mass Transfer, **39**(7), pp. 1343–1350.

[91] Loretz M., Coquard R., Baillis D., and Maire E., 2008, "Metallic foams: Radiative properties/comparison between different models," Journal of Quantitative Spectroscopy and Radiative Transfer, **109**(1), pp. 16–27.

[92] Zhao C. Y., Tassou S. A., and Lu T. J., 2008, "Analytical considerations of thermal radiation in cellular metal foams with open cells," International Journal of Heat and Mass Transfer, **51**(3), pp. 929–940.

[93] Placido E., Arduini-Schuster M. C., and Kuhn J., 2005, "Thermal properties predictive model for insulating foams," Infrared physics & technology, **46**(3), pp. 219–231.

[94] Petrasch J., Wyss P., and Steinfeld A., 2007, "Tomography-based Monte Carlo determination of radiative properties of reticulate porous ceramics," Journal of Quantitative Spectroscopy and Radiative Transfer, **105**(2), pp. 180–197.

[95] Loretz M., Maire E., and Baillis D., 2008, "Analytical Modelling of the Radiative Properties of Metallic Foams: Contribution of X-Ray Tomography," Advanced engineering materials, **10**(4), pp. 352–360.

[96] Coquard R., Loretz M., and Baillis D., 2008, "Conductive Heat Transfer in Metallic/Ceramic Open-Cell Foams," Advanced Engineering Materials, **10**(4), pp. 323–337.

[97] Coquard R., Baillis D., and Randrianalisoa J., 2011, "Homogeneous phase and multi-phase approaches for modeling radiative transfer in foams," International Journal of Thermal Sciences, **50**(9), pp. 1648–1663.

[98] Akolkar A., and Petrasch J., 2011, "Tomography based pore-level optimization of radiative transfer in porous media," International Journal of Heat and Mass Transfer, **54**(23), pp. 4775–4783.

[99] Coquard R., Rousseau B., Echegut P., Baillis D., Gomart H., and Iacona E., 2011, "Investigations of the radiative properties of Al–NiP foams using tomographic images and stereoscopic micrographs," International journal of heat and mass transfer.

[100] Tancrez M., and Taine J., 2004, "Direct identification of absorption and scattering coefficients and phase function of a porous medium by a Monte

Carlo technique," International Journal of Heat and Mass Transfer, **47**(2), pp. 373–383.

[101] Taine J., Iacona E., and Bellet F., 2008, "Radiation in porous media: an upscaling methodology," Proceedings 5th European Thermal-Sciences Conference, T.H. van der M. G.G.M. Stoffels, and A.A. van Steenhoven, eds., Eindhoven, Pays-Bas, pp. ISBN 978–90–386–1274–4.

[102] Zeghondy B., Iacona E., and Taine J., 2006, "Determination of the anisotropic radiative properties of a porous material by radiative distribution function identification (RDFI)," International journal of heat and mass transfer, **49**(17), pp. 2810–2819.

[103] Rémi C., Dominique B., and Daniel Q., 2009, "Radiative Properties of Expanded Polystyrene Foams," Journal of Heat Transfer, **131**(1), p. 012702.

[104] Baillis D., Raynaud M., and Sacadura J. F., "Determination of spectral radiative properties of open cell foam: Model validation," Journal of thermophysics and heat transfer, **14**(2), pp. 137–143.

[105] Baillis D., Raynaud M., and Sacadura J. F., "Spectral radiative properties of open-cell foam insulation," Journal of thermophysics and heat transfer, **13**(3), pp. 292–298.

[106] Coquard R., Rochais D., and Baillis D., 2011, "Modeling of the coupled conductive and radiative heat transfer IN NiCrAl from photothermal measurements and x-ray tomography," Special Topics & Reviews in Porous Media - An International Journal, **2**(4), pp. 249–265.

[107] Coquard R., Rochais D., and Baillis D., 2009, "Experimental investigations of the coupled conductive and radiative heat transfer in metallic/ceramic foams," International Journal of Heat and Mass Transfer, **52**(21), pp. 4907–4918.

[108] Lipiński W., Keene D., Haussener S., and Petrasch J., 2010, "Continuum radiative heat transfer modeling in media consisting of optically distinct components in the limit of geometrical optics," Journal of Quantitative Spectroscopy and Radiative Transfer, **111**(16), pp. 2474–2480.

[109] Lipiński W., Petrasch J., and Haussener S., 2010, "Application of the spatial averaging theorem to radiative heat transfer in two-phase media," Journal of Quantitative Spectroscopy and Radiative Transfer, **111**(1), pp. 253–258.

[110] Coquard R., Rochais D., and Baillis D., 2012, "Conductive and radiative heat transfer in ceramic and metal foams at fire temperatures," Fire technology, pp. 1–34.

[111] De Micco C., and Aldao C. M., 2005, "Radiation contribution to the thermal conductivity of plastic foams," Journal of Polymer Science Part B: Polymer Physics, **43**(2), pp. 190–192.

[112] Micco C. D., and Aldao C. M., 2003, "On the net radiation method for heat transfer," European Journal of Physics, **24**(1), pp. 81–89.

[113] Zhao C. Y., Lu T. J., Hodson H. P., and Jackson J. D., 2004, "The temperature dependence of effective thermal conductivity of open-celled steel alloy foams," Materials Science and Engineering: A, **367**(1), pp. 123–131.

[114] Glicksman L., Schuetz M., and Sinofsky M., 1987, "Radiation heat transfer in foam insulation," International journal of heat and mass transfer, **30**(1), pp. 187–197.

[115] Glicksman L. R., Marge A. L., and Moreno J. D., 1993, "Radiation heat transfer in cellular foam insulation," ASME-PUBLICATIONS-HTD, **203**, pp. 45–45.

[116] Cunnington G. R., Lee S. C., and White S. M., "Radiative properties of fiber-reinforced aerogel : Theory versus experiment," Journal of thermophysics and heat transfer, **12**(1), pp. 17–22.

[117] Lee S. C., and Cunnington G. R., "Heat transfer in fibrous insulations : Comparison of theory and experiment," Journal of thermophysics and heat transfer, **12**(3), pp. 297–303.

[118] Caps R., Heinemann U., Fricke J., and Keller K., 1997, "Thermal conductivity of polyimide foams," International Journal of Heat and Mass Transfer, **40**(2), pp. 269–280.

[119] Zhao C. Y., Lu T. J., and Hodson H. P., 2004, "Thermal radiation in ultralight metal foams with open cells," International Journal of Heat and Mass Transfer, **47**(14–16), pp. 2927–2939.

[120] Andreozzi A., Bianco N., Manca O., and Naso V., 2012, "Numerical analysis of radiation effects in a metallic foam by means of the radiative conductivity model," Applied Thermal Engineering, **49**(0), pp. 14–21.

[121] Howell J. R., 1998, "The Monte Carlo method in radiative heat transfer," Journal of Heat Transfer, **120**(3), pp. 547–560.

[122] 2008, TracePro, Lambda Research Corporation.

[123] Bhattacharya A., Calmidi V. V., and Mahajan R. L., 2002, "Thermophysical properties of high porosity metal foams," International Journal of Heat and Mass Transfer, **45**(5), pp. 1017–1031.